A Thesis Submitted for the Degree of PhD at the University of Warwick

Permanent WRAP URL:

http://wrap.warwick.ac.uk/158011
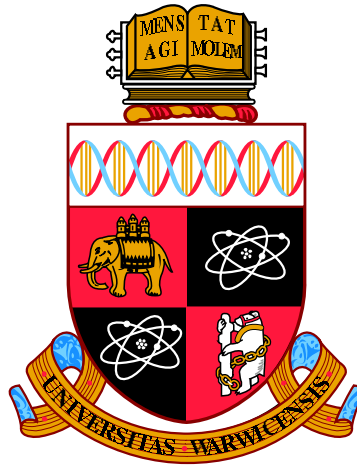
For more information, please contact the WRAP Team at: wrap@warwick.ac.uk

warwick.ac.uk/lib-publications

FLUCTUATING HYDRODYNAMICS OF NANOSCALE INTERFACIAL FLOWS

by

Chengxi Zhao

Thesis

Submitted to the University of Warwick

for the degree of

Doctor of Philosophy

School of Engineering

March 2020

獻給我的家人

Contents

List of Tables

List of Figures

vii

Acknowledgments

First of all, I would like to express my deep and sincere gratitude to my two supervisors, Prof. Duncan Lockerby and Dr. James Sprittles for guiding me into the micro/nano-fluid world. I still remember the welcome hug from Duncan when I just arrived at Warwick, and the coffee invited by James at the first meeting with him in the Maths Institution, wishing me a happy start to my PhD. I enjoyed discussions with them in every office meeting, where I benefited a lot from their broad vision, deep insight, and sparkling inspiration. I admired their research attitudes: always patient, critical and motivated, which will become the criteria in my future career. With their invaluable support, I had a very enjoyable, peaceful and meaningful time during the entire PhD study.

My thanks also go to the colleagues in the 'Micro & Nano flows' group at various institutions in the UK — in particular, to Dr. Livio Gibelli for his help in numerous aspects in my research (e.g., modeling and code debugging) as my 'third supervisor'; to Mr. Yixin Zhang, Dr. Juan Padrino and Dr. Mykyta Chubynsky for their wisdom and useful advice in mathematical modeling; to Mr. Sree Hari P. D., Mr. Martin Nikiforidis and Dr. Rohit Pillai for their kind help in MD modeling; finally to Dr. Matthew K. Borg and Prof. Jason Reese (who unfortunately passed away in 2019) for their valuable suggestions in research orientations and methodologies.

In the meantime, I would like to thank Prof. Peter J. Thomas for chairing all the panel meetings during my PhD study. I like his humour and enjoyed the Wales hiking experience with him and other fluid group members.

I am also grateful for the Chancellor's International Scholarship offered by the University of Warwick and other funding support provided by the EPSRC (grants

Declarations

This thesis is submitted to the University of Warwick in support of my application for the degree of Doctor of Philosophy. It has been composed by myself and has not been submitted in any previous application for any degree.

Parts of this thesis have been published by the author:

Zhao, Chengxi, James E. Sprittles, and Duncan A. Lockerby. Revisiting the Rayleigh-Plateau instability for the nanoscale, *Journal of Fluid Mechanics*, 861 (2019).

Zhao, Chengxi, Duncan A. Lockerby and James E. Sprittles. Dynamics of liquid nano-threads: fluctuation-driven instability and rupture, *Physical Review Fluids*, 5.4 (2020): 044201.

Zhao, Chengxi, James E. Sprittles, and Duncan A. Lockerby. Interface dynamics of nano-filaments, *Droplets 2019*, Durham, UK, 16-18 September 2019.

Abstract

Understanding the influence of thermal fluctuations on nanoscale interfacial flows is crucial to a range of modern and emerging technologies, such as in lab-on-a-chip technology and next-generation 3D printing. In this thesis, effects of thermal fluctuations on two specific flows (nano-jets and bounded nano-films) are studied in detail with: (i) Molecular dynamics (MD) used as 'numerical experiments'; and (ii) Landau-Lifshtz Navier-Stokes equations (LLNS, also known as fluctuating hydrodynamics equations) as an approximate, but numerically efficient, alternative. To pursue theoretical results and relatively cheap numerical solutions, further simplifications to LLNS equations, which use a long-wave approximation, are studied: (i) the stochastic lubrication equation (SLE) for nano-jets; and (ii) the stochastic thin-film equation (STFE) for bounded nano-films.

The famous Rayleigh-Plateau (RP) theory is re-evaluated and revised for the instability of nanoscale jets, where MD experiments demonstrate its inadequacy. A new framework based on the SLE is developed, which captures nanoscale flow features and highlights the critical role of thermal fluctuations at small scales. Remarkably, the model indicates that classically stable (i.e. 'fat') liquid cylinders can be broken at the nanoscale, and this is confirmed by MD.

A simple and robust numerical scheme is then developed for the SLE, which is validated against MD for both the initial (linear) instability and the nonlinear rupture process. Particular attention is paid to the rupture process and its statistics, where the double-cone profile reported by Moseler & Landmann [1] is observed, as well as other distinct profile forms depending on the flow conditions. Comparison to the similarity solution in Eggers [2], a power law of the minimum thread radius against time to rupture, shows agreement only at low surface tension; indicating that surface tension cannot generally be neglected when considering rupture dynamics.

For bounded nano-films, STFEs are developed to accommodate substrate roughness and slip boundary conditions (BCs). An efficient solver with a new iteration method, verified by the theoretical models, is then developed to explore the nonlinear dynamics of nano-droplet spreading and coalescence. Numerical solutions of the spreading denote that the slip BC accelerates the process in both the deterministic and stochastic regimes, which is supported by the power laws of the similarity solutions derived. Additionally, thermal noise is shown to decelerate the coalescence, which is confirmed by MD.

Abbreviations

x, y, z	$[\mathrm{m}]$	Cartesian coordinates
z, r, ϕ	$[\mathrm{m}, \mathrm{m}, \mathrm{rad}]$	cylindrical coordinates
u, v, w	$\left[\mathrm{m\,s^{-1}}\right]$	velocities in different directions
p	$\left[\mathrm{kg\,m^{-1}\,s^{-2}}\right]$	pressure
ρ	$\left[\mathrm{kg\,m^{-3}}\right]$	liquid density
μ	$\left[\mathrm{kg\,m^{-1}\,s^{-1}}\right]$	dynamic viscosity
ν	$\left[\mathrm{m^2\,s^{-1}}\right]$	kinematic viscosity
γ	$\left[\mathrm{kg\,s^{-2}}\right]$	surface tension
T	$[\mathrm{K}]$	temperature
k_{B}	$\left[\mathrm{kg\,m^2\,s^{-2}\,K^{-1}}\right]$	Boltzmann constant
t	$[\mathrm{s}]$	time
h	$[\mathrm{m}]$	interface height
L	$[\mathrm{m}]$	length of liquid threads / thin-films
r_0	$[\mathrm{m}]$	initial radii of liquid threads/cylinders
h_0	$[\mathrm{m}]$	initial height of thin-film
W	$[\mathrm{m}]$	width of quasi-one-dimensional thin-films
τ	$\left[\mathrm{kg\,m^{-1}\,s^{-2}}\right]$	shear stress
S	$\left[\mathrm{kg\,m^{-1}\,s^{-2}}\right]$	stochastic shear stress
ω	$\left[\mathrm{s^{-1}}\right]$	growth rate of perturbation
k	$\left[\mathrm{m^{-1}}\right]$	wavenumber
λ	$[\mathrm{m}]$	wavelength

$\mathcal{N}$	$\left[\mathrm{m}^{-1/2}\,\mathrm{s}^{-1/2}\right]$	Gaussian distributed noise
f	$[\mathrm{m}]$	solid shape functions
β	$[\mathrm{m}]$	slip length
P	$\left[\mathrm{kg}\,\mathrm{m}^{-1}\,\mathrm{s}^{-2}\right]$	pressure tensors
σ	$[\mathrm{m}]$	potential distance
ϵ	$\left[\mathrm{kg}\,\mathrm{m}^{2}\,\mathrm{s}^{-2}\right]$	depth of the potential well
$\mathbf{r}_i$	$[\mathrm{m}]$	position of molecule
$\mathbf{v}_i$	$\left[\mathrm{m}\,\mathrm{s}^{-1}\right]$	velocity of molecule
$\mathbf{a}_i$	$\left[\mathrm{s}^{-1}\right]$	acceleration of molecule
$\mathbf{f}_i$	$\left[\mathrm{kg}\,\mathrm{m}\,\mathrm{s}^{-2}\right]$	interaction forces between molecules
m_i	$[\mathrm{kg}]$	mass of molecule
$\mathcal{U}$	$\left[\mathrm{kg}\,\mathrm{m}^{2}\,\mathrm{s}^{-2}\right]$	interaction potential

NS	Navier-Stokes equations
LLNS	Landau-Lifshitz Navier-Stokes equations
LE	lubrication equaion
SLE	stochastic lubrication equaion
TFE	thin-film equation
STFE	stochastic thin-film equation
RP	Rayleigh-Plateau
TCW	thermal capillary waves
PSD	power spectral density
ODE	ordinary differential equation
PDE	partial differential equation
SPDE	stochastic partial differential equation
RHS	right hand side
Re	Reynolds number
Oh	Ohnesorge number
Th	thermal-fluctuation number
MD	molecular dynamics
NVE	microcanonical ensemble
NVT	canonical ensemble
LJ	Lennard Jones potential

Chapter 1

Introduction

1.1 Background

Interfacial flows are ubiquitous in every natural and industrial phenomenon where liquids are involved, (e.g. in the breakup of jets, coalescence of droplets and dewetting of thin-films). Therefore, understanding the behaviour of interfacial flows is crucial to a range of technologies, such as ink-jet printing [3], fibre manufacture [4] and drug delivery [5]. Macroscopic interfacial flows have been widely studied, with numerous properties derived [6, 7] which have predicted physics, improved existing technologies and designed new ones.
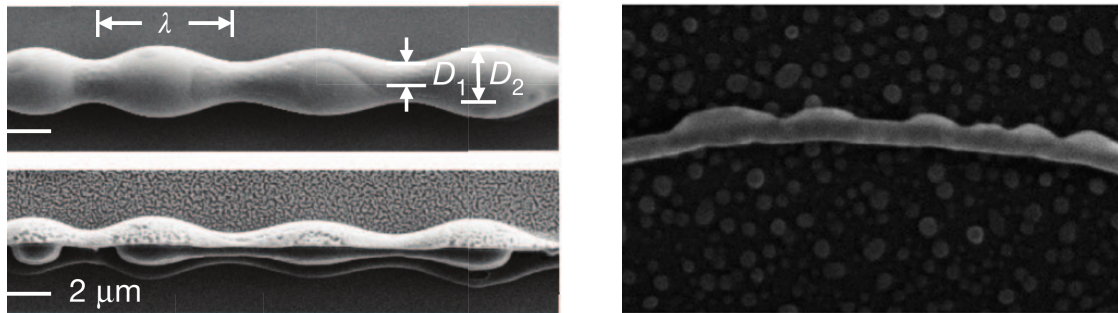
Figure 1.1: Application of the nanoscale Rayleigh-Plateau (RP) dynamics in modern manufacture. Left panel: SEM image of polymer-core/glass-shell spherical particle fabrication by RP dynamics, taken from [8]. Right panel: RP crystal growth of germanium periodic shells on silicon nanowire cores, taken from [9].

Driven by the trend for miniaturisation in industry, interfacial flows are required to be manipulated at the micro/nano-scale in some modern technologies, like lab-on-chip [10], high-resolution 3D printing with nano-jets [11], drug manufacturing [8] (see the left

panel in Figure 1.1) and nanowire fabrication [12, 9] (see the right panel in Figure 1.1). So, the validity of the macroscopic theories for nanoscale interface dynamics has recently been brought into question; due mainly to the extra physical factors at the molecular scale. One significant factor is thermal fluctuations, which come from the random thermal motions of molecules. The first direct visual observation of these fluctuations in interfacial flows was shown in [13], where a rough structure of a gas-liquid interface in a phase-separated colloid-polymer mixture (with ultralow surface tension) was imaged by laser scanning confocal microscopy (LSCM) (see Figure 1.2). The influence of thermal fluctuations is usually negligible in the macroscopic fluids after spatial and temporal ensembling, while at the nanoscale it plays an important role [14]; especially in the interfacial flows, which is the theme of this work.
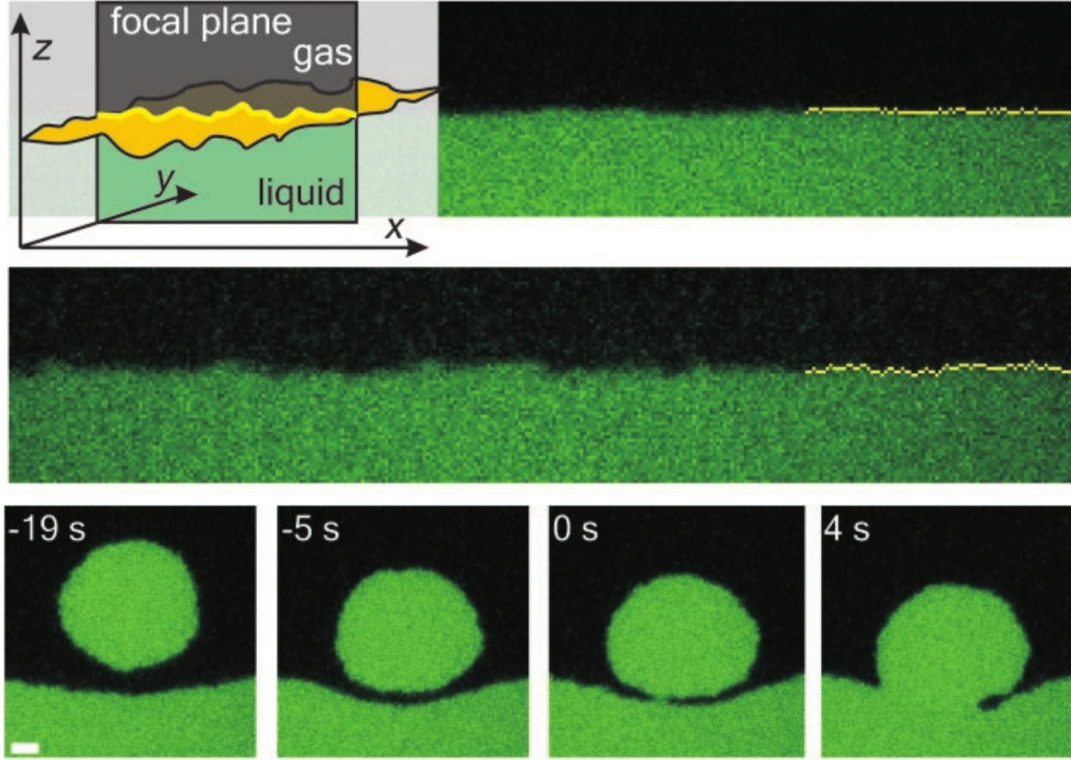
Figure 1.2: Thermal capillary waves (TCW) at the liquid-gas interface imaged with LSCM. A thin-film interface is presented in the upper figures, while lower figures show the coalescence of colloidal liquid droplets with the bulk liquid phase, reproduced from [13].

To predict the behaviour of these fluctuations in interfacial flows, two models will be employed in this thesis. One is molecular dynamics (MD), used as 'numerical

experiments'. The other model, which was first proposed by Landau & Lifshitz [15], are the fluctuating hydrodynamics equations, where stochastic shear stress terms are added to the Navier-Stokes equations. These stochastic PDEs will be simplified with lubrication approximations to pursue theoretical and more-efficient numerical solutions for further understanding of nanoscale interfacial flows.

1.2 Thesis outline

In this work, we focus on two specific kinds of interfacial flow at the nanoscale: (i) nano-jets and (ii) nano 'bounded' thin-films, whose dynamics are explored by the two models mentioned above. The thesis is organised as follows:

- Chapter 2 is a literature review on the current state-of-the-art in understanding and modelling the two kinds of interfacial flows that we concentrate on. Here, classical models at the macroscale are first reviewed, followed by a survey of the literature on the influence of thermal noise in nano-jets and nano-film flows, respectively, in which the existence of several unanswered questions generates the motivation for the research in the following chapters.

- In Chapter 3, details of the above-mentioned two models are introduced. First, we describe the basic framework of MD and the different molecular models used in this work, with some validation tests in Section 3.1. Then, the long-wave/lubrication approximation is used to derive stochastic lubrication equations (SLE) for nano-jets and two new stochastic thin-film equations (STFE), with additional substrate physics taken into account.

- In Chapter 4, we revisit the Rayleigh-Plateau instability at the nanoscale to explore how thermal fluctuations affect the famous jet-flow instability.

- In Chapter 5, a reliable SLE solver is proposed and developed, validated by MD results, that uses a simple correlated noise model to achieve grid-size/time-step convergence. Furthermore, the solver is applied to explore the statistics of the behaviour of nano-thread rupture, whose ensemble averages are compared with the well-known similarity solutions.

- In Chapter 6, an efficient STFE solver is developed in the Crank-Nicolson framework, with a new iteration method proposed. This solver is verified by analytical solutions for both deterministic and stochastic cases. The solver is then employed

to explore two interesting bounded thin-film flows: (i) nanodroplet spreading and (ii) nanodroplet coalescence.

- Chapter 7 summarises the work done in this study and gives suggestions for future work.

Chapter 2

Literature review

In this chapter, we carry out a literature review of the two specific interfacial flows of interest: (i) jet flows and (ii) bounded thin-film flows. In Section 2.1, (deterministic) classical models are reviewed, while findings for challenges at the nanoscale are introduced in Section 2.2.

2.1 Classical models

2.1.1 Jet-flow dynamics

In classical fluid dynamics theories, jet flows are studied to explain how a falling liquid thread/cylinder breaks up into smaller droplets with less surface, but with its volume conserved. This process is usually divided into two stages, where good analytical progress has been made [16]: (i) the initial (linear) instability generation and (ii) the nonlinear rupture dynamics.
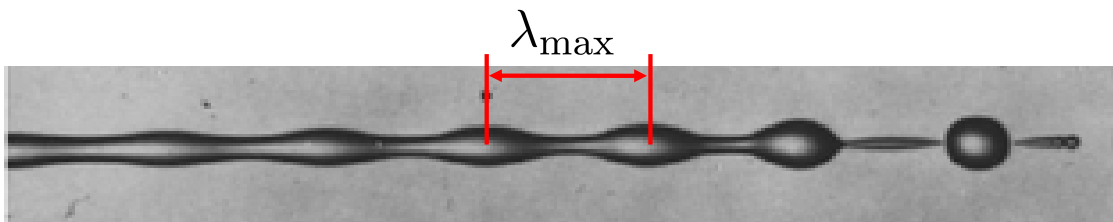
Figure 2.1: Instability of a jet flow from an experiment, reproduced from [17]

The instability mainly focuses on the growth/dissipation of the initial perturbation waves (see Figure 2.1). The earliest research for this topic dates back to about 140 years ago, when Plateau [18] concluded that only long-wave perturbations are unstable

5

with a critical wavelength, $\lambda_{\mathrm{crit}} = 2\pi r_0$, beneath which all the interface disturbances decay. Here, r_0 is the initial radius of jet-flows. Then Rayleigh [19, 20] conducted a linear stability analysis on the inviscid axisymmetric NS equation to find a fastest-growing mode with wavelength $\lambda_{\mathrm{max}} = 9.01 r_0$ (or wavenumber $k_{\mathrm{max}} = 0.697/r_0$). To acknowledge both of their brilliant contributions, the instability of jet flows is usually referred to as the 'Rayleigh-Plateau' (RP) instability. Since this original work, the RP theoretical framework has been subjected to numerous generalisations with more physical factors taken into account (e.g. viscosity [21] and ambient flows [22]). Although a 'real' jet flow is more complicated, with both temporal and spatial instability, the RP theories have been shown to provide not only nice analytical predictions [23], but also accurate descriptions of macroscopic experiments [24] and numerical solutions for the full nonlinear NS equation [25].

Despite the useful theoretical models derived from the axisymmetric NS equation in the linear stages of growth, it is difficult to obtain analytical solutions for rupture dynamics with strong nonlinearity. To solve this problem, Lee developed a one-dimensional equation with the quasi-stationary stream analysis [26], but only considered the inviscid case. Then Bogy took the viscosity into consideration with a complicated theoretical structure, which has not been found to have a clear connection with the NS equation [27]. The most famous one-dimensional model was proposed by Eggers & Dupont [28] with the 'lubrication approximation' applied to the axisymmetric NS equation. This lubrication equation (LE) has been solved numerically to predict the nonlinear rupture dynamics, where good agreement was obtained with the experimental data [29] and the numerical results for the full three-dimensional NS equation [30].

Based on the LE, three different scaling theories have been developed to describe the dynamics in the vicinity of the pinch-off singularity:

- the inertial regime (I-regime), where inertial and capillary forces are comparable (viscous forces are weak) [31];

- the viscous regime (V-regime), where viscous and capillary forces are comparable (inertial forces are weak) [32, 33];

- the viscous-inertial universal regime (VI-regime), where viscous, capillary and inertial forces are all comparable [34].

The three regimes can be distinguished by the Ohnesorge number, $\mathrm{Oh} = \mu/\sqrt{\rho\gamma r_0}$, with the scaling laws for the time evolution of minimal thread radius, $h_{\mathrm{min}}(t)$. The results are presented in Table 2.1, where t_{b} is defined as the breakup(rupture) time.

I-regime	Oh$\ll 1$	$h_{\min} \sim (t_b - t)^{2/3}$
V-regime	Oh$\gg 1$	$h_{\min} \sim 0.0709\,(t_b - t)$
VI-regime	Oh≈ 1	$h_{\min} \sim 0.0304\,(t_b - t)$

Table 2.1: Scaling theories near rupture in different regimes.
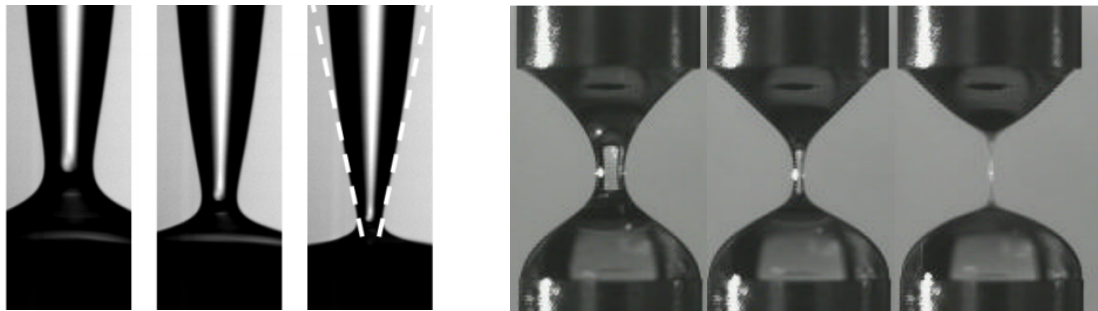
Figure 2.2: Rupture profiles of different liquids. Left panel: asymmetric pinching-off profiles of a dripping water droplet (Oh$\ll 1$), taken from [35]; Right panel: symmetric pinching-off profiles of a glycerol filament (Oh$\gg 1$), taken from [36].

The scaling laws of $h_{\min}(t)$ for I-regime and V-regime above have been proved experimentally with different types of rupture profiles: (i) a cone shape with angles of 18.1° and 112.8° (see the left panel in Figure 2.2) [35]; and (ii) a long-thread shape (see the right panel in Figure 2.2) [36]. However, since the local Oh varies at different time instances in the rupture, the dynamics in reality are more complicated than expected. It has been found that no matter which regime the pinching-off starts in, it will end up in the VI-regime at the final stage [37], so that there are two transitions: (i) inertial to viscous-inertial (I $\rightarrow$ VI) transition, first proved numerically in [38], and (ii) viscous to viscous-inertial (V $\rightarrow$ VI) transition, already found experimentally in [39]. Moreover, more complex cases have been studied by Castrejón-Pita [40] with both experiments and numerical simulations, where multiple regime transitions (i.e. V $\rightarrow$ I $\rightarrow$ V $\rightarrow$ IV) have been discovered. A recent study [41] focused on the transition between different similarity solutions and demonstrated that the '*transient regime undergoes unexpected log-scale oscillations that delay dramatically the onset of the final self-similar solution*' experimentally, first discovered by Li & Sprittles numerically [37].

7

2.1.2 Bounded film flows

Another fluid configuration, bounded planar thin-film flows, are also common in both nature and technologies with a variety of interesting dynamics such as wave propagation of falling films [42], finger-like structures in dewetting [43] and under-compressive shocks of the advancing contact lines [44]. In this section, we prefer to review thin-film instability/rupture, one fundamental behaviour, rather than the complicated ones above, mainly to present theoretical understandings of the dynamics and establish a connection with effects at small scales.

Thin-film breakup was first observed in experiments done by Reiter [45] with liquid polystyrene on silicon substrates, where some holes appeared after the breakup. The holes then grew with ridges formed ahead of them, which ultimately contacted each other, creating 'cellular' structures. Due to the RP instability, the ridges were unstable and finally broke up into droplets, the sizes of which were found to depend on the contact angles [46].

The theoretical works for thin-film instability far pre-date the experimental studies mentioned above, and were done by Vrij [47] and Sheludko [48], who pointed out that instability is driven by intermolecular forces. However, their models came from the free energy equation, in which no clear connection with the NS equation was found. Ruckenstein & Jain [49] used linear stability analysis of the NS equation to get the critical and fastest-growing wavelengths of interface perturbations.

A full nonlinear model, the thin-film equation(TFE) was first proposed by William & Davis [50] using long-wave/lubrication approximation to simplify the NS equation. In this model, an additional disjoining pressure term was supplemented to represent the intermolecular interactions between the solid-liquid and liquid-gas interfaces. Assuming an explicit expression for the disjoining pressure term, we can not only conduct linear stability analysis on the TFE to get the scaling of the perturbation wavelength and its growth rate as a function of the initial uniform film thickness [51], but also pursue a similarity solution to predict the final rupture dynamics [52]. This unstable (rupture) mechanism is known as 'spinodal dewetting' [53].

After the earliest experimental work done by Reiter [45, 46], Jacobs et al. [54] saw that the holes, similar to the findings in Reiter's work [45], had a Poisson distribution, which did not agree with the predictions from the spinodal dewetting. Moreover, the instabilities were found to be caused by defects on the substrate or inside the film itself, denoting another unstable mechanism, defined as 'nucleation dewetting'. Spinodal dewetting was first observed in experiments done by Bischof et al.[55] using liquid

gold films on quartz substrates. Besides the two mechanisms achieved, Seemann et al. [56] conducted a series of experiments with well-controlled film properties to alter the interface potential, and revealed another unstable mechanism, thermal nucleation. In summary, the thin film would break up due to three mechanisms [57]:

(i) spinodal dewetting due to the molecular interations (van der Waals forces);

(ii) heterogeneous nucleations around defects of films/substrates ;

(iii) thermal nucleations around random holes.
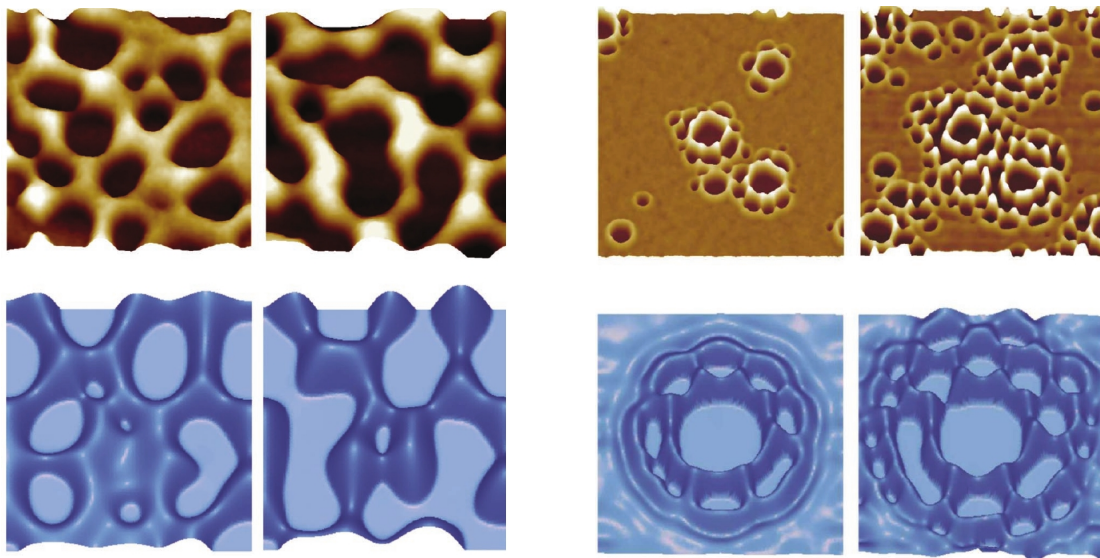
Figure 2.3: Dewetting of ultrathin films, taken from [58]. Upper figures with khaki backgrounds are the AFM images of a polystyrene film on a silicon wafer, while the lower figures with dark-blue backgrounds show the numerical solutions for the TFE. Left panel: $h_0 = 3.9$ nm at $T = 326$ K; Right panel: $h_0 = 4.9$ nm at $T = 343$ K.

In reality, film dewetting is usually more complicated due to potential combinations of different mechanisms. For example, Figure 2.3 shows two rupture patterns, done by Becker et al. [58] both experimentally and numerically. Note that the difference mainly arises from the initial height of the film. The thinner case (left panel in Figure 2.3) breaks up only due to spinodal dewetting, while for the thicker one (right panel in Figure 2.3), heterogeneous nucleations 'pre-empt' the onset of instability at the initial stage, while spinodal dewetting 'kicks in' later. Also, good agreement between experimental observations and numerical predictions was obtained in [58], with the caveat that the numerical predictions were slower than the experimental results. This mismatch

9

was probably caused by a nanoscale factor (e.g. thermal fluctuations) which was not included in the TFE. More explanations will be reviewed in section § 2.2.2.

2.2 Challenges from thermal fluctuations at the nanoscale

As noted in Chapter 1, extra physical factors at the molecular scale could be crucial to nano-fluid dynamics. The factor we concentrate on in this work is thermal fluctuations (due to random molecular motions), which have been found to have a significant effect on the dynamics of a wide range of nano-fluids, such as fluid mixing (Rayleigh-Taylor instability) [59], moving contact lines [60, 61, 62], droplet coalescence [63] and fluidic transport in the carbon nanotubes [64]. There is therefore cause to reassess the validity of the classical models (introduced in Section 2.1) at the nanoscale and to question the theories behind long-held beliefs. In this section, we conduct a review of the current state-of-the-art literature concerning the influence of thermal fluctuations on nano-jets (§ 2.2.1) and nano-films (§ 2.2.2), respectively.

2.2.1 Nano-jets

The earliest works of nano-thread dynamics date back to 1993 [65] with MD applied to simulate a short nano-thread, where numerical results of rupture time were found to be of the same order of magnitude as predicted by the RP instability. Then, in 1998, Kawano [66] undertook MD simulations for long threads and obtained a similar agreement of rupture time. However, the dominant wavenumbers ($0.386 \sim 0.50$) extracted from the MD results were significantly smaller than that (0.697) of RP theory.

Breakthroughs in this area were made at the beginning of the 21st century. In 2000 in an article in Science, Moseler & Landman [1] used MD simulations of nanoscale jets to discover a rupture profile not described by macroscopic theory: a double-cone profile (see the left panel in Figure 2.4) was observed at rupture, a phenomenon attributed to thermal fluctuations that are negligible at usual engineering scales. This behaviour was described using a stochastic lubrication equation (SLE) derived by applying the lubrication approximation to the fluctuating hydrodynamics equations [15].

A 'nanoscale' similarity solution was then derived by Eggers [2] for the SLE to reproduce the double-cone profile observed by Moseler & Landman and to obtain a power law for the time resolution of minimum radius, i.e. $h_{\min}(t) \sim (t_{\mathrm{b}} - t)^{0.418}$, totally different from the macroscopic ones in Table 2.1. The rupture profiles and power law were further

10

confirmed by physical experiments using specially prepared low-surface-tension liquid-liquid combinations that enhanced fluctuations [67, 68] (see right panel in Figure 2.4), further MD simulations [69, 70] and dissipative-particle-dynamics (DPD) simulations used as a coarse-graining version of MD [71]. Interestingly, this specific double-cone profile could even be discovered in falling granular streams at the macroscale [72], where the shape of macroscopic particles is modified to control the cohesive forces between these particles.
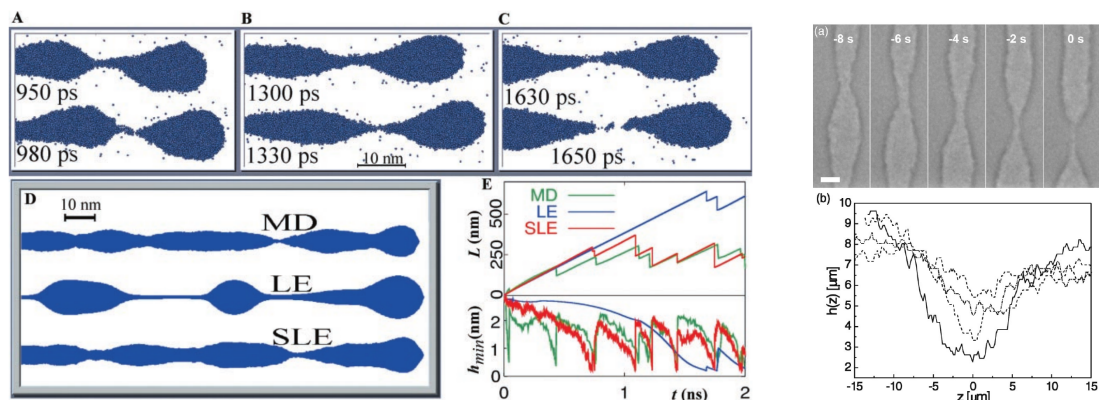
Figure 2.4: Nanoscale jet breakup. Left panel: numerical results from different models, reproduced from [1]; Right panel: experimental rupture profiles, reproduced from [67].

Despite major advances made in the study of nano-jet flows, many open problems remain. One is whether the RP instability mechanism is valid in the presence of thermal fluctuations at the nanoscale. Although the earliest work (1993) [65] concluded that '*fluctuations substantially distort the shape of the cylinder*', Min & Wong (2006) [73] claimed that the Plateau stability criterion [18] held even at the molecular scale with MD simulations. In a recent study [74], mean dominant wavenumbers obtained from MD results were found to be significantly smaller than the Rayleigh prediction ($k_{max} = 0.697/r_0$), coinciding with the results in [66]. However, Rayleigh's theory is correct for inviscid fluid with $Oh \ll 1$, while at the nanoscale, Oh is usually larger than 1, namely, the viscous effect is non-negligible, thus leading to $k_{max} < 0.697/r_0$ obtained from the viscous instability theory [21, 22, 28]. So the deviations between MD and Rayleigh's predictions in [66, 74] are not necessarily caused by additional nanoscale effects. Mo et al. [75] then carried out a series of DPD simulations with various Oh numbers (or Reynold numbers) and found that their numerical results did not match with the viscous instability theory [22]. Interestingly, the DPD results showed that perturbation with the wavenumber, $kr_0 > 1$, still grew, challenging the Plateau stable boundary. But it is a

pity not to see any further theoretical analyses after that. Recently, a fluctuating lattice Boltzmann model was applied to solve the three-dimensional LLNS, and to investigate the influence of fluctuations on the distribution of droplet volumes after the breakup of a nanoligament, which was found to depend on two relevant length scales, i.e., the thermal length scale and ligament size [76]. However, the connections between the RP instabilities and the distribution of droplet volumes are not straightforward due to non-negligible effects of nonlinearity at the final stage of breakup (before droplet formation). Therefore, currently, it is still unclear how the thermal fluctuations affect instability, motivating the research work in Chapter 4.

Another doubt is about numerical solutions for the SLE, which is, seemingly, an efficient and powerful tool to explore the rupture dynamics of nano-threads. But, surprisingly, there are no detailed numerical SLE studies in the previous literature, , the considerations in [1, 70] only presented qualitative comparisons between MD and selected SLE realisations. However, the SLE is stochastic, and many independent solutions are needed in order to (i) verify that the statistics of these solutions are well described by the SLE (in comparison with MD); and (ii) understand the statistics of the rupture process, especially the accuracy of the 'universal profile' in the similarity solution and the validity of the assumptions made (e.g. negligible surface tension) in Eggers' paper [2]. Moreover, macroscopic experiments and models reviewed in § 2.1.1 denote that pinching-off is a very complicated process with transitions between different 'regimes'. The transition process would become more complex with a new 'fluctuation-dominated regime' added at the nanoscale. Pioneering work by Mo et al. [77], with DPD simulations, discovered a crossover from the I-regime to a fluctuation regime. However, the numerical prediction for each case in [77] was from just one realisation. To reach more reliable conclusions, more independent realisations are required to be performed. Additionally, 'V-regime' and 'VI-regime' with viscous forces were not taken into account in the work of Mo et al., despite their importance at the nanoscale. Both these flaws made their findings less convincing. Therefore, it is interesting to develop a reliable SLE solver to explore the complicated rupture dynamics of nano-threads, which is the main target of the work in Chapter 5.

2.2.2 Nano-film flows

To take the influence of thermal noise on thin-film flows into account, Grün et al. [78] rigorously (in contrast to the SLE) derived a stochastic thin-film equation (STFE) with a lubrication/long-wave approximation (similar to the approach used in § 2.1.2) applied

to the full fluctuating hydrodynamics equations. The STFE was then solved numerically to demonstrate that the fluctuations can accelerate the rupture of thin films, providing a probable explanation for the mismatch between the TFE predictions and experimental data in [58] mentioned at the end of § 2.1.2.

In a later work [79], instability analysis was conducted on the STFE to obtain a spectrum for the thermal capillary waves (TCW) in thin-film flows, and indicated that thermal noise changes the TCW from an exponential decay to a power law for large wavevectors, confirmed by the experiments on the dewetting of polymer films [80]. However, due to the limitations of measurement techniques, the initial film roughness and characteristic time scale in [80] cannot be obtained directly from the experiments, thus leading to fitting parameters to match the experimental data with the theoretical model in [79] and making the demonstration in [80] less reliable. As 'numerical experiments', MD is another powerful tool to demonstrate the TCW theory in [79], first done by Willis & Freund [81] in 2010 with a short Lennard-Jones polymers model. Recently, multiple independent MD simulations (realisations) were performed in our group to obtain averaged spectra to validate the 'advanced' TCW theory proposed by Zhang et al. [82], with the power spectra at different time instances explicitly calculated.

Besides the linear theoretical models, several numerical studies have been carried out to explore the dynamics further. One numerical finding was that thermal noise reduced the number of droplets formed after rupture, but increased the variability in size and space distribution [83]. Diez et al. [84] supplemented the original STFE frame with a spatially correlated noise model (to replace the perfectly uncorrelated noise that is widely used) and then solved the 'new' STFE both theoretically and numerically to compare with their experimental data, followed by another numerical study with perfectly correlated noise along the wall-normal direction [85]. In addition, for a more practical purpose, the three-dimensional STFE were solved by Pahlavan et al. [86] to show complicated three-dimensional dewetting patterns and droplet coalescence after long-time simulations. In a recent work [87], the STFE was also applied to numerically explore a thin non-planar film rupture subjected to drainage, showing scaling laws of both a 'dimple-dominated regime' and the 'fluctuation-dominated regime'.

The STFE can also be employed to investigate other bounded flows besides the film rupture, mainly concerning nonlinear dynamics. One instance is the droplet spreading on the substrate at the nanoscale, which was first investigated by Davidovitch et al. [88] in 2005. In their work, similarity solutions were derived to describe the dynamics with two regimes with a corresponding power law for the typical droplet width: (i) 'surface-tension dominated regime' with Tanner's law, $\ell \sim t^{1/7}$ (first proposed in

[89]); and (ii) 'fluctuation-dominated regime' with the stochastic law, $\ell \sim t^{1/4}$, followed by another numerical work for the STFE with the gravity forces and contact angles taken into account [90]. MD was also performed by Willis & Freund [91] to examine the fluctuation-dominated regime, where faster spreading due to the thermal noise predicted by MD matched the numerical solutions for the STFE very well. But the stochastic power law was not seen, probably because it takes several decades in time to dominate, which was too computationally expensive in MD.

Remarkably, the spreading is the only nonlinear behaviour that has been investigated with the STFE, while the TFE has been widely used for various nonlinear dynamics, such as film rupture [52], bounded droplet coalescence [92] and step-film dissipation [93, 94]. Therefore, it would be interesting to use the STFE for more film flow configurations to explore how thermal fluctuations affect nonlinear dynamics at the nanoscale. Some preliminary tests will be carried out in Chapter 6. Another problem worth investigating further is the solid boundary condition. The current STFE was derived with perfectly smooth substrates and no-slip boundary condition, which is not always the case in reality. Since previous works have developed 'advanced' TFEs considering the influence of substrate roughness [95] and the slip boundary condition [51], respectively, it would be feasible to derive 'advanced' STFEs with the two boundary effects, which will be done in Chapter 3.

2.3 Summary

In this chapter, a literature review has been conducted on multiscale dynamics for two specific interfacial flows, jet flows and bounded-film flows, highlighting the influence of thermal fluctuations at the nanoscale. Several unclear issues motivate the work in the following chapters, summarised as:

- Chapter 3: develop an 'advanced' STFE frame with solid boundary effects (e.g., surface roughness and slip boundary condition) taken into account;

- Chapter 4: explore how thermal fluctuations affect the RP instability at the nanoscale;

- Chapter 5: develop a reliable SLE solver and investigate the statistics of nano-thread rupture;

- Chapter 6: study nonlinear dynamics of different film flows at the nanoscale (i.e. nanodroplet spreading and nanodroplet coalescence).

Chapter 3

Numerical models

In this chapter, we introduce two models employed in this thesis used to explore the role of fluctuations at the nanoscale. The first, Molecular Dynamics (MD), which we utilise as 'numerical experiments' for nanoscale fluids, is described in Section 3.1 with test cases for liquid properties in § 3.1.3. The second, fluctuating hydrodynamics equations (also called Landau-Lifshitz Navier-Stokes (LLNS) equations), are presented in Section 3.2, where the lubrication approximation is applied to derive the SLE for nanojets (§ 3.2.2) and the STFE for thin-films (§ 3.2.3).

3.1 Molecular dynamics simulations

Molecular dynamics (MD) is a computational method which obtains statistical properties of an ensemble of molecules [96] by calculating the trajectories of numerous molecules. Since computational capabilities have increased rapidly recently, MD has been successfully applied in different areas, such as biology [97], material sciences [98] and plasma [99]. The earliest MD study of liquid properties can be found in a 1957 paper [100], using hard sphere molecular models. Recently, it has been used to explore the physics of nano-fluids, e.g., liquid transportation in carbon nanotubes [101], wetting [102] and interface dynamics (introduced in Section 2.2) with more complicated molecular models.

In this section, MD techniques used in the thesis are introduced, including the governing equations, a numerical scheme to solve the equations (§ 3.1.1) and interaction functions between molecules (§ 3.1.2). Several simple cases are tested in § 3.1.3 to obtain liquid properties with a well-known MD package, LAMMPS [103].

3.1.1 Basic framework of MD

A molecule contains one or more atoms connected by chemical bonds. In MD, each atom is assumed as a point particle with all mass at the infinitesimally small center point. With these assumptions, the particle motions can be modelled using Newton's equation:

$$\frac{\mathrm{d}\mathbf{r}_i}{\mathrm{d}t} = \mathbf{v}_i\,, \tag{3.1}$$

$$m_i\frac{\mathrm{d}\mathbf{v}_i}{\mathrm{d}t} = \mathbf{f}_i\,, \tag{3.2}$$

where $\mathbf{r}_i$, $\mathbf{v}_i$, m_i and $\mathbf{f}_i$ are, respectively, the position, velocity, mass and forces of an arbitrary atom i in a system of M atoms (i is the serial number of atoms). The interaction forces are determined by the distance between two atoms and can be calculated using the interaction potential $\mathcal{U}$,

$$\mathbf{f}_i = -\sum_{j=1}^{M} \nabla\mathcal{U}(r_{ij}), \qquad \text{for all } i \neq j\,. \tag{3.3}$$

Here, r_{ij} is the distance between atom i and j, i.e., $r_{ij} = |\mathbf{r}_i - \mathbf{r}_j|$.

Note that $\mathbf{r}_i$, $\mathbf{u}_i$ and $\mathbf{f}_i$ are three-dimensional vectors. Therefore, the whole system is described by $6M$ Newton equations. Since it is difficult to obtain analytic solutions for $6M$ ODEs, efficient algorithms for reliable numerical solutions are needed. One approach is the 'velocity Verlet' algorithm proposed by Swope et al. in 1982 [104]. In this numerical framework, the atomic position ($\mathbf{r}_i$) is explicitly calculated with the velocity at $t + \triangle t/2$ $\left(\mathbf{v}_i^{t+1/2}\right)$, written as,

$$\mathbf{r}_i^{t+1} = \mathbf{r}_i^t + \mathbf{v}_i^{t+1/2}\triangle t = \mathbf{r}_i^t + \left(\mathbf{v}_i^t + \frac{\mathbf{f}_i^t\,\triangle t}{2m_i}\right)\triangle t\,. \tag{3.4}$$

Now, the interatomic forces can be updated with new positions,

$$\mathbf{f}_i^{t+1} = -\frac{\partial}{\partial\mathbf{r}_i^{t+1}}\mathcal{U}(\sum_{j=1}^{M}\mathbf{r}_j^{t+1}) \tag{3.5}$$

and substituting $\mathbf{f}_i^t$ and $\mathbf{f}_i^{t+1}$ into the momentum equation (Equation (3.2)) yields the

velocity at $t + \triangle t$,

$$\mathbf{v}_i^{t+1} = \mathbf{v}_i^t + \frac{\mathbf{a}_i^t + \mathbf{a}_i^{t+1}}{2} \triangle t = \mathbf{v}_i^t + \frac{\mathbf{f}_i^t + \mathbf{f}_i^{t+1}}{2m_i} \triangle t . \tag{3.6}$$

We then move to the next step at $t = t + \triangle t$, repeating the three above steps to advance further.

This 'velocity Verlet' method has been established as an easily programmed, efficient and accurate scheme for MD simulations [103, 105, 106], and thus is widely used in lots of MD packages (e.g. LAMMPS, GROMACS, NAMD).

3.1.2 Molecular models

The interactions in MD can be modelled by a pairwise potential (U), whose type is determined by the molecular structure. The simplest one is the Lennard-Jones (LJ) 12-6 potential [107], widely used in modelling neutral atoms or molecules. Here, the pairwise potential is expressed as

$$\mathsf{U}(r_{ij}) = 4\epsilon \left[\left(\frac{\sigma}{r_{ij}} \right)^{12} - \left(\frac{\sigma}{r_{ij}} \right)^6 \right] , \tag{3.7}$$

where ϵ is the depth of the attractive potential well and σ is the radius of the repulsive core. i and j represent serial numbers of atoms. The LJ potential contains two terms:

(i) the long range attractive (van der Waals) term, r_{ij}^{-6}, due to electron correlations;

(ii) the close range repulsive term, r_{ij}^{-12}, due to overlapping electron clouds.

Fluid	$\sigma(\text{Å})$	ε/k_B (K)	M(g/mol)	T(K)
Xenon	3.90	227.55	131.29	270
Krypton	3.63	162.58	83.80	230
Argon	3.40	116.79	39.95	300

Table 3.1: Potential model parameters and molar mass [108]

.

Figure 3.1 illustrates the LJ potential for three different noble gases (see Table 3.1 for the parameters). Note that the 'bottom' point represents strongest attractive forces between two atoms, where $r_{\text{bottom}} = 2^{1/6}\sigma \approx 1.122\sigma$. Additionally, U tends to 0 when

$r_{ij} \gg \sigma$. So, a cut-off distance r_c is introduced into the numerical framework. When calculating the total interaction forces, contributions from the atoms outside the 'cut-off range' are not taken into account, i.e.,

$$U_{\mathrm{MD}}(r_{ij}) = \begin{cases} \mathsf{U}(r_{ij}) & \text{if} \quad r_{ij} \leq r_c\,, \\ 0 & \text{if} \quad r_{ij} > r_c\,. \end{cases} \tag{3.8}$$

Note that the cut-off distance leads to truncated errors of the force calculation. But, U with $r_c > 2.5\sigma$ (the most common cut-off distance) is smaller than 1.6% of its value at the minimum point$(-\epsilon)$ [109] and will decrease to 0 quickly with the increase of r_c. So it is reasonable to neglect the small truncated errors due to the cutoff.
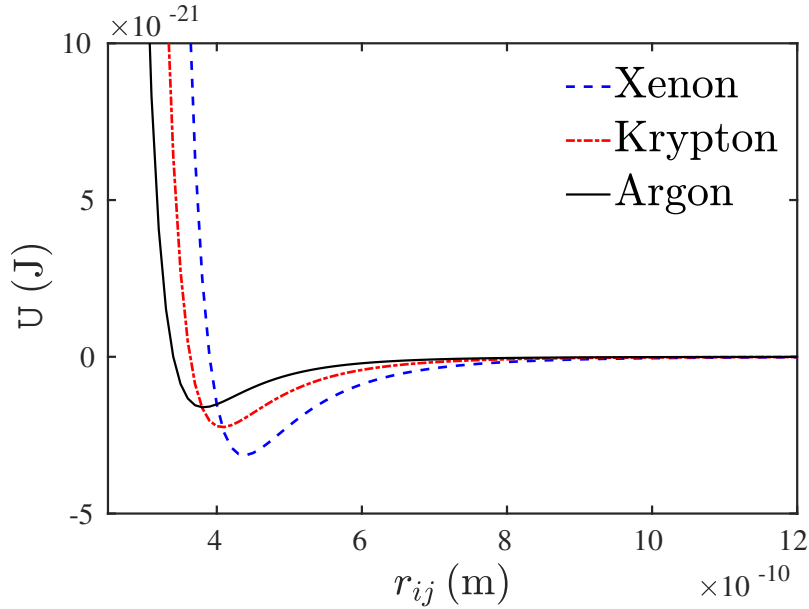
Figure 3.1: The LJ potential for different monatomic molecules.

Despite the simplicity of the LJ potential, it has limited capabilities to describe more 'practical' liquids. For example, liquid argon (an LJ liquid) only exists stably at a very low temperature $(T < 150\,\mathrm{K})$, at which it is very difficult to test experimentally. Turning to more 'practical' liquids raises the requirement for more complicated models. In this thesis, we also employ a well-known water molecular model, TIP4P/2005 [110] to provide more physically 'realistic' predictions.

This rigid water model is constructed based on the Bernal-Fowler geometry (Figure 3.2) with four parts: an oxygen atom (O) with no charge, two hydrogen atoms (H)

18

with a point charge and a massless part (M) with charge. According to experimental data, the O-H distance and H-O-H angle are set as 0.9572Å and 104.52°, respectively. The intermolecular pair potential can be divided into two different types: (i) the Lennard-Jones (LJ) potential and (ii) the Coulomb (electrostatic) potential. So the expression for the pair potential is

$$U(r_{ij}) = 4\epsilon \left[\left(\frac{\sigma}{r_{ij}} \right)^{12} - \left(\frac{\sigma}{r_{ij}} \right)^{6} \right] + \frac{1}{4\pi\varepsilon_0} \frac{q_i q_j}{r_{ij}}, \tag{3.9}$$

where ε_0 represents the vacuum permittivity, q_i and q_j are the atomic charges. i and j are the serial numbers of different kinds of atoms. We list all the parameters for different atoms in Table 3.2. Note that the LJ potential only exists between oxygen atoms (O-O), while there are three pairs of the Coulomb potential, i.e. H-H, H-M and M-M.

Table 3.2: Parameters of the TIP4P/2005 model

Atom	ϵ (kJ mol^{-1})	σ (nm)	$q(e)$
H	0	0	0.5564
O	0.775	0.315	0
M	0	0	-1.112
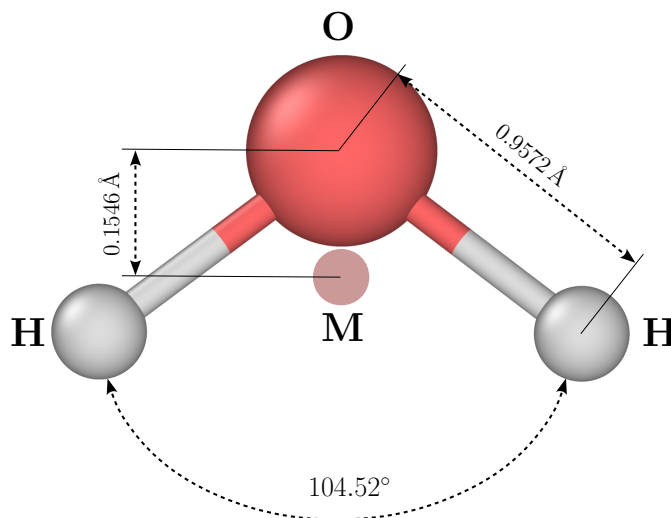
Figure 3.2: Schematic representation of the TIP4P/2005 molecular models for water.

Besides the 4-site water model used in Table 3.2, there are numerous water models developed, such as simpler 3-site models(e.g. SPC/E [111] and TIP3P[112]) or more complicated 5-site models (e.g. ST2 [113] and TIP5P [114]). The main reason we employ

the TIP4P/2005 in this thesis is that it can balance accuracy (compared to the 3-site models) and efficiency (compared to the 5-site models).

Despite the precise predictions of TIP4P/2005, it is not a feasible method for large systems due to the huge computational costs. Therefore, it is necessary to turn to less computationally expensive models (i.e. coarse-grain water models) for the large/long-time simulations. Here, we chose the mW model [115], which mimics the hydrogen-bonded structure of water through the introduction of a non-bond angular dependent term that encourages tetrahedral configurations. The model contains two terms:

(i) ϕ_{ij} depending on the distances between pairs of water molecules (represented by r_{ij} and s_{ik});

(ii) ϕ_{ijk} depending on the angles formed by triplets of water molecules (represented by θ_{ijk}),

where i, j and k represent the serial numbers of coarse grains. The full expression is given by

$$\mathsf{U} = \sum_i \sum_{j>i} \phi_{ij}(r_{ij}) + \sum_i \sum_{j \neq i} \sum_{k>j} \phi_{ijk}(r_{ij}, s_{ik}, \theta_{ijk}), \tag{3.10}$$

$$\phi_{ij}(r_{ij}) = A\epsilon \left[B \left(\frac{\sigma}{r_{ij}} \right)^p - \left(\frac{\sigma}{r_{ij}} \right)^q \right] \exp\left(\frac{\sigma}{r_{ij} - a\sigma} \right),$$

$$\phi_{ijk}(r_{ij}, s_{ik}, \theta_{ijk}) = \kappa\epsilon(\cos\theta_{ijk} - \cos\theta_0)^2 \exp\left(\frac{\chi\sigma}{r_{ij} - a\sigma} \right) \exp\left(\frac{\chi\sigma}{s_{ik} - a\sigma} \right),$$

where A, B, p, q, χ and κ respectively give the form and scale to the potential, and θ_0 represents the tetrahedral angles. All the parameters are presented in Table 3.3.

Table 3.3: Parameters of the mW model

ϵ (kJ mol^{-1})	σ (nm)	A	B	p	q	χ	κ	a	θ_0 (degree)
25.87	0.2390	7.050	0.6022	4	0	1.2	23.15	1.8	109.47

3.1.3 Test cases for liquid properties

To validate the molecular models established in LAMMPS, we carry out several simple tests to calculate two important liquid properties (viscosity represented by μ and surface tension represented by γ), then compare the MD results obtained with experimental data. These two parameters are also widely used in the following chapters to connect the MD results with the fluctuating hydrodynamics models.
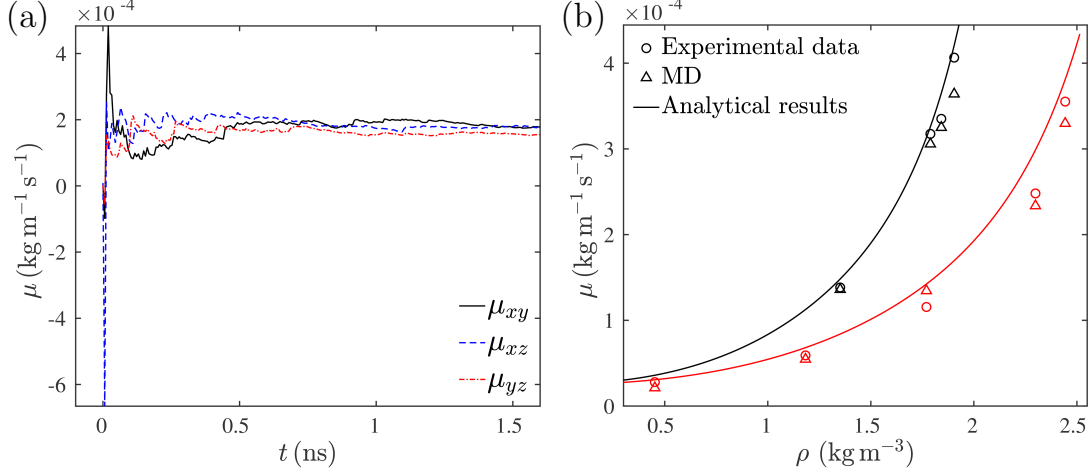
Figure 3.3: Dynamic viscosity from MD with Green-Kubo method. (a) Time history of pressure tensors of Xenon. (b) MD validation for Xenon(black) and Krypton (red). The experimental data comes from [108] and analytical result is derived by Rowley & Painter [116].

For viscosity, we apply the Green-Kubo method [117, 118]. Here, dynamic viscosity can be calculated by integration of the time-autocorrelation function of the off-diagonal elements of the pressure tensors P_{IJ} (Equation (3.11)).

$$\mu_{IJ} = \frac{V_{\text{bulk}}}{k_{\text{B}}T} \int_0^\infty \langle P_{IJ}(t) \cdot P_{IJ}(0) \rangle \, dt \quad (I \neq J), \tag{3.11}$$

where I and J represent Cartesian components of vectors (i.e. x, y, z). V_{bulk} represents the volume of the bulk fluid. The pressure tensors are obtained using the definition in [119] (see Equation (3.12)) and calculated by an in-built function in LAMMPS numerically.

$$P_{IJ} = \left(\sum_{k=1}^N m_k v_{k_I} v_{k_J} + \sum_{k=1}^N r_{k_I} f_{k_J} \right) / V_{\text{bulk}}. \tag{3.12}$$

Here, r_k and f_k are the position and force vector of atom k. N represents the number of atoms in the system.

The first test is performed in a cubic box containing 500 noble gas molecules, with the experimental data found in [108]. The parameters of LJ potential are given in Table 3.1. The cut-off radius is set to $r_c = 4\sigma$ and periodic boundary conditions are used. We use NVT ensembles to get initial equilibrium state with desired density and temperature obtained. After that, the thermostat is turned off and the NVE ensembles

21

are then invoked to calculate the viscosity by averaging the appropriate function. The time history of NVE simulations is illustrated in Figure 3.3(a), with about 20000 time steps for reaching equilibrium and another 50000 for production, where the different line patterns represent μ from different directional components of P. Note that we choose a shorter r_c and fewer time steps compared to the corresponding parameters used in [108] mainly for less computational costs. However, nice convergence still can be found after a long time period of averaging. The final result is the mean value of the three directional components, i.e., $\mu = (\mu_{xy} + \mu_{yz} + \mu_{xz})/3$. Figure 3.3(b) shows good agreement between our MD results (triangular dots) and the experimental data (circular dots) [108] for Xenon and Krypton with different densities. In addition, both can be well predicted by the analytical solutions derived by Rowley & Painter [116], giving us the confidence to apply the Green-Kubo method for more complicated molecules.

(a) $T = 84.09\,\mathrm{K}$

(b) $T = 116.70\,\mathrm{K}$
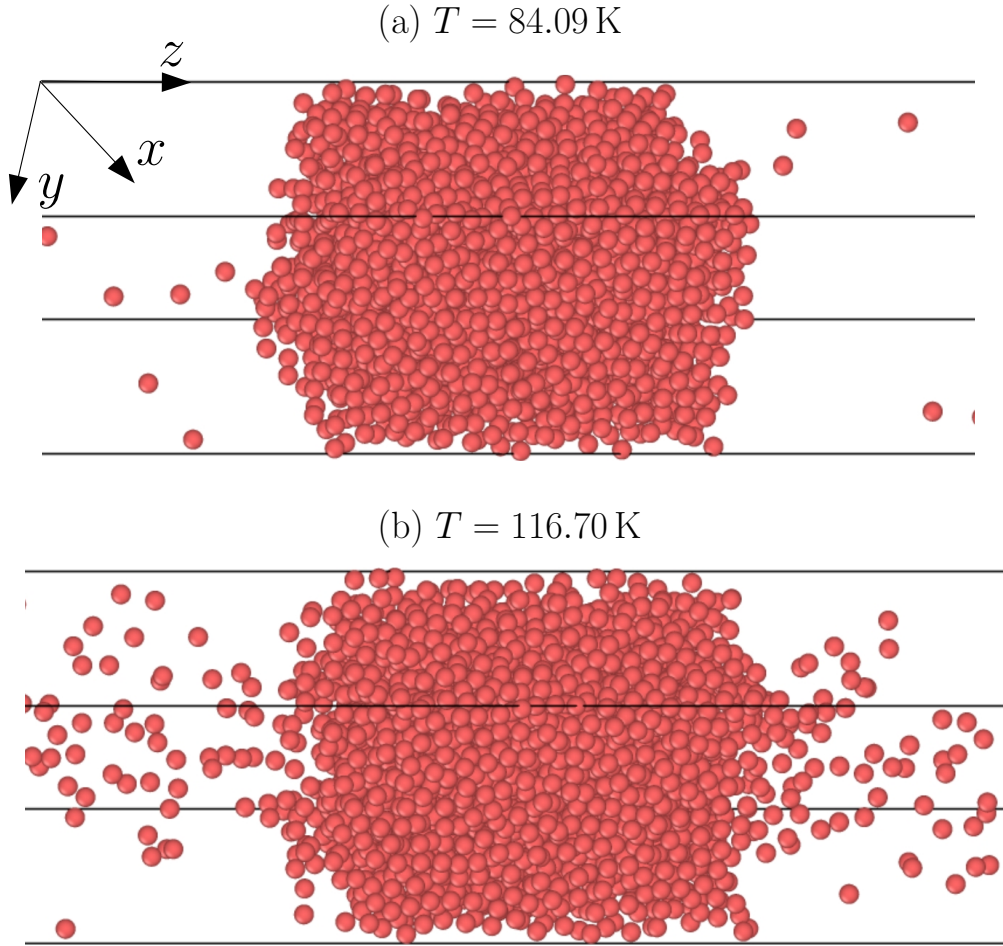
Figure 3.4: Liquid-vapour systems at different temperatures

The second important coefficient is surface tension (γ), which can be obtained from a simple liquid-vapour system (illustrated in Figure 3.4), where a bulk of liquid argon is located in the centre, with the periodic boundary condition. Some liquid molecules evaporate into the vacuum on the two sides, resulting in the liquid-vapour interface. Obviously, a higher temperature leads to more evaporation, modifying the physical properties of the interface.

With similar simulation methods, the equilibrium state can be achieved with the averaged profiles (along the z direction) for both the density and pressure tensor, as shown in Figure 3.5(a). From the density profile, we can find that two thin liquid-vapour interfaces (less than 1 nm) with spikes of the pressure tensor on the two sides. The surface tension is calculated from the profiles of the components of P using the mechanical definition in [120] as,

$$\gamma = \frac{1}{2} \int_0^L [P_\mathrm{n}(z) - P_\mathrm{t}(z)] \, dz \,, \tag{3.13}$$

where subscripts 'n' and 't' denote normal and tangential components, respectively. Here, $P_\mathrm{n} = P_{zz}$ and $P_\mathrm{t} = (P_{xx} + P_{yy})/2$.
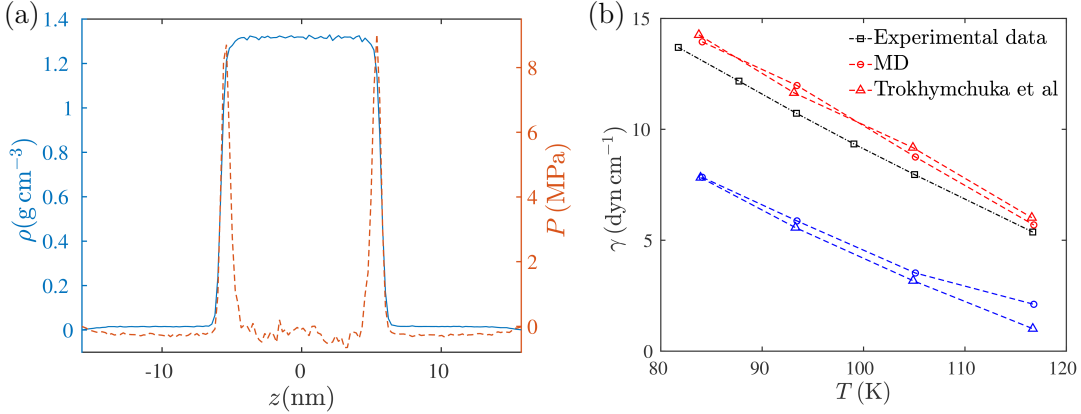
Figure 3.5: MD simulations for surface tension. (a) Density (blue lines) and pressure tensor difference (i.e. $P = P_\mathrm{n} - P_\mathrm{t}$, red lines) distribution at $T = 84.09$ K. (b) MD results with two different cut-off distances: (i) $r_c = 2.5\sigma$ (blue lines) and (ii) $r_c = 5.5\sigma$ (red lines). The black lines are the experimental data. Circle and triangle dots represent MD results from our simulations and data in [121], respectively.

The integral results at different temperature are plotted in Figure 3.5(b) to compare with both experimental data and MD results in [121]. Since Trokhymchuka et al. [121] have also pointed out that the truncation of interactions has an obvious influence

on the predictions for liquid-vapour systems, we carry out the tests with two different cut-off distances, i.e., 2.5σ and 5.5σ. In figure 3.5(b) we see good agreement between our MD results and Trokhymchuka's predictions. Note that the results of larger r_c are closer to the experimental data, meaning that the most common cut-off distance, 2.5σ is not long enough to calculate the interface properties accurately. Therefore, we will always set r_c to be larger than 5σ in this thesis, regardless of the molecule model being used, despite this resulting in more expensive computational costs.

In the same way, we can obtain the γ and μ values of water at different temperatures with the TIP4P/2005 model. The results are shown in Figure 3.6, where good agreement between MD results and experimental data can be obtained.
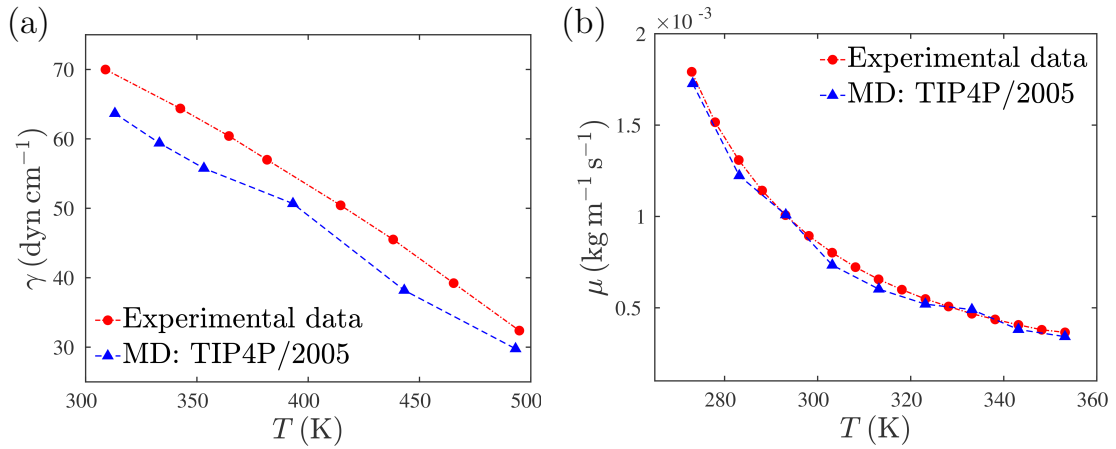
Figure 3.6: Comparison between MD results predicted by the TIP4P/2005 and experimental data. (a) Surface tension at different temperatures. (b) Viscosity at different temperatures.

3.2 Fluctuating hydrodynamics equations

Although MD can provide reliable predictions of nano-fluid dynamics, it has several clear drawbacks. The first is its expensive computational cost, limiting its applicability to very small spatial/temporal scales (e.g, $< 50\,\mathrm{nm}$ / $< 100\,\mathrm{ns}$). Secondly, the options for fluid properties are restrictive. For example, Figure 3.6(b) shows the maximum viscosity of the liquid water is smaller than $2 \times 10^{-3}\,\mathrm{kg\,m^{-1}\,s^{-1}}$. More viscous liquids (e.g. glycerol) can be modelled with a more complicated molecular model (a long-chain structure), but which are more difficult to construct and even worse for computational cost. As a consequence, systematic parametric analysis, usually important in fluid dynamics research, is seemingly not available with MD. Lastly, MD only provides discrete molec-

ular data, for which mathematical techniques cannot be applied to pursue theoretical models (equations/formulas with mathematical variables) directly.

Therefore, it is necessary to turn to PDE models for two reasons:

(i) to explore the dynamics with a wider range of fluid properties (e.g. density, viscosity and surface tension);

(ii) to study fluid properties revealing insight into the influence of thermal fluctuations.

In this section, we will present three SPDE models (fluctuating hydrodynamics equations). In §3.2.1, the three-dimensional LLNS for the interfacial flows are introduced as the basic framework. Then two simplified SPDEs are derived from the LLNS with the long-wave approximation for nano-jet flows (§3.2.2) and bounded thin-film (§3.2.3) at the nanoscale, respectively.

3.2.1 Landau-Lifshitz Navier-Stokes equations for the interfacial flows

In order to take thermal fluctuations into account, Landau and Lifshitz added a stochastic stress flux into the incompressible NS (hydrodynamic) equation to achieve the well-known LLNS [15] equations:

$$\nabla \cdot \boldsymbol{u} = 0 \,, \tag{3.14}$$

$$\rho \left(\partial_t \boldsymbol{u} + \boldsymbol{u} \cdot \nabla \boldsymbol{u} \right) = -\nabla p + \nabla \cdot \boldsymbol{\tau} + \nabla \cdot \boldsymbol{S} \,, \tag{3.15}$$

where $\boldsymbol{S}$ is the stochastic stress term, representing the effect of the molecular thermal motions. Similar to the deterministic stress τ, $\boldsymbol{S}$ is symmetric and trace free, with five independent components (note that the stochastic normal stress tensors are not independent according to the continuity equation), but with a zero mean value for each. If the thermal fluctuations are spatially/temporally uncorrelated, the covariance of $\boldsymbol{S}$ is

$$\left\langle \boldsymbol{S}_{ij}(\mathbf{r}, t) \boldsymbol{S}_{kl}(\acute{\mathbf{r}}, \acute{t}) \right\rangle = 2 \, k_{\mathrm{B}} \, \mu \, T \, \delta(\mathbf{r} - \acute{\mathbf{r}}) \, \delta(t - \acute{t}) \left(\delta_{ik}\delta_{jl} + \delta_{il}\delta_{jk} \right) \,. \tag{3.16}$$

Here, the variables with '´' could be infinitesimally close to the original ones (without '´') in time or space.

Equation (3.14) and (3.15) describe the dynamics of the interior flows. When the density of vapour (gas) is much smaller than the liquid, the outside can be assumed to be dynamically passive to simplify the problem. With this assumption, the kinematic

boundary condition is expressed as

$$\partial_t h + \boldsymbol{V}_i \cdot \nabla h = 0 \,, \tag{3.17}$$

where normal and tangential stresses are balanced, given by

$$p + \boldsymbol{n} \cdot (\boldsymbol{\tau} + \boldsymbol{S}) \cdot \boldsymbol{n} = \gamma \nabla \cdot \boldsymbol{n} \,, \tag{3.18}$$

$$\boldsymbol{n} \cdot (\boldsymbol{\tau} + \boldsymbol{S}) \cdot \boldsymbol{t} = 0 \,. \tag{3.19}$$

Here, h is represent the interface position, $\boldsymbol{V}_i$ is the velocity of interfaces, $\gamma \nabla \cdot \boldsymbol{n}$ is the Laplace pressure, $\boldsymbol{n}$ and $\boldsymbol{t}$ are normal and tangential vectors with respect to the interface, respectively.

The LLNS above is a complicated SPDE system, which is almost impossible to solve analytically. Although there exists some pioneering research [122, 123] concerning the numerical solutions for bulk fluids, nobody has yet developed a robust three-dimensional solver for the LLNS with the interface equations (Equation (3.14) $\sim$ (3.19)). It seems sufficiently difficult to construct a reliable numerical scheme for these equations directly that simplifying them mathematically would be desirable. In the next two sections, we will apply the lubrication (long-wave) approximation to derive two one-dimensional SPDEs from the equations above for specific flows at the nanoscale.

3.2.2 Stochastic Lubrication Equations for nanojets

In this section, we start from the derivation of the macroscopic/deterministic model, LE for jet flows first proposed by Eggers & Dupont [28] with the lubrication approximation used on the axisymmetric NS equations (Equation (A.1) $\sim$ (A.8b) in Appendix. A). Then a stochastic shear stress term is added to the LE to achieve the the stochastic lubrication equations (SLE), first derived by Moseler & Landman [1]. Although the thermal fluctuations in real physics are not axisymmetric, breakup profiles predicted by MD [1] and experiments [67] are approximately axisymmetric, indicating 'axisymmetric influence' of the thermal noise on nanothread dynamics. Therefore, it is reasonable to employ the axisymmetric assumption to derive the SLE.

A schematic of the system is shown in Figure 3.7. Note that the interface profiles h only depend on z spatially when the perturbations are assumed axisymmetric. Additionally, r_0 denotes the initial radius and λ represents the wavelength of the perturbations. These variables will be widely used in the next chapter to describe the instability.
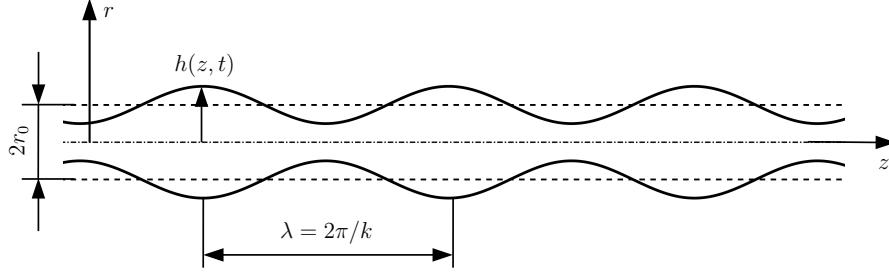
Figure 3.7: Schematic of a liquid thread with a perturbed interface

Since we are looking at thin columns of fluid relative to their elongation, Taylor expansion is applied to the axis velocity $u(z,t)$ and pressure $p(z,t)$ terms.

$$u(z,r) = u_0 + u_2 r^2 + O(r^4),$$ (3.20)

$$p(z,r) = p_0 + p_2 r^2 + O(r^4).$$ (3.21)

Substituting (3.20) and $v \ll u$ into the axisymmetric continuity equation (Equation (A.1)) yields,

$$v(z,r) \approx -\frac{r}{2}\frac{\partial u}{\partial z} = -\frac{r}{2}u_0' - \frac{r^3}{4}u_2',$$ (3.22)

where " $'$ " represents spatial derivative ∂_z. After substituting Equation (3.20)-(3.22) into the momentum equations (Equation (A.4) and (A.5)), and neglecting high order terms, we have

$$\partial_t u_0 + u_0 u_0' = -p_0'/\rho + \nu(4u_2 + u_0''),$$ (3.23)

$$0 = -\frac{u_0'}{2r} - \frac{1}{r^2}\left(-\frac{u_0' r}{2}\right).$$ (3.24)

Here, Equation (3.24) is identically satisfied. With the same approach, the interface equations (Equation (A.6)-(A.8b)) can be rewritten as

$$\partial_t h + u_0 h' + u_0' h/2 = 0,$$ (3.25)

$$p_0 + \mu u_0' = \gamma \left(\frac{1}{R_1} + \frac{1}{R_2}\right),$$ (3.26)

$$-u_0' h' + 2u_2 h - \frac{1}{2}u_0'' h - 2u_0'' h' = 0,$$ (3.27)

where R_1 is the radius of the cylinder at the different locations, and R_2 is the radius of perturbation waves along the z-axis. Substituting Equation (3.26) and (3.27) into

Equation (3.23) to eliminate u_2 and p_0 gives us a new momentum equation:

$$\partial_t u_0 + u_0 u_0' = -\frac{\gamma}{\rho}\left(\frac{1}{R_1} + \frac{1}{R_2}\right)' + \frac{3\nu}{h^2}\left(h^2 u_0'\right)'. \tag{3.28}$$

To take thermal fluctuations into account, we add stochastic stress, S_{LE}, modelled by a Gaussian (white) noise into the momentum equation above:

$$\partial_t u + uu' = -p'/\rho + 3\nu \left(h^2 u'\right)'/h^2 + S_{\mathrm{LE}}. \tag{3.29}$$

From Equation (3.28), we know the deterministic 'lubrication' shear stress,

$$\tau_{\mathrm{LE}} = 3\mu u',$$

where the coefficient '3' comes from the long-wave approximation. Combining the coefficient with fluctuation-dissipation theorem [124] in cylindrical coordinate yields the covariance of S_{LE},

$$
\begin{aligned}
&\langle S_{\mathrm{LE}}(z,t) S_{\mathrm{LE}}\left(\acute{z},\acute{t}\right)\rangle \\
&= \frac{3}{(2\pi h)^2}\int_0^{2\pi}\int_0^{2\pi}\int_0^h\int_0^h \langle S_{zz}(\mathbf{r},t) S_{zz}(\acute{\mathbf{r}},\acute{t})\rangle d\theta d\acute{\theta} dr d\acute{r}, \\
&= \frac{12 k_{\mathrm{B}} T \mu}{(2\pi h)^2}\int_0^{2\pi}\int_0^{2\pi}\int_0^h\int_0^h \frac{1}{h}\delta(\theta-\acute{\theta})\delta(r-\acute{r})\delta(z-\acute{z})\delta(t-\acute{t}) d\theta d\acute{\theta} dr d\acute{r}, \\
&= \frac{12 k_{\mathrm{B}} T \mu}{(2\pi h)^2} 2\pi \delta(z-\acute{z})\delta(t-\acute{t}), \\
&= \frac{6 k_{\mathrm{B}} T \mu}{\pi h^2}\delta(z-\acute{z})\delta(t-\acute{t}). \tag{3.30}
\end{aligned}
$$

Since S_{LE} represents random variables with Gaussian distribution, the square root of the covariance above is applied to describe the fluctuation intensity. Therefore, we can obtain the SLE:

$$\partial_t u = -uu' - p'/\rho + 3\nu\frac{(h^2 u')'}{h^2} + \frac{1}{\rho}\sqrt{\frac{6 k_{\mathrm{B}} T \mu}{\pi}}\frac{(h\mathcal{N})'}{h^2}, \tag{3.31}$$

$$\partial_t h = -uh' - u'h/2, \tag{3.32}$$

with the full Laplace pressure retained

$$p = \gamma \left[\frac{1}{h\sqrt{1 + (h')^2}} - \frac{h''}{\left(1 + (h')^2\right)^{\frac{3}{2}}} \right] , \qquad (3.33)$$

where $\mathcal{N}$ represents the white noise with the units $[\mathrm{m}^{-1/2}\,\mathrm{s}^{-1/2}]$. Two curvatures $(1/R_1$ and $1/R_2)$ in the Laplace pressure are expressed by h and its derivatives.

The SLE has been shown to be a powerful tool for predicting the interfacial dynamics of a nano-jet/thread with the fluctuation effect taken into consideration [1, 2, 125]. We will use it as one of the core equations in this thesis to explore the instability (Chapter 4) and rupture (Chapter 5) of nano threads.

Dealing with the derivative of $\mathcal{N}$ is the key to solving the SLE. Although values of differentiated white noise are infinite, its spectrum is not. Therefore, we can transfer the SLE into the frequency domain to achieve analytical solutions of $\mathcal{N}'$ (details will be shown in Chapter 4). For the numerical solutions, the evaluation of the derivative of white noise requires a minimum scale to be chosen (implied by the time step or grid size), which may cause problems in numerical stability or convergence (see Chapter 5 for more information).

3.2.3 Stochastic thin-film equation

Another interesting topic of study is the modelling of flows of bounded films at the nanoscale. Here, we will only focus on two dimensional systems, whose schematic is illustrated in Figure 3.8, where the shaded section represents the (solid) substrate and h_0 is the initial height of the film.
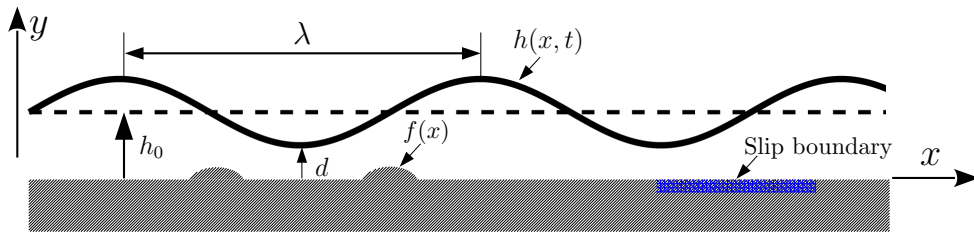
Figure 3.8: Schematic of a thin-film with different solid boundaries

This system can be modelled by two dimensional LLNS equations (Equation (A.9)-(A.14) in Appendix. A). We apply the methodology, first proposed by Grün et al [78] in 2006, to simplify these SPDEs further, where the lubrication (long-wave) approximation

29

is used again with the rescaling shown below:

$$x = \lambda\tilde{x}, \quad u = U\tilde{u}, \quad t = \frac{\lambda}{U}\tilde{t}, \quad p = \frac{U\mu}{\varepsilon d}\tilde{p}, \quad\quad S_{xy} = \frac{U\mu}{d}\tilde{S}_{xy},$$

$$y = d\tilde{y}, \quad v = \varepsilon U\tilde{v}, \quad \gamma = \frac{U\mu}{\varepsilon^3}\tilde{\gamma}, \quad \Pi = \frac{U\mu}{\varepsilon d}\tilde{\Pi}, \quad (S_{xx}, S_{yy}) = \frac{U\mu}{\lambda}(\tilde{S}_{xx}, \tilde{S}_{yy}).$$

Here, the small parameter $\varepsilon = d/\lambda \ll 1$ represents the ratio of the characteristic film height d and length scale λ. Note that the stochastic shear stress scales like the dominant term (lowest order in ε) in the corresponding components of the stress tensor. Here $\mu\partial_x u$ and $\mu\partial_y v$ is used to pursue the scales of S_{xx} and S_{yy}, respectively. The scale of S_{xy}, which is equal to S_{yx} due to symmetry, is evaluated by $\mu\partial_y u$ since another component ($\mu\partial_x v$) in τ_{xy} has a lower order, so it is neglected. Substituting all these scalings into Equation (A.9)-(A.11) yields,

$$\frac{\partial\tilde{u}}{\partial\tilde{x}} + \frac{\partial\tilde{v}}{\partial\tilde{y}} = 0\,, \tag{3.34}$$

$$\varepsilon\,\mathrm{Re}\,\frac{\mathrm{D}\tilde{u}}{\mathrm{D}\tilde{t}} = -\frac{\partial(\tilde{p} + \tilde{\Pi})}{\partial\tilde{x}} + \varepsilon^2\frac{\partial^2\tilde{u}}{\partial\tilde{x}^2} + \frac{\partial^2\tilde{u}}{\partial\tilde{y}^2} + \varepsilon^2\frac{\partial\tilde{S}_{xx}}{\partial\tilde{x}} + \frac{\partial\tilde{S}_{xy}}{\partial\tilde{y}}\,, \tag{3.35}$$

$$\varepsilon^3\,\mathrm{Re}\,\frac{\mathrm{D}\tilde{v}}{\mathrm{D}\tilde{t}} = -\frac{\partial(\tilde{p} + \tilde{\Pi})}{\partial\tilde{y}} + \varepsilon^4\frac{\partial^2\tilde{v}}{\partial\tilde{x}^2} + \varepsilon^2\frac{\partial^2\tilde{v}}{\partial\tilde{y}^2} + \varepsilon^2\frac{\partial\tilde{S}_{xy}}{\partial\tilde{x}} + \varepsilon^2\frac{\partial\tilde{S}_{yy}}{\partial\tilde{y}}\,, \tag{3.36}$$

where Reynolds number, $\mathrm{Re} = \rho U d/\mu$. Moreover, the interface equations ($y = h$) are modified as

$$\frac{\partial\tilde{h}}{\partial\tilde{t}} + \tilde{u}\frac{\partial\tilde{h}}{\partial\tilde{x}} - \tilde{v} = 0\,, \tag{3.37}$$

$$\tilde{p} + \frac{\varepsilon^4(\partial_{\tilde{x}}\tilde{h})^2(2\partial_{\tilde{x}}\tilde{u} + \tilde{S}_{xx}) - \varepsilon^2\,\partial_{\tilde{x}}\tilde{h}(\partial_{\tilde{y}}\tilde{u} + \varepsilon\partial_{\tilde{x}}\tilde{v} + 2\,\tilde{S}_{xy}) + \varepsilon^2(\partial_{\tilde{y}}\tilde{v} + \tilde{S}_{yy})}{1 + \varepsilon^2(\partial_{\tilde{x}}\tilde{h})^2}$$

$$= -\tilde{\gamma}\frac{\partial_{\tilde{x}}^2\tilde{h}}{[1 + \varepsilon^2(\partial_{\tilde{x}}\tilde{h})^2]^{3/2}}\,, \tag{3.38}$$

$$\varepsilon^2\partial_{\tilde{x}}\tilde{h}\left(2\,\partial_{\tilde{x}}\tilde{u} + \tilde{S}_{xx} - 2\,\partial_{\tilde{y}}\tilde{v} - \tilde{S}_{yy}\right) + \left[\varepsilon^2(\partial_{\tilde{x}}\tilde{h})^2 - 1\right](\partial_{\tilde{y}}\tilde{u} + \varepsilon^2\partial_{\tilde{x}}\tilde{v} + \tilde{S}_{xy}) = 0\,. \tag{3.39}$$

After eliminating all the high order terms, we obtain

$$\partial_{\tilde{x}}\tilde{u} + \partial_{\tilde{y}}\tilde{v} = 0\,, \tag{3.40a}$$

$$0 = -\partial_{\tilde{x}}(\tilde{p} + \tilde{\Pi}) + \partial_{\tilde{y}}^2\tilde{u} + \partial_{\tilde{y}}\tilde{S}_{xy}\,, \tag{3.40b}$$

$$0 = -\partial_{\tilde{y}}(\tilde{p} + \tilde{\Pi})\,, \tag{3.40c}$$

$$\partial_{\tilde{t}}\tilde{h} + \tilde{u}\,\partial_{\tilde{x}}\tilde{h} - \tilde{v} = 0 \,, \tag{3.40d}$$

$$\tilde{p} = -\tilde{\gamma}\partial_{\tilde{x}}^2\tilde{h}, \quad (y = h)\,, \tag{3.40e}$$

$$\partial_{\tilde{y}}\tilde{u} + \tilde{S}_{xy} = 0, \quad (y = h)\,. \tag{3.40f}$$

In Grün's work [78] the substrate boundary condition was set as perfectly smooth and no-slip (Equation (3.41)) in their further steps, which, in reality, is not usually the case, especially at the nanoscale:

$$\tilde{u} = 0 \quad \text{at} \quad \tilde{y} = 0\,. \tag{3.41}$$

In the following parts of this section, we will take two important substrate effects, namely the surface roughness and slip shown in Figure 3.8, into consideration and re-derive the stochastic thin-film equation (STFE) with these factors.

Derivation of the STFE with surface roughness – Since Equation (3.40c) shows that the pressure term, $\tilde{p} + \tilde{\Pi}$ is independent of y, we can easily integrate Equation (3.40b) with respect to the y coordinate from $\tilde{h}$ to $\tilde{y}$ with Equation (3.40f) as the boundary condition:

$$(\tilde{y} - \tilde{h})\partial_{\tilde{x}}(\tilde{p} + \tilde{\Pi}) = \partial_{\tilde{y}}\tilde{u} + \tilde{S}\,. \tag{3.42}$$

Then, Equation (3.42) is integrated with respect to the y coordinate from the substrate to $\tilde{y}$. Note that, here, the substrate boundary condition is

$$\tilde{u} = 0 \quad \text{at} \quad \tilde{y} = f(x)\,. \tag{3.43}$$

Here, $f(x)$ is the function used to describe the substrate profiles (see the 'bump' in the Figure 3.8). The integration gives

$$\tilde{u} = (\tilde{y}^2/2 - \tilde{h}\tilde{y} - \tilde{f}^2/2 + \tilde{f}\tilde{h})\partial_{\tilde{x}}(\tilde{p} + \tilde{\Pi}) - (\tilde{h} - \tilde{y})\tilde{S}\,. \tag{3.44}$$

Integrating Equation (3.40a) across the channel gives

$$\partial_{\tilde{x}}\left(\int_{\tilde{f}}^{\tilde{h}} \tilde{u}\,d\tilde{y}\right) - \tilde{u}\partial_{\tilde{x}}\tilde{h} + \tilde{v} = 0\,. \tag{3.45}$$

Combined with Equation (3.40d), we have

$$\partial_{\tilde{t}}\tilde{h} = -\partial_{\tilde{x}}\left(\int_{\tilde{f}}^{\tilde{h}} \tilde{u}\,d\tilde{y}\right)\,. \tag{3.46}$$

Therefore,

$$\partial_{\tilde{t}}\tilde{h} = -\partial_{\tilde{x}}\left\{\int_{\tilde{f}}^{\tilde{h}}\left[(\tilde{y}^2/2 - \tilde{h}\tilde{y} - \tilde{f}^2/2 + \tilde{f}\tilde{h})\partial_{\tilde{x}}(\tilde{p} + \tilde{\Pi}) - (\tilde{h} - \tilde{y})\tilde{S}\right]d\tilde{y}\right\}. \qquad (3.47)$$

After substituting Equation (3.40e) and rewriting $\tilde{\Pi}$ in terms of the interface potential $\tilde{\Phi}$, we obtain

$$\partial_{\tilde{t}}\tilde{h} = \partial_{\tilde{x}}\left[\frac{(\tilde{h} - \tilde{f})^3}{3}\partial_{\tilde{x}}\left(\tilde{\Phi} - \tilde{\gamma}\,\partial_{\tilde{x}}^2\tilde{h}\right) + \int_{\tilde{f}}^{\tilde{h}}(\tilde{h} - \tilde{y})\tilde{S}d\tilde{y}\right]. \qquad (3.48)$$

To obtain the explicit expression for the noise term, we return to the dimensional domain where Equation (3.48) can be written as

$$\partial_t h = \partial_x\left[\frac{(h - f)^3}{3\mu}\partial_x\left(\Phi - \gamma\,\partial_x^2 h\right) + \frac{1}{\mu}\int_f^h(h - y)Sdy\right]. \qquad (3.49)$$

Due to the delta-correlations in the fluctuating shear stress (Equation (3.16)), we can calculate the variance of $\int_f^h(h - y)S(x, y, t)dy$:

$$\left\langle\int_f^h(h - y)S(x, y, t)dy\int_f^h(h - \acute{y})S(\acute{x}, \acute{y}, \acute{t})d\acute{y}\right\rangle$$
$$= \int_f^h\int_f^h(h - y)(h - \acute{y})\left\langle S(x, y, t)S(\acute{x}, \acute{y}, \acute{t})\right\rangle d\acute{y}dy$$
$$= \int_f^h\int_f^h(h - y)(h - \acute{y})\left[\frac{2k_{\mathrm{B}}T\mu}{W}\delta(x - \acute{x})\delta(y - \acute{y})\delta(t - \acute{t})\right]d\acute{y}dy$$
$$= \left[\frac{2k_{\mathrm{B}}T\mu}{W}\delta(x - \acute{x})\delta(t - \acute{t})\right]\int_f^h(h - y)^2dy$$
$$= \frac{2k_{\mathrm{B}}T\mu}{3W}(h - f)^3\delta(x - \acute{x})\delta(t - \acute{t}), \qquad (3.50)$$

where W represent the width along the z-direction. Finally, we obtain the lubrication equation for arbitrary surfaces

$$\partial_t h = \partial_x\left[\frac{(h - f)^3}{3\mu}\partial_x\left(\Phi - \gamma\,\partial_x^2 h\right) + \sqrt{\frac{2k_{\mathrm{B}}T}{3W\mu}}(h - f)^{3/2}\mathcal{N}(x, t)\right]. \qquad (3.51)$$

Here, $\mathcal{N}$ has the same meaning as is defined in §3.2.2. Note that when $f = 0$, that is when the boundary condition (Equation (3.43)) is equal to Equation (3.41), the STFE

above will return to Grün's result [78]:

$$\partial_t h = \partial_x \left[\frac{h^3}{3\mu} \partial_x \left(\Phi - \gamma \partial_x^2 h \right) + \sqrt{\frac{2k_B T h^3}{3W\mu}} \mathcal{N}(x,t) \right].$$ (3.52)

Derivation of the STFE with a slip boundary condition– In a similar way, we can derive a model with the 'Navier slip boundary condition',

$$\tilde{u}_s = \tilde{\beta} \partial_{\tilde{y}} \tilde{u} \quad \text{at} \quad \tilde{y} = 0.$$ (3.53)

Here, $\tilde{u}_s$ is the dimensionless slip velocity and $\tilde{\beta}$ represents the dimensionless slip length. With this boundary condition, the integration of Equation (3.42) will be

$$\tilde{u} - \tilde{u}_s = (\tilde{y}^2/2 - \tilde{h}\tilde{y})\partial_{\tilde{x}}(\tilde{p} + \tilde{\Pi}) - (\tilde{h} - \tilde{y})\tilde{S}.$$ (3.54)

Here, the explicit expression of $\tilde{u}_s$ can be obtained from the combination of Equation (3.42) and the slip boundary

$$\tilde{u}_s = -\tilde{\beta}\tilde{h}\partial_{\tilde{x}}(\tilde{p} + \tilde{\Pi}) - \tilde{\beta}\tilde{S}_s.$$ (3.55)

$\tilde{S}_s$ represents the stochastic shear stress on the liquid-solid interface. Substituting Equation (3.55) and (3.54) into Equation (3.46), we have

$$\partial_{\tilde{t}}\tilde{h} = \partial_{\tilde{x}} \left\{ \left(\tilde{h}^3/3 + \tilde{\beta}\tilde{h}^2 \right) \partial_{\tilde{x}}(\tilde{p} + \tilde{\Pi}) + \int_0^{\tilde{h}} \left[(\tilde{h} - \tilde{y})\tilde{S} + \tilde{\beta}\,\tilde{S}_s \right] d\tilde{y} \right\}.$$ (3.56)

Returning to the dimensional domain, we get the lubrication framework with the slip length:

$$\partial_t h = \partial_x \left\{ \frac{h^3/3 + \beta h^2}{\mu} \partial_x(p + \Pi) + \frac{1}{\mu} \int_0^h \left[(h - y)S + \beta S_s \right] dy \right\}.$$ (3.57)

In a similar way, we can calculate variance of $\int_f^h \left[(h - y)S + \beta S_s \right] dy$. Note that the shear stress in the liquid bulk and wall boundary are uncorrelated, so the variance between these two types of stress is zero, i.e., $\langle S S_s \rangle = 0$. Therefore, the total variance above

only contains two covariance terms, namely,

$$\left\langle \int_0^h \left[(h-y)S(x,y,t) + \beta\, S_{\mathrm{s}}(x,t)\right] dy \int_0^h \left[(h-\acute{y})S(\acute{x},\acute{y},\acute{t}) + \beta\, S_{\mathrm{s}}(\acute{x},\acute{t})\right] d\acute{y} \right\rangle$$

$$= \int_0^h \int_0^h \left[(h-y)(h-\acute{y})\left\langle S(x,y,t)\, S(\acute{x},\acute{y},\acute{t})\right\rangle + \beta^2 \left\langle S_{\mathrm{s}}(x,t)\, S_{\mathrm{s}}(\acute{x},\acute{t})\right\rangle\right] d\acute{y}dy$$

$$= \left[\frac{2k_{\mathrm{B}}T\mu}{W}\delta(x-\acute{x})\delta(t-\acute{t})\right] \int_0^h \left[(h-y)^2 + \beta\, h\right] dy$$

$$= \left[\frac{2k_{\mathrm{B}}T\mu}{W}\delta(x-\acute{x})\delta(t-\acute{t})\right] \left(\frac{h^3}{3} + \beta h^2\right). \tag{3.58}$$

Here, the covariance $\langle S_{\mathrm{s}}(x,t)S_{\mathrm{s}}(\acute{x},\acute{t})\rangle$ is derived from the model proposed by Bocquet & Barrat [126] (See Appendix. B for more details) Finally, we obtain the STFE with the slip length:

$$\partial_t h = \partial_x \left[\frac{h^3/3 + \beta h^2}{\mu}\partial_x\left(\Phi - \gamma\,\partial_x^2 h\right) + \sqrt{\frac{2k_{\mathrm{B}}T}{W\mu}\left(\frac{h^3}{3} + \beta h^2\right)}\,\mathcal{N}(x,t)\right]. \tag{3.59}$$

Analogously (compared to the conclusion with roughness), when $\beta = 0$, Grün's result is recovered from the STFE above.

3.3 Summary

In this chapter, we present the two models employed in this thesis for studying the thermal fluctuations of nanoscale interfacial flows. The basic framework of MD is introduced in § 3.1.1 with three molecular models (structures) described in § 3.1.2. LAMMPS is used to establish these molecular structures in § 3.1.3, whose results are validated by experimental data.

In Section 3.2, we introduced three different kinds of SPDE models for fluctuating hydrodynamics. The three-dimensional LLNS is first presented in § 3.2.1, which provides the basic SPDE framework. Then two simplified one-dimensional lubrication (long-wave) equations are derived for two specific flows. One is the SLE for nano-jet flows, first proposed by Moseler & Landman in 2000 [1]. In § 3.2.2, we use a simple direct approach (modified based on [28]) to derive the SLE. The second is the STFE, used to describe bounded thin-film flows. Two new STFEs are proposed in § 3.2.3 with rough surface and slip boundary effects taken into account. Note that both return to the well-known Grün result [78] without roughness ($f = 0$) or slip ($\beta = 0$).

The SLE and STFE will be used as the core SPDE models in the following chap-

ters to explore the interfacial dynamics in the presence of fluctuation effects. Because of their simplicity, analytical solutions of their linearised versions are accessible. One solution will be explored in the next chapter to study the instability of nanoscale liquid cylinders.

Chapter 4

Rayleigh-Plateau instability at the nanoscale

In this chapter, we revisit the Rayleigh-Plateau (RP) instability at the nanoscale, using both the SLE and MD. First, in Section 4.1, macroscopic RP theories are introduced to explain their two classical contributions:

(i) critical wavenumber, k_{crit};

(ii) dominant perturbation modes, k_{max}.

In Section 4.2 an analytical framework, SLE-RP (derived from the SLE) is proposed to model the influence of thermal fluctuations on the instability (both k_{crit} and k_{max}) at the nanoscale, which is supported by MD in Section 4.3.

4.1 Macroscopic RP Instability

The RP instability is analysed on an infinitely long cylinder with some initial perturbations (see Figure 4.1). According to the Young-Laplace equation (Equation (4.1)), the stability of these perturbations depends on the capillary forces of two radii of curvature, where R_1 is the radius of the cylinder at the different locations, and R_2 is the radius of perturbation waves along the z-axis:

$$\triangle p = \gamma \left(1/R_1 + 1/R_2 \right) . \tag{4.1}$$
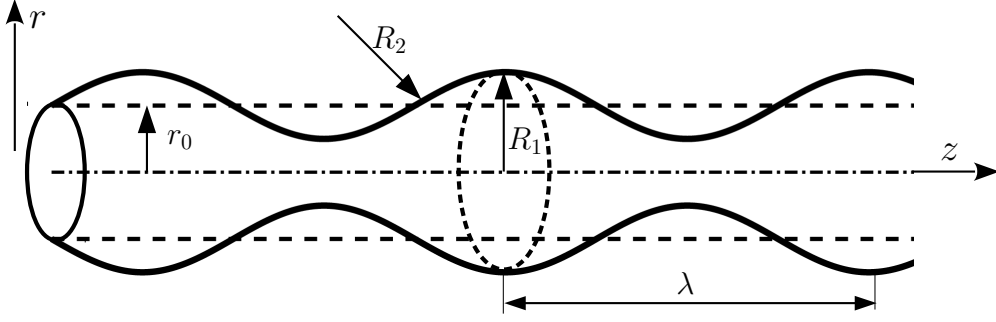
Figure 4.1: Schematic for the RP Instability

Since the curvature varies at different locations, the capillary force of the curvature, $1/R_1$ is larger at troughs than at crests, resulting in the driving force for the growth of the perturbations. However, the capillary force of $1/R_2$ is negative at troughs, creating an opposite contribution. Therefore, the instability value depends on which of the two components play a dominant role. Qualitatively, longer perturbation waves are 'more unstable' because of weaker negative forces ($1/R_2$ has a smaller value). However, to achieve quantitative results, we need to return to the Navier-Stokes (NS) equation, as covered in the next subsection.

4.1.1 RP theories based on the axisymmetric NS equations

To simplify the problem and connect to Rayleigh's original analysis, we start by assuming an inviscid fluid. The interface disturbance can be expressed as $h = r_0 + \varepsilon r_0 e^{\omega t + ikz}$, where $\varepsilon \ll 1$, and other variables are modelled by adding a perturbed variable ($\hat{u}$, $\hat{v}$, $\hat{p}$) to an initial value (u_0, v_0, p_0),

$$u = u_0 + \hat{u}, \quad v = v_0 + \hat{v}, \quad p = p_0 + \hat{p}.$$

Since $u_0 = 0$ and $v_0 = 0$, we can linearize the axisymmetric NS equation (Equation (A.1)-(A.3)) by approximating to zero all terms containing more than one perturbed variable (i.e. $\hat{u}\partial_z\hat{u}$), giving us

$$\frac{\partial \hat{u}}{\partial z} + \frac{\partial \hat{v}}{\partial r} + \frac{\hat{v}}{r} = 0 \,, \tag{4.2}$$

$$\frac{\partial \hat{u}}{\partial t} = -\frac{1}{\rho}\frac{\partial \hat{p}}{\partial z} \,, \tag{4.3}$$

$$\frac{\partial \hat{v}}{\partial t} = -\frac{1}{\rho}\frac{\partial \hat{p}}{\partial r} \,. \tag{4.4}$$

We assume that the disturbances in velocity and pressure will have the same form as the interface disturbance, so we can write the perturbation velocities and pressure as:

$$\hat{u} = Z(r)e^{\omega t + ikz}, \quad \hat{v} = R(r)e^{\omega t + ikz}, \quad \hat{p} = P(r)e^{\omega t + ikz}.$$

Substituting these into Equations (4.2)-(4.4) yields perturbation linear equations:

$$\frac{d\text{R}}{dr} + \frac{\text{R}}{r} + ikz = 0 \,, \tag{4.5}$$

$$\omega Z = -\frac{ik}{\rho} P \,, \tag{4.6}$$

$$\omega R = -\frac{1}{\rho}\frac{d\text{P}}{dr} \,. \tag{4.7}$$

Eliminating the Z and P gives us a differential equation in R:

$$r^2 \frac{d^2 \text{R}}{dr^2} + r\frac{d\text{R}}{dr} - \left[1 + (kr)^2\right]\text{R} = 0 \,. \tag{4.8}$$

Since Equation (4.8) is a second-order differential equation, modified Bessel functions of order 1 can be employed to find its solution:

$$R(r) = CI_1(kr) \,. \tag{4.9}$$

To determine the value of C, we use the kinematic boundary condition (Equation (A.6)), with the perturbation growth rate equal to the perturbation velocity v:

$$\frac{\partial \hat{r}}{\partial t} = \hat{v} \Rightarrow \varepsilon r_0 \omega e^{\omega t + ikz} = R(r_0)e^{\omega t + ikz} \,,$$

$$\Rightarrow \varepsilon r_0 \omega = CI_1(kr_0) \,,$$

$$\Rightarrow C = \varepsilon r_0 \omega / I_1(kr_0) \,. \tag{4.10}$$

Substituting the entire perturbation formula into the equation for the normal pressure (Equation (A.7b)) gives

$$p_0 + \hat{p} = \gamma(1/R_1 + 1/R_2) \,,$$

$$\Rightarrow p_0 + \hat{p} = \gamma \left(\frac{1}{r_0(1 + \hat{r})} - \frac{\partial^2 \hat{r}}{\partial z^2} \right) \,,$$

$$\Rightarrow \gamma/r_0 + \hat{p} = \gamma \left(1/r_0 - \varepsilon e^{\omega t + ikz}/r_0 + \varepsilon k^2 r_0 e^{\omega t + ikz} \right) \,,$$

$$\Rightarrow \hat{p} = -\frac{\varepsilon \gamma}{r_0} \left(1 - k^2 r_0^2\right) e^{\omega t + ikz} \,. \tag{4.11}$$

Integrating Equation (4.7) yields another formula for $\hat{p}$

$$P(r) = -\frac{\varepsilon \omega^2 \rho r_0}{I_1(kr_0)} \int_0^{r_0} I_1(kr) dr \,,$$

$$\Rightarrow \hat{p} = -\frac{\varepsilon \omega^2 \rho r_0 I_0(kr_0)}{k I_1(kr_0)} e^{\omega t + ikz} \,. \tag{4.12}$$

In this way, we obtain the core equation of RP Instability [19, 20]:

$$\omega^2 = \frac{\gamma}{\rho r_0^3} k r_0 \frac{I_1(kr_0)}{I_0(kr_0)} \left(1 - k^2 r_0^2\right) \,, \tag{4.13}$$

Taking viscosity into consideration, Weber [21] obtained a more general equation for the growth rate ω:

$$\omega^2 + 2\nu k^2 \left\{ 2 - \frac{I_1(kr_0)}{kr_0 I_0(kr_0)} + \frac{2k^2}{l^2 - k^2} \left[1 - \frac{l}{k} \frac{I_1(kr_0)}{I_0(kr_0)} \frac{I_0(lr_0)}{I_1(lr_0)} \right] \right\} \omega$$
$$= \frac{\gamma}{\rho r_0^3} (1 - k^2 r_0^2) k r_0 \frac{I_1(kr_0)}{I_0(kr_0)} \,, \tag{4.14}$$

where $l^2 = k^2 + \omega / \mu$. When the long wave approximation is applied (for small arguments of kr_0), the Bessel function can be approximated by the leading terms of their expansions [127], namely, $I_1(kr_0)/I_0(kr_0) = kr_0/2$. So Equation (4.14) can be simplified to

$$\omega^2 + 3\nu k^2 \omega = \frac{\gamma}{2\rho r_0^3} (1 - k^2 r_0^2) k^2 r_0^2 \,. \tag{4.15}$$

Since the mathematical derivation for Equation (4.14) is rather complicated, the lubrication equation in Chapter 3 is applied instead to directly obtain Equation (4.15), as presented in the next section.

4.1.2 Stability analyses of the LE

By the same approach introduced in §4.1.1, we substitute the small perturbation term $\hat{r}$ into the LE in Chapter 3. After ignoring all terms of order $O(\hat{r})$ or higher, we have

$$\partial_t u = -p'/\rho + 3\nu u'' \,, \tag{4.16}$$

$$\partial_t \hat{r} = -u'/2 \,. \tag{4.17}$$

Replacing all the derivatives of u in Equation (4.16) with the derivatives of $\hat{r}$ yields

$$-2\frac{\partial^2 \hat{r}}{\partial t^2} + \frac{p''}{\rho} = -6\nu\frac{\partial \hat{r}''}{\partial t}\,.\tag{4.18}$$

In addition, the full Laplace pressure can be simplified as Equation (4.19) with only leading-order terms:

$$p = \gamma(1/h - h'')\,.\tag{4.19}$$

Therefore, the derivative of the pressure becomes

$$p'' = \gamma\left(-\frac{h''}{h^2} - h''''\right) = \gamma\left(-\frac{\hat{r}''}{r_0} - r_0\hat{r}''''\right)\,.\tag{4.20}$$

Adding Equation (4.20) to Equation (4.18), we obtain the following linearised LE (LLE)

$$\frac{\partial^2 \hat{r}}{\partial t^2} + \frac{\gamma}{2\rho}\left(\frac{\hat{r}''}{r_0} + r_0\hat{r}''''\right) - 3\nu\frac{\partial \hat{r}''}{\partial t} = 0\,.\tag{4.21}$$

Substituting $\hat{r} = r_0\varepsilon e^{\omega t + ikz}$ into Equation (4.21) gives us the same expression as Equation (4.15) in the previous section:

$$\omega^2 + (3\nu k^2)\omega + \frac{\gamma}{2\rho r_0^3}k^2 r_0^2\left(k^2 r_0^2 - 1\right) = 0\,.\tag{4.22}$$

4.1.3 Dispersion relation

Solving the equations above provides the dispersion relation between the growth rate, ω, and the wavenumber k. To model the influence of the liquid properties more easily, we nondimensionalise the growth rate with $\tilde{\omega} = \omega/\sqrt{\gamma/\left(\rho r_0^3\right)}$. So, for the inviscid flow, we can achieve Rayleigh's conclusion [19] from Equation (4.13) as

$$\tilde{\omega} = \sqrt{\frac{I_1(kr_0)}{I_0(kr_0)}kr_0\left(1 - k^2 r_0^2\right)}\,.\tag{4.23}$$

With long wave approximation, the lubrication result is

$$\tilde{\omega} = kr_0\sqrt{\left(1 - k^2 r_0^2\right)/2}\,.\tag{4.24}$$
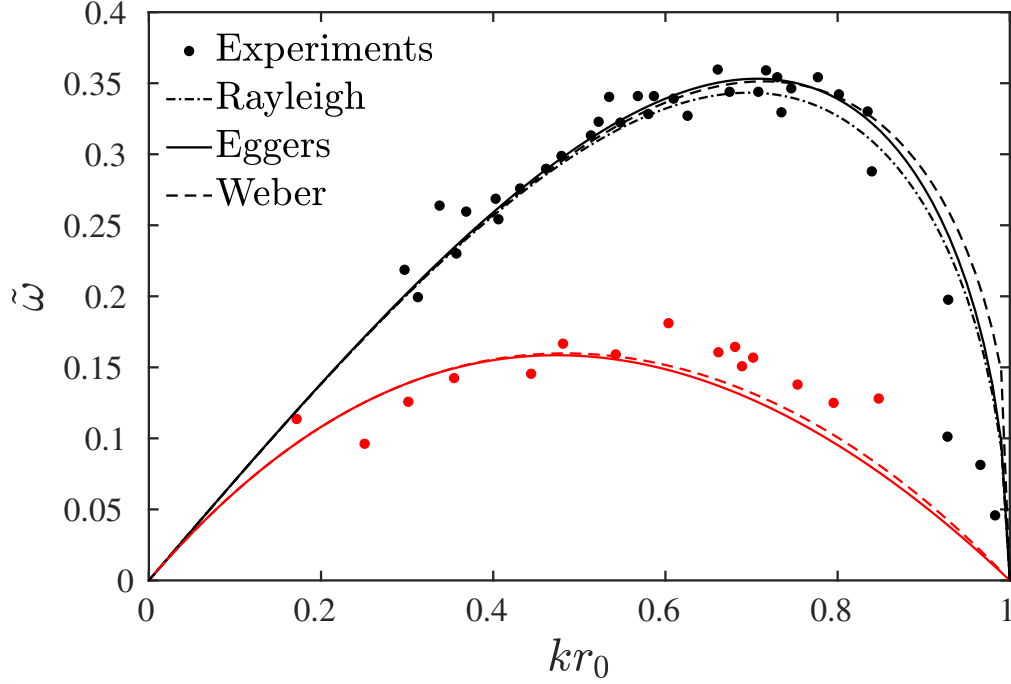
Figure 4.2: The dispersion relation for different liquids. Black lines represent liquid water with $\mathrm{Oh} = 10^{-3}$ and red ones represent glycerol with $\mathrm{Oh} = 0.58$. The dots are the experimental data from [24]. The dash-dotted lines and solid lines are the results of Equations (4.24) and (4.25) respectively. Dashed lines are the numerical solutions for Equation (4.14).

From Equation (4.22), we derive the lubrication result including the viscous term, which was first obtained by Eggers & Dupont [28]

$$\tilde{\omega} = \frac{kr_0}{2} \sqrt{\left(9\,\mathrm{Oh}^2 - 2\right) k^2 r_0^2 + 2} - \frac{3}{2}\,\mathrm{Oh}\,k^2 \,, \tag{4.25}$$

where $\mathrm{Oh} = \nu\sqrt{\rho/\left(\gamma r_0\right)}$ is the Ohnesorge number, which relates the viscous forces to inertial and surface-tension. Note that, when $\mathrm{Oh} = 0$, the inviscid result (Equation (4.24)) will be recovered from Eggers' model above.

The dispersion relations of the models above are compared in Figure 4.2 with experimental data in [24]. Since Weber's model (Equation (4.14)) is a complex nonlinear equation, we will solve it numerically with an iteration scheme. From Figure 4.2, we can see that:

(i) all the models can capture the physics of the instability well due to good agreements

41

with the experimental data;

(ii) deviations between Eggers' model and Weber's results are small, showing strong capabilities of the LE in spite of the lubrication (long-wave) approximation.

This finding also gives us further confidence to employ its expansion, SLE, to study the instability at the nanoscale, which is the main contribution of this chapter.

Moreover, two main conclusions of the RP theory are clearly shown in Figure 4.2. The first is that $\tilde{\omega} = 0$ at $kr_0 = 1$, showing that only long-wave perturbations are unstable ($kr_0 < 1$) and the critical wavelength $\lambda_{\text{crit}} = 2\pi/k = 2\pi r_0$. The second is the fastest growing (dominant) wavenumber (kr_0 for $\tilde{\omega}_{\text{max}}$). Note that this dominant mode depends on Oh: liquids with larger Oh are found to have smaller dominant wavenumbers, where Rayleigh's inviscid model is applicable. Since these two main conclusions are the core of the classical RP theory, one of the key purposes of this work is to answer whether they are still valid at the nanoscale. Details of our findings will be presented in the following sections.

4.2 SLE-RP framework

In this section, we propose an analytical framework, SLE-RP for the RP instability at the nanoscale, taking the influence of thermal fluctuations into account. First, stability analyses are applied to the SLE.

4.2.1 Stability analysis

We can obtain the linearised SLE with respect to perturbation variables $\hat{r}(z, t)$ in a similar way to the linearisation approach in Section 4.1.2, writing it as

$$\frac{\partial^2 \hat{r}}{\partial t^2} + \frac{\gamma}{2\rho} \left(\frac{\hat{r}''}{r_0} + r_0 \hat{r}'''' \right) - 3\nu \frac{\partial \hat{r}''}{\partial t} = -\frac{A}{2r_0} \mathcal{N}''. \tag{4.26}$$

Note that the only difference between Equations (4.21) and (4.26) is the stochastic term on the right-hand side. A finite Fourier transform is applied to Equation (4.26) to obtain

$$\frac{\mathrm{d}^2 R}{\mathrm{d}t^2} + \alpha \frac{\mathrm{d}R}{\mathrm{d}t} + \beta R = \frac{A}{2r_0} k^2 N \,, \tag{4.27}$$

where $\alpha = 3\mu k^2$ and $\beta = \frac{\gamma}{2\rho}\left(r_0 k^4 - \frac{k^2}{r_0}\right)$ and the transformed variables are defined as follows:

$$R(k,t) = \int_0^L \hat{r}(z,t)e^{-ikz}dz \quad \text{and} \quad N(k,t) = \int_0^L \mathcal{N}(z,t)e^{-ikz}dz.$$

The solution of Equation (4.27) is linearly decomposed into two parts:

$$R = R_{\mathrm{LE}} + R_{\mathrm{fluc}}. \tag{4.28}$$

The first part is the solution to the homogenous form of Equation (4.27) (i.e. with $A = 0$) with some stationary initial disturbance (i.e. $R=R_{\mathrm{i}}$ and $dR/dt=0$ at $t = 0$). The solution to the homogeneous ODE is straightforward to obtain:

$$R_{\mathrm{LE}} = R_{\mathrm{i}}e^{-at/2t_0}\left[\cosh\left(ct/2t_0\right) + \frac{a\sinh\left(ct/2t_0\right)}{c}\right], \tag{4.29}$$

where

$$a = 3(kr_0)^2\left(\frac{\ell_\nu}{r_0}\right)^{\frac{1}{2}} \quad \text{and} \quad c = 2\left[\frac{9}{4}\frac{\ell_\nu}{r_0}(kr_0)^4 + \frac{(kr_0)^2}{2}(1 - (kr_0)^2)\right]^{\frac{1}{2}},$$

and characteristic flow scales for time $t_0 = (\rho r_0^3/\gamma)^{\frac{1}{2}}$ and length $\ell_\nu = \rho\nu^2/\gamma$ have been introduced. This is a solution to the LE (there is no fluctuating component), and is thus denoted R_{LE} in Equation (4.28).

The second component of the solution arises from solving the full form of Equation (4.27) with zero initial disturbance; this part of the solution is solely due to fluctuations, and is thus denoted R_{fluc}. This is obtained by determining the impulse response of the homogeneous equation,

$$H(k,t) = 2t_0 e^{-at/2t_0}\sinh(ct/2t_0)/c. \tag{4.30}$$

which due to the linear, time-invariant nature of the system, allows us to write

$$R_{\mathrm{fluc}} = \frac{Ak^2}{2r_0}\int_0^t N(k,t-\mathcal{T})H(k,\mathcal{T})d\mathcal{T}. \tag{4.31}$$

The modal amplitude R ($= R_{\mathrm{LE}} + R_{\mathrm{fluc}}$) is a complex random variable, with zero mean. We note that R_{LE} is also random, as it develops from a random initial condition, but is uncorrelated with R_{fluc} (both have zero mean). So, in order to obtain information

on how disturbances associated with each wavenumber develop in time, allowing the identification of unstable and fastest growing modes, the root mean square (rms) of $|R|$ is sought (equivalent to the standard deviation of $|R|$).

$$|R|_{\text{rms}} = \sqrt{\overline{|R_{\text{LE}} + R_{\text{fluc}}|^2}} = \sqrt{\overline{|R_{\text{LE}}|^2} + \overline{|R_{\text{fluc}}|^2}}, \tag{4.32}$$

where $|R_{\text{LE}}|^2$ can easily be obtained from Equation (4.29).

$$\overline{|R_{\text{LE}}|^2} = \overline{|R_i|^2} e^{-at/t_0} \left[\cosh\left(ct/2t_0\right) + \frac{a \sinh\left(ct/2t_0\right)}{c} \right]^2. \tag{4.33}$$

Since $N(k,t)$ is uncorrelated Gaussian white noise, the variance of N is

$$\begin{aligned}
\overline{|N(k,t)|^2} &= \delta(t)\overline{|N(k)|^2} \\
&= \delta(t)\left\langle N(k)N(-k) \right\rangle \\
&= \delta(t)\left\langle \int_0^L \int_0^L \mathcal{N}(z)e^{-ikz}\mathcal{N}(z')e^{ikz'} dzdz' \right\rangle, \\
&= \delta(t)\left\langle \int_0^L \int_0^L \mathcal{N}(z)\mathcal{N}(z')e^{ik(z'-z)} dzdz' \right\rangle, \\
&= \delta(t)\left\langle \int_0^L \int_0^L \delta(z-z')e^{ik(z'-z)} dzdz' \right\rangle, \\
&= \delta(t)L. \tag{4.34}
\end{aligned}$$

Substituting Equation (4.34) into Equation (4.31) gives us

$$\begin{aligned}
\overline{|R_{\text{fluc}}|^2} &= \left(\frac{Ak^2}{2r_0}\right)^2 \overline{\left|\int_0^t N(k,t-\mathcal{T})H(k,\mathcal{T})d\mathcal{T}\right|^2}, \\
&= \left(\frac{Ak^2}{2r_0}\right)^2 L \int_0^t H^2 d\mathcal{T}, \\
&= \ell_{\text{fluc}}^2 b \frac{(a^2-c^2) - a^2\cosh(ct/t_0) - ac\sinh(ct/t_0) + c^2 e^{at/t_0}}{ac^2(a^2-c^2)e^{at/t_0}}, \tag{4.35}
\end{aligned}$$

where non-dimensional $b = \frac{3}{\pi}\frac{L}{r_0}(kr_0)^4 \left(\frac{\ell_\nu}{r_0}\right)^{\frac{1}{2}}$ and the thermal capillary length $\ell_{\text{fluc}} = (k_{\text{B}}T/\gamma)^{\frac{1}{2}}$ gives the characteristic length scale of the fluctuations. More details of the derivations of Equation (4.35) are presented in Appendix C.

Finally, we get the expression for the rms of the modal amplitude:

$$|R|_{\mathrm{rms}} = \sqrt{\overline{|R_{\mathrm{LE}}|^2} + \overline{|R_{\mathrm{fluc}}|^2}}\,, \tag{4.36}$$

$$\overline{|R_{\mathrm{LE}}|^2} = |R_{\mathrm{i}}|^2 e^{-at/t_0} \left[\cosh\left(ct/2t_0\right) + \frac{a\sinh(ct/2t_0)}{c}\right]^2,$$

$$\overline{|R_{\mathrm{fluc}}|^2} = \ell_{\mathrm{fluc}}^2\, b\, \frac{(a^2-c^2)-a^2\cosh(ct/t_0)-ac\sinh(ct/t_0)+c^2 e^{at/t_0}}{ac^2(a^2-c^2)e^{at/t_0}}\,,$$

which is the main result of our SLE-RP framework. This modal amplitude, which is a function of k and t, gives information on how disturbances associated with each wavenumber develop from (growing) unstable modes, as well as allowing the fastest growing (most dangerous) mode to be identified.

4.2.2 Convergence to the classical model

From Equation (4.36), fluctuations can be seen to be negligible when the thermal capillary length is much shorter than the initial modal amplitude; i.e $R \to R_{\mathrm{LE}}$ as $\ell_{\mathrm{fluc}}/R_{\mathrm{i}} \to 0$. We refer to this classical limit as the LE-RP model (as distinct from the SLE-RP model). Additionally, as $t \to \infty$,

$$|R_{\mathrm{LE}}|^2 \to |R_i|^2 e^{(c-a)t/t_0} \left(\frac{c+a}{2c}\right)^2,$$

$$\overline{|R_{\mathrm{fluc}}|^2} \to \frac{\ell_{\mathrm{fluc}}^2\, b}{2ac^2(a^2-c^2)} \left[2c^2 - e^{(c-a)t/t_0}\left(a^2+ac\right)\right],$$

with $c - a \geq 0$ for $kr_0 \leq 1$, which is the case as $t \to \infty$. Therefore, a functional form of Equation (4.36) is:

$$\mathcal{R}(k,t) = \mathcal{F}_1(k)e^{\mathcal{G}(k)t} + \mathcal{F}_2(k)\,, \tag{4.37}$$

where

$$
\begin{cases}
\mathcal{G}(k) &= (c-a)/t_0\,, \\
\mathcal{F}_1(k) &= |R_i|^2 \left(\frac{c+a}{2c}\right)^2 + \frac{\ell_{\mathrm{fluc}}^2\, b}{2c^2(c-a)}\,, \\
\mathcal{F}_2(k) &= \frac{\ell_{\mathrm{fluc}}^2\, b}{a(a^2-c^2)}\,.
\end{cases}
$$

In order to find the maxima of $\mathcal{R}(k,t)$, which defines the fastest growing mode $k = k_{\mathrm{max}}$, we calculate the derivative of Equation (4.37) with respect to k to obtain

$$\frac{1}{te^{\mathcal{G}t}}\frac{\partial \mathcal{R}}{\partial k} = \frac{1}{t}\frac{d\mathcal{F}_1}{dk} + \frac{d\mathcal{G}}{dk}\mathcal{F}_1 + \frac{1}{te^{\mathcal{G}t}}\frac{d\mathcal{F}_2}{dk}\,, \tag{4.38}$$

setting $\partial \mathcal{R}/\partial k = 0$. As $1/t$ and $e^{-\mathcal{G}t}$ vanish as $t \to \infty$, and $\mathcal{F}_1(k_{\max}) \neq 0$, the equation for determining k_{max} is simply

$$\left.\frac{d\mathcal{G}}{dk}\right|_{k=k_{\max}} = \frac{1}{t_0} \left.\frac{d(c-a)}{dk}\right|_{k=k_{\max}} = 0 \,. \qquad (4.39)$$

This is in fact the same equation as that found by Eggers and Dupont in [28], who neglected fluctuations entirely. However, as breakup occurs in a finite time, both terms in Equation (4.36) could play a role in determining $k_{\max}$ at any instant, with the second term increasing in importance as $\ell_{\text{fluc}}/R_{\text{i}}$ increases (all else being constant).

4.3   Results and discussion

$t = 0.00$ ns

$t = 2.88$ ns

$t = 3.75$ ns
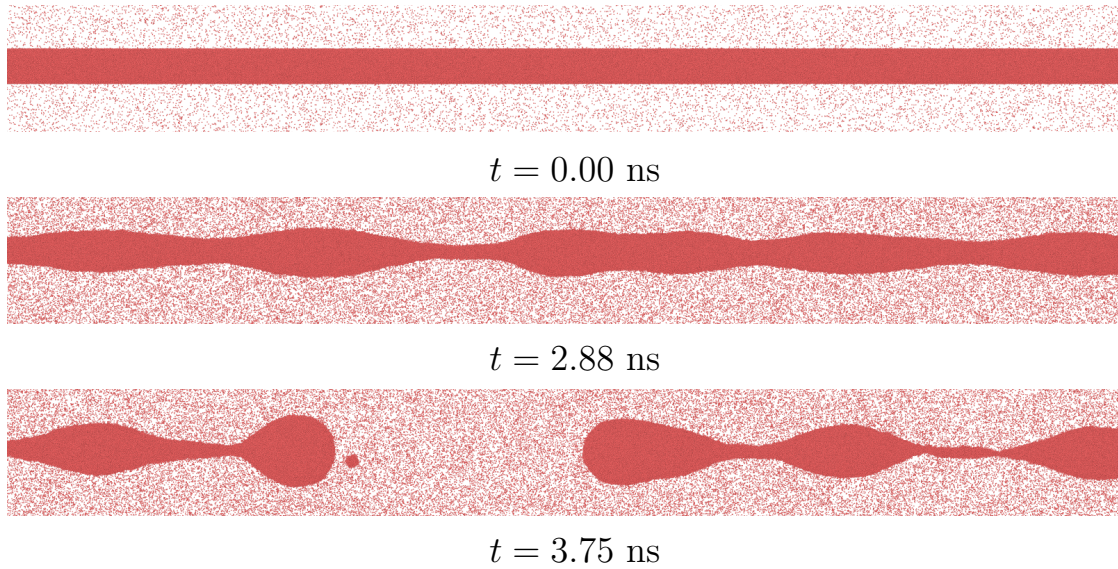
Figure 4.3: Molecular dynamics simulation of the Rayleigh-Plateau instability showing a liquid cylinder (*Cylinder 1*) breaking into droplets.

We test our hypothesis MD simulations (in Figure 4.3) on long cylinders $L/r_0 = 160$ of three different radii: *Cylinder 1* ($r_0 = 5.76$ nm, 2.1×10^6 particles), *Cylinder 2* ($r_0 = 2.88$ nm, 2.8×10^5 particles), and *Cylinder 3* ($r_0 = 1.44$ nm, 4.6×10^4 particles). The simulation box (57 nm $\times$ 57 nm $\times L$ in the x, y and z directions, respectively) has periodic boundary conditions imposed in all directions and is filled with Lennard-Jones (LJ) fluid, introduced in Chapter 3. Despite the low density of vapours, the geometry of the periodic boundaries (a box rather than a cylinder) may cause radial anisotropy,

46

contradicting the axisymmetric assumption. So the size of the entire simulation domain is at least 10 times bigger than the thread radius to avoid this problem.

The initial configuration is created from the output of separate liquid-only and vapour-only simulations. Both simulations are carried out in boxes (57 nm $\times$ 57 nm $\times L$) with periodic boundary conditions. The numbers of liquid and vapour molecules are determined by respective densities of 1398 kg/m^3 and 3.22 kg/m^3, which correspond to the saturated liquid and vapour densities at a temperature of 84.09 K [108]. These systems are equilibrated to the desired temperature by using canonical ensemble (NVT) with a Nosé-Hoover thermostat with 100000 steps. The time step is set as 2.5 femtoseconds. After equilibrium results achieved, a cylinder (with the radius, r_0 and length, L), cut from the liquid box, is implemented into the vapour box with the central cylinder region subtracted to construct the initial configuration. Since the equilibrium state (molecular positions and velocities) cannot be conserved after the cutting and merging process, simulations at the initial stage would provide some unphysical predictions. However, the initial stage (thousands of steps) is so short compared to the entire dynamics process (millions of steps) that the influence of the initial configuration can be neglected.
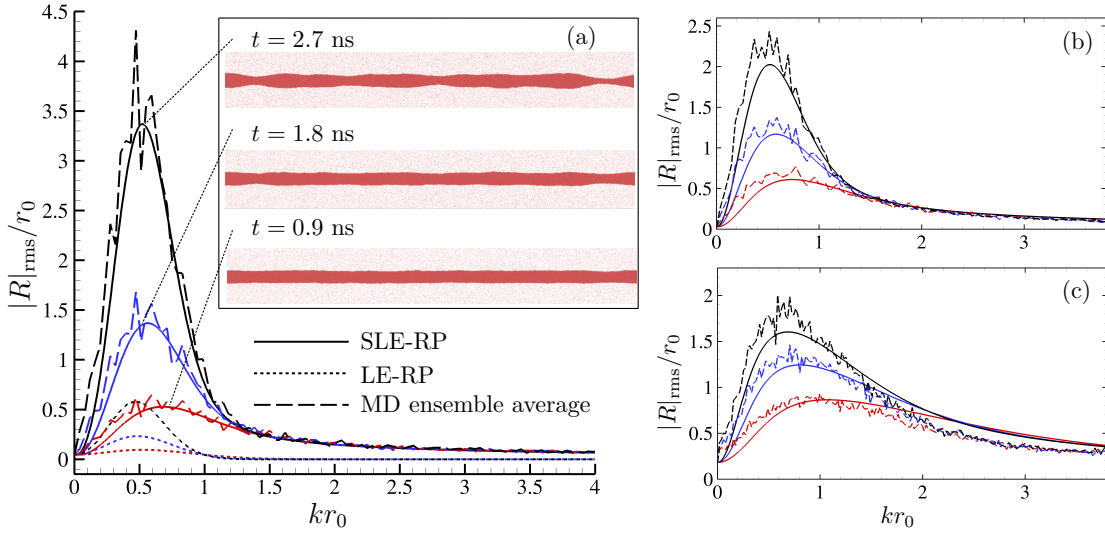
Figure 4.4: The r.m.s of dimensionless modal amplitude versus dimensionless wavenumber; a comparison of ensemble-averaged MD data and Equation (4.36) at various time instants.
(a) *Cylinder 1*; Selected MD realisations are shown at these instances in the inset;
(b) *Cylinder 2*, the three time steps are: 0.23 (red), 0.47 (blue), 0.70 (black) /ns;
(c) *Cylinder 3*, the three timesteps are: 0.062 (red), 0.125 (blue), 0.100 (black) /ns.

Based on the methods (extracting liquid properties from MD) in Chapter 3, we

47

obtain $\nu = 1.76 \times 10^{-7} \mathrm{m^2\ s^{-1}}$ and $\gamma = 1.42 \times 10^{-2}\ \mathrm{N\,m^{-1}}$.
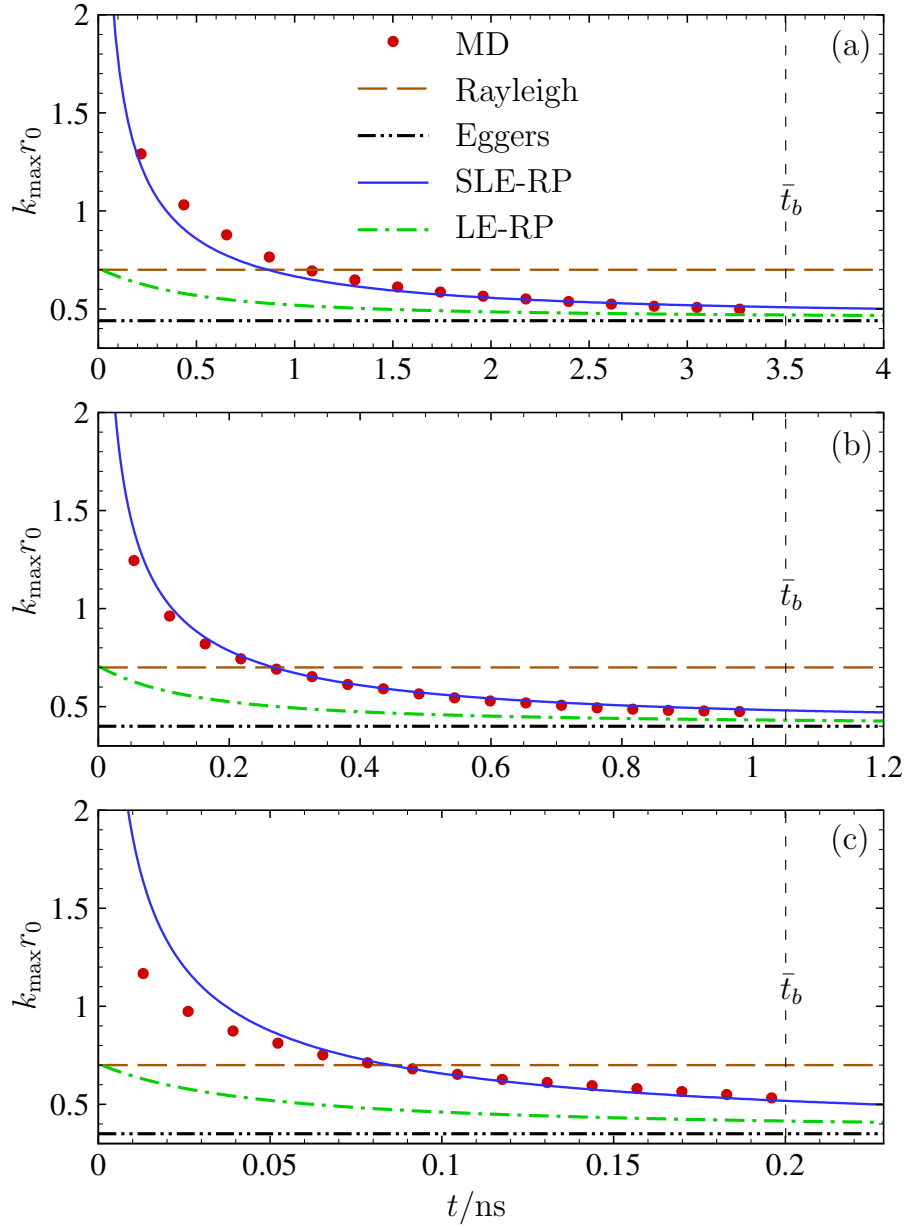
Figure 4.5: Evolution in time t of the wavenumber with greatest amplitude k_{max} for (a) *Cylinder 1* (b) *Cylinder 2* and (c) *Cylinder 3*. Red dots and solid lines are the maximum predicted by MD (interpolation) and the SLE-RP respectively. Average breakup time, $\bar{t}_{\mathrm{b}}$, is obtained from the MD data.

To gather statistics, multiple independent MD simulations (*Cylinder 1*: 30, *Cylinder 2*: 45 and *Cylinder 3*: 100) are performed. The interface shape in MD is extracted

from axially distributed annular bins based on a threshold density (more details are given in Appendix D). For each realisation, a discrete Fourier transform of the interface disturbance (h) is performed and then an ensemble average at each time (see Appendix D for more information) allows us to produce the results shown in Figure 4.4 (dashed lines) and Figure 4.5 (red dots). Using the initial condition from the MD to extract R_i, remarkably good agreement with the SLE-RP is obtained, giving us confidence that our approach captures the essential physics.

The MD results in Figure 4.4 illustrate that there exists a modal distribution which varies with time, becoming sharper at later times, and extracting k_{max} from data of this class yields the dominant modes in Figure 4.5. Note that k_{max} of the MD is not extracted from the spectrums directly because of their discontinuities. Rational polynomial functions (in-built 'toolbox' in MATLAB) are employed to fit the MD data with smooth spectrums generated, whose peaks are extracted as k_{max}. Figure 4.5 confirms that k_{max} tends to the Eggers and Dupont result as $t \to \infty$. However, k_{max} at the average breakup time (which ultimately determines drop size) is consistently overpredicted by Rayleigh's inviscid result, as seen in previous MD, and underpredicted by the Eggers and Dupont model (valid across all values of viscosity) — particularly for the smallest radius (*Cylinder 3*) where $k_{max} = 0.52/r_0$ in the MD and $k_{max} = 0.35/r_0$ from Eggers and Dupont. Here, the breakup time of the MD is defined as the moment when the minimum thread thickness is smaller than the atomic scale, namely $h_{min} < \sigma$. $\bar{t}_b$ represents the averaged breakup time of all the realisations. The modal analysis based purely on the LE-RP also underpredicts the MD data and fails to exhibit the dominant short wavelength modes we observed at early times. In contrast, the SLE-RP curves in both Figs. 4.4 and 4.5 give excellent agreement with the MD and underline the critical role of thermal fluctuations in the instability mechanism at the nanoscale.

Intriguingly, the early-time behaviour in Figure 4.5 indicates that $k_{max}r_0$ can be greater than unity, violating the classical stability criterion of Plateau. Therefore, it seems possible that 'fat' cylinders, whose length is below the classical critical stability ($L < L_{crit} = 2\pi r_0$), may be unstable in the presence of fluctuations. To test the hypothesis, we consider Equation (4.36) at the critical point, i.e. when $kr_0 = 1$, to obtain

$$\overline{|R|^2} = |R_i|^2 + \frac{L}{4\pi r_0}\ell_{fluc}^2\left(\frac{\ell_\nu}{r_0}\right)^{\frac{1}{2}}\frac{6at/t_0 + 3e^{-2at/t_0}\left(4e^{at/t_0} - 1\right) - 9}{a^3}. \tag{4.40}$$

49
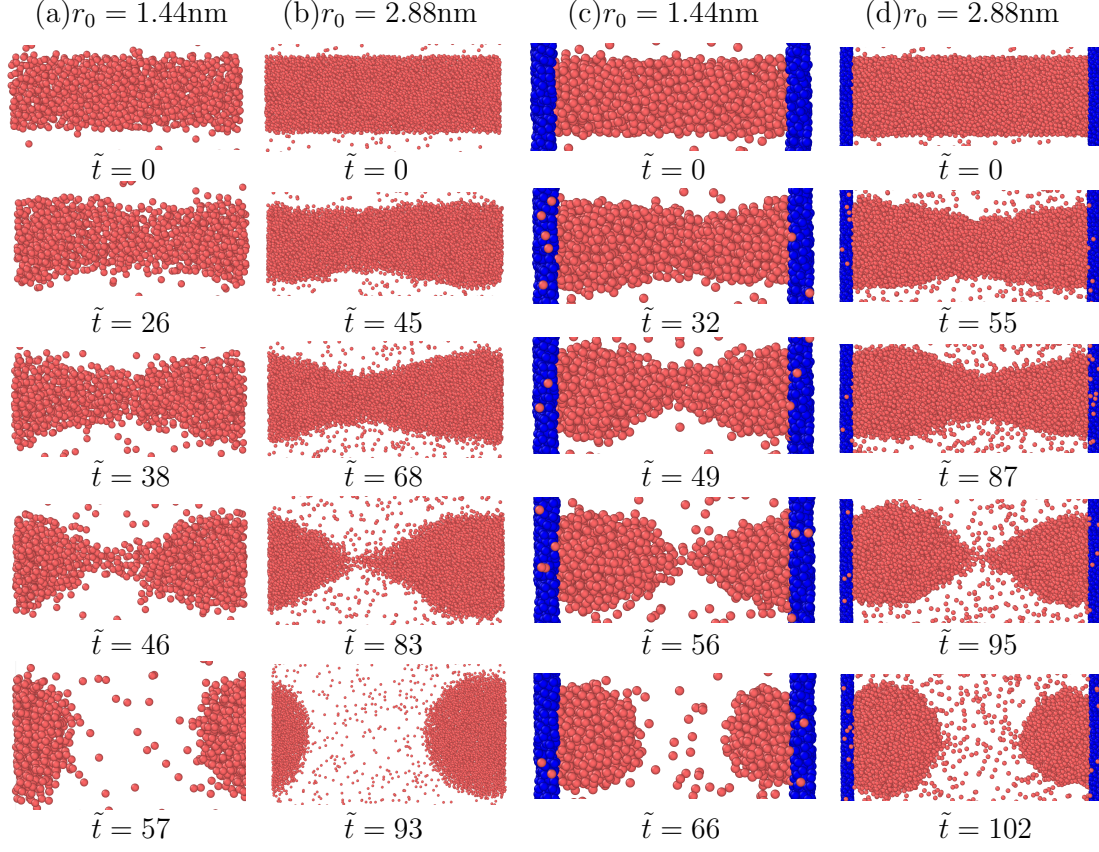
Figure 4.6: Selected realisations for the breakup of classically stable cylinders (i.e. those satisfying the Plateau stability criterion). The two simulations on the left satisfy periodic boundary conditions, while those on the right are bounded by a wall (in blue). Non-dimensional time $\tilde{t} = t/t_0$.

Notably, the contribution from LE equations (the first term on the right hand side of Equation (4.40)) is a constant; so, according to the classical model, the initial disturbance neither decays or grows. Hence, it is critically stable. However, the second term (purely due to fluctuations) grows in proportion to t as $t \to \infty$, giving a potential mechanism for breakup. This suggests that cylinders of the critical length, and perhaps shorter, are likely to be unstable at the nanoscale. To verify these conclusions, we perform a further series of MD experiments for cylinders of two radii ($r_0 = 1.44, 2.88$ nm) that are slightly shorter than the critical length L_{crit}, so that all classically unstable (long) wavelengths are suppressed by the domain size. This has been performed using two different flow configurations, one in which periodic boundary conditions are applied and the other in which the liquid is confined by a solid wall, in order to demonstrate the

robustness of this phenomenon.

The four cylinders in Figure 4.6, of different radii, both have length $L = 6r_0 < L_{\text{crit}}$ which satisfy Plateau's stability criterion. And yet all breakup in finite time, supporting our conclusion from SLE-RP that fat cylinders can indeed become unstable at the nanoscale. Notably, the breakup shapes resemble the double-cone profiles first observed by [1].
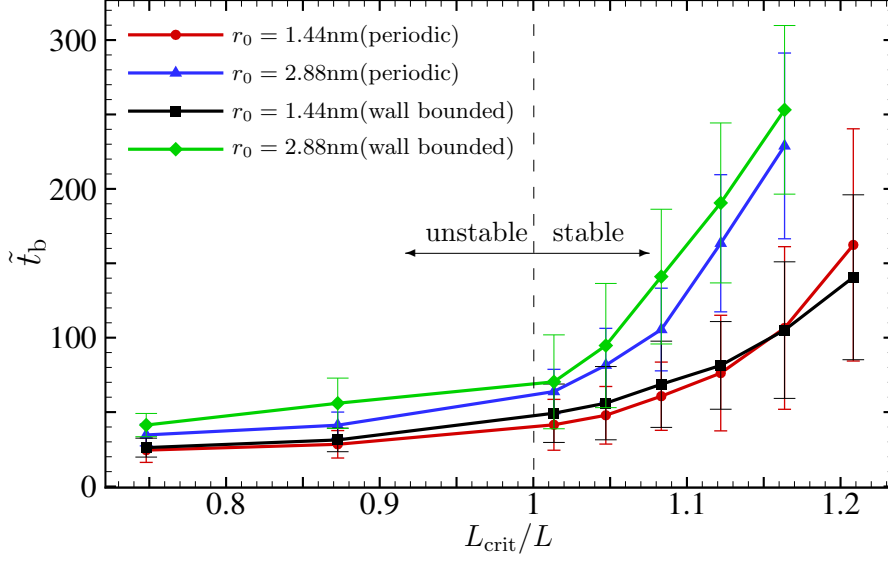
Figure 4.7: The non-dimensional breakup time ($\tilde{t}_{\text{b}} = t_{\text{b}}/t_0$) of short nano cylinders near the classical stability boundary, obtained from MD. $L_{\text{crit}}/L = 2\pi r_0/L = kr_0$. Error bars represent standard deviations of $\tilde{t}_{\text{b}}$.

Having established the possibility of violating the Plateau criterion at the nanoscale, in Figure 4.7 we show the average breakup time of such cylinders using 50 independent MD simulations for each data point (the standard deviation is indicated). We can make two intuitive observations:

(i) for the smaller radius cylinder, the breakup (which is partly or wholly due to fluctuations) occurs significantly faster;

(ii) as the aspect ratio of the cylinder becomes fatter, crossing the classical stability limit ($L_{\text{crit}}/L > 1$), the average breakup time increases dramatically, as does the variance.

The reason for this is that, at lower aspect ratios, the now stabilising effect of surface tension becomes stronger, and one has to wait longer (on average) for the 'perfect storm'

of fluctuations to arrive that will overcome these and rupture the cylinder. This could explain why previous MD [73] appears to support the classical criterion: to violate the Plateau stability one must either be close to $L_{\mathrm{crit}}/L = 1$ or wait a relatively long time. Notably, while this is a 'long time' in MD, from the perspective of the macroscopic world the timescales on which classical stability is lost are tiny.

4.4 Summary

In this chapter, we first showed that classical RP theories are accurate in describing macroscale experiments, in Section 4.1. Then, in Section 4.2, a new analytical framework, SLE-RP is developed to study the RP instability for the nanoscale while taking into account the influence of thermal fluctuations. With demonstrations from molecular dynamics experiments in Section 4.3, our model enables us to understand two important phenomena:

 (i) the classical model fails to predict the dominant modes,

(ii) Plateau stability boundary is lost.

Chapter 5

Rupture dynamics of nanoscale threads

Despite the success of the analytical model SLE-RP, as shown in Chapter 4, its applicability is limited due to the linear assumption; numerical solutions to the SLE offer much broader applicability than the analytic results, and can be obtained at a small fraction of the computational cost of MD. Therefore, in this chapter we carry out detailed numerical studies to obtain (from lots of independent realisations) a deeper understanding of the statistics of both instability and rupture.

The Chapter is laid out as follows. In Section 5.1 the dimensionless SLE are introduced (§ 5.1.2), with two important dimensionless parameters Oh and Th. A simple yet robust scheme for their numerical solution is proposed in Section 5.2, and its convergence characteristics are demonstrated (§ 5.2.4). In Section 5.3, numerical SLE solutions are verified against known analytical results and validated against MD calculations (introduced in §5.1.1); firstly for initial (linear) instability growth (§5.3.1), and secondly for nonlinear growth of disturbances to the point of rupture (§5.3.2). In Section 5.4 we use the SLE solver, (i) to provide a deeper understanding of the impact of fluctuations on rupture dynamics and (ii) to reach cases that would be computationally intractable for MD.

5.1 MD settings and dimensionless SLE

5.1.1 MD settings

The MD simulations for benchmarks in this chapter are performed on nanoscale threads of water. The simulation box extends $10r_0$, $10r_0$, and L in the x, y and z directions, respectively. The liquid thread is placed in the centre of the domain, and there are periodic boundary conditions imposed in all three directions. Because vapour densities predicted by water molecular models are extremely low ($\approx 0\,\mathrm{kg\,m^{-3}}$ when $T < 350\,\mathrm{K}$), we only need a water cylinder as the initial configuration, which is cut from a liquid bulk, created from equilibrium NVT simulations with a Nosé-Hoover thermostat at a specific temperature. The same ensemble and thermostat is used for the main simulations with the time step, 2.5 femtoseconds.
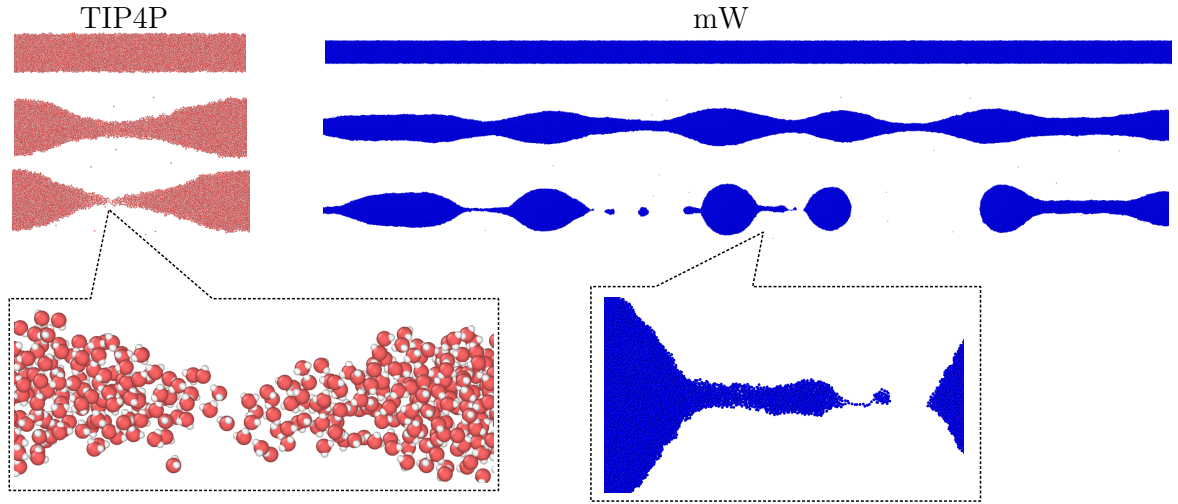
Figure 5.1: MD simulations using the different molecular models for water. Left panel: rupture dynamics of a short thread predicted by the TIP4P/2005; Right panel: perturbation instabilities of a long thread modelled by the mW.

In the present work, liquid water is chosen because of its wide applications and its ability to create a large range of material properties [128]. The detailed properties (e.g. temperature, surface tension, dynamic viscosity) will be listed in the relevant sections, where γ and ν are calculated with the approach in §3.1.3. For the instability validation cases in §5.3.1 (requiring long cylinders) a coarse-grained water molecule model known as mW [115] is adopted, for computational efficiency; whereas for the breakup validation cases in §5.3.2, the TIP4P/2005 water model [110] is used, thus achieving a more accurate result. Selected MD realisations of both models are shown in

Figure 5.1.

5.1.2 Dimensionless stochastic lubrication equations (SLE)

To identify the governing dimensionless parameters in the SLE, we use the following variables as scales of length, time, velocity and pressure, based on (but not confined to) a balance of inertial and surface-tension forces:

$$\tilde{h} = h^*/r_0, \quad \tilde{t} = t^* \Big/ \sqrt{\rho r_0^3/\gamma}\,, \quad \tilde{u} = u^* \Big/ \sqrt{\gamma/(\rho r_0)}\,, \quad \tilde{p} = p^*/(\gamma/r_0)\,. \tag{5.1}$$

Since most quantities in this chapter are nondimensional from this point on, we therefore drop the tilde from the dimensionless symbols and add an asterisk to the dimensional ones as the superscript. Note that this nomenclature is only used in the current chapter. The dimensionless SLE are written as follows:

$$\partial_t u = -uu' - p' + 3\,\mathrm{Oh}\,\frac{(h^2 u')'}{h^2} + \sqrt{\frac{6}{\pi}}\,\mathrm{Th}\,\sqrt{\mathrm{Oh}}\,\frac{(h\mathcal{N})'}{h^2}\,, \tag{5.2}$$

$$\partial_t h = -uh' - u'h/2\,, \tag{5.3}$$

with the full Laplace pressure retained:

$$p = h^{-1}\left(1 + \left(h'\right)^2\right)^{-\frac{1}{2}} - h''\left(1 + \left(h'\right)^2\right)^{-\frac{3}{2}}\,. \tag{5.4}$$

In the dimensionless LE, Oh is all that is needed to characterise the dynamics of free macroscopic threads, but here we obtain an additional dimensionless quantity: the *thermal-fluctuation number*, $\mathrm{Th} = l_\mathrm{T}/r_0$, to express the relative intensity of interface fluctuations, where $l_\mathrm{T} = \sqrt{k_\mathrm{B} T/\gamma}$ is the characteristic thermal fluctuation length. When $\mathrm{Th} = 0$, the classical model (LE) is recovered.

5.2 Numerics for the SLE

5.2.1 MacCormack scheme

In order to solve the full nonlinear SLE, we use the MacCormack method [129], a simple second-order finite difference scheme in both time and space. The solution at each time level is defined by two arrays, $\{h_i\}_{i=1}^n$ and $\{u_i\}_{i=1}^n$. Here, n is the number of mesh points. The time-derivative terms are approximated by $(h_i^{t+1} - h_i^t)/\triangle t$ and $(u_i^{t+1} - u_i^t)/\triangle t$. The

numerical method proceeds in two steps. There is a predictor step:

$$\left(\begin{array}{c} \overline{u_i^{t+1}} \\ \overline{h_i^{t+1}} \end{array} \right) = \left(\begin{array}{c} u_i^t \\ h_i^t \end{array} \right) + \mathbf{F}(u_i^t, h_i^t)\triangle t, \tag{5.5}$$

and a corrector step:

$$\left(\begin{array}{c} u_i^{t+1} \\ h_i^{t+1} \end{array} \right) = \left(\begin{array}{c} u_i^t \\ h_i^t \end{array} \right) + \frac{\triangle t}{2} \left[\mathbf{F}(u_i^t, h_i^t) + \overline{\mathbf{F}}(\overline{u_i^{t+1}}, \overline{h_i^{t+1}}) \right], \tag{5.6}$$

where $\overline{u_i^{t+1}}$ and $\overline{h_i^{t+1}}$ are "provisional" values at time level $t+1$, and $\mathbf{F}$ represents all the partial spatial derivative terms on the right-hand side. For the explicit expression of $\mathbf{F}$, two differential operators, $\triangle_{\mathrm{f}}$ and $\triangle_{\mathrm{b}}$ are introduced to represent forward and backward difference respectively:

$$\begin{aligned} \triangle_{\mathrm{f}} f &= (f_{i+1} - f_i)/(z_{i+1} - z_i), \\ \triangle_{\mathrm{b}} f &= (f_i - f_{i-1})/(z_i - z_{i-1}). \end{aligned} \tag{5.7}$$

$\mathbf{F}$ is discretised by the forward difference for the predictor step, written as

$$\mathbf{F}(u_i^t, h_i^t) = \left[\begin{array}{c} -u_i^t \triangle_{\mathrm{f}} u_i^t - \triangle_{\mathrm{f}} p_i^t + \frac{3\,\mathrm{Oh}}{(h_i^t)^2} \frac{(h_{i+1}^t)^2 \triangle_{\mathrm{f}} u_i^t - (h_i^t)^2 \triangle_{\mathrm{b}} u_i^t}{z_{i+1} - z_i} + \sqrt{\frac{6}{\pi}} \frac{\mathrm{Th}\sqrt{\mathrm{Oh}}}{(h_i^t)^2} \triangle_{\mathrm{f}}(h_i^t N_i^t) \\ -u_i^t \triangle_{\mathrm{f}} h_i^t - h_i^t \triangle_{\mathrm{f}} u_i^t / 2 \end{array} \right], \tag{5.8}$$

while the backward method is applied for $\overline{\mathbf{F}}$,

$$\overline{\mathbf{F}}(\overline{u_i^{t+1}}, \overline{h_i^{t+1}}) =$$

$$\left[\begin{array}{c} -\overline{u_i^{t+1}} \triangle_{\mathrm{b}} \overline{u_i^{t+1}} - \triangle_{\mathrm{b}} \overline{p_i^{t+1}} + \frac{3\,\mathrm{Oh}}{(\overline{h_i^{t+1}})^2} \frac{(\overline{h_i^{t+1}})^2 \triangle_{\mathrm{f}} \overline{u_i^{t+1}} - (\overline{h_{i-1}^{t+1}})^2 \triangle_{\mathrm{b}} \overline{u_i^{t+1}}}{z_i - z_{i-1}} + \sqrt{\frac{6}{\pi}} \frac{\mathrm{Th}\sqrt{\mathrm{Oh}}}{(\overline{h_i^{t+1}})^2} \triangle_{\mathrm{b}}(\overline{h_i^{t+1}} N_i^t) \\ -\overline{u_i^{t+1}} \triangle_{\mathrm{b}} \overline{h_i^{t+1}} - \overline{h_i^{t+1}} \triangle_{\mathrm{b}} \overline{u_i^{t+1}} / 2 \end{array} \right]. \tag{5.9}$$

5.2.2 Uncorrelated noise

By construction, after enforcing the fluctuation-dissipation balance, the covariance of the stochastic term in Equation (5.3) is

$$\langle \mathcal{N}(z,t)\mathcal{N}(z',t') \rangle = \delta(z - z')\delta(t - t'), \tag{5.10}$$

where the presence of a Dirac delta function ensures infinitely small temporal/spatial correlation functions; i.e. the noise term is temporally and spatially uncorrelated. To

represent $\mathcal{N}$ numerically, we introduce computer-generated random numbers, N_i^t, that are normally distributed with zero mean and unit variance. The delta function in Equation (5.10) can be approximated by a 2D rectangular (boxcar) function (in t and z) that is non-zero over a time step ($\triangle t$) and grid spacing ($\triangle z$). The amplitude of the rectangular function, $1/(\triangle t \triangle z)$, is such that the integral properties of the delta function are preserved, i.e. $\int_{-\infty}^{\infty} \int_{-\infty}^{\infty} \delta(z,t) \, dz \, dt = 1$ [122]. The complete noise term is thus discretised by

$$\mathcal{N} \approx N_i^t / \sqrt{\triangle t \triangle z} \,. \tag{5.11}$$

Equation (5.11) provides a robust and accurate numerical performance when used in conjunction with linear equations, e.g. one-dimensional LLNS [130], or for the linearised SLE. However, the full SLE are nonlinear (including the stochastic driving force: $(h\mathcal{N})'/h^2$), which creates stability issues that exacerbate as $\triangle z$ and $\triangle t$ become smaller and the amplitude of noise becomes larger (see Equation (5.11)). Consequently, for some cases, it is impossible to achieve a spatially and temporally resolved result (i.e. one that converges as $\triangle z \to 0$ and $\triangle t \to 0$).
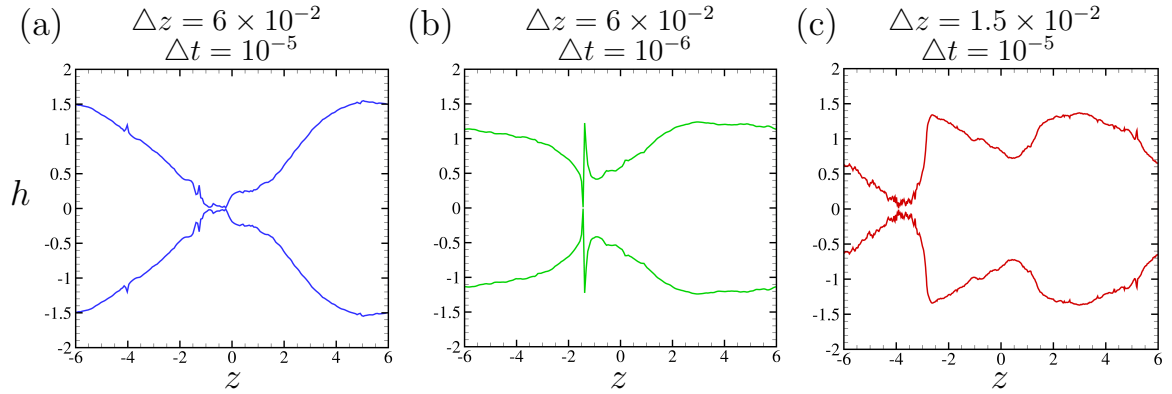
Figure 5.2: Rupture profiles obtained with the uncorrelated noise model: non-convergence of $\triangle z$ and $\triangle t$

      Figure 5.2 shows an example of the non-convergence about rupture profiles with $Oh = 1$ and $Th = 0.1$. Here Figure 5.2 (a) and (b) have the same grid size, while (a) and (c) have the same time step. Obvious deviations can be found in the results above, where profiles with a finer time step (green lines) and grid size (red lines) seem more 'physically unreasonable'.

5.2.3 A simple correlated noise model

As a straightforward solution to this problem, we propose a numerical method where, beneath a certain scale, the noise becomes spatially and temporally correlated; thus remaining finite as $\triangle z \to 0$ and $\triangle t \to 0$. MD results show that this 'correlation scale' is much smaller than any scale of interest in this chapter.

While this solution is largely pragmatic in nature, it actually reflects the physics better than uncorrelated noise. Figure 5.3 (a) shows the temporal autocorrelation function of shear stress fluctuations in a bulk liquid, as calculated by MD (in a $3\,\text{nm}^3$ periodic cube of TIP4P water at $T = 340\text{K}$). Notably, when time scales are smaller than a picosecond the fluctuations become correlated; we find a similar situation in the spatial fluctuations of stress in MD.

Motivated by these MD results, into our SLE we introduce a correlation time scale, T_c, and correlation length scale, L_c. Then the time step and grid spacing must be equal or smaller than T_c and L_c, respectively. Inside the correlation scale, a simple linear interpolation is applied between uncorrelated random noise at the end points of the correlation interval (as illustrated in Figure 5.3 (b) for temporal noise). The uncorrelated noise (which is interpolated between) has a mean of zero and a variance depending on L_c and T_c.
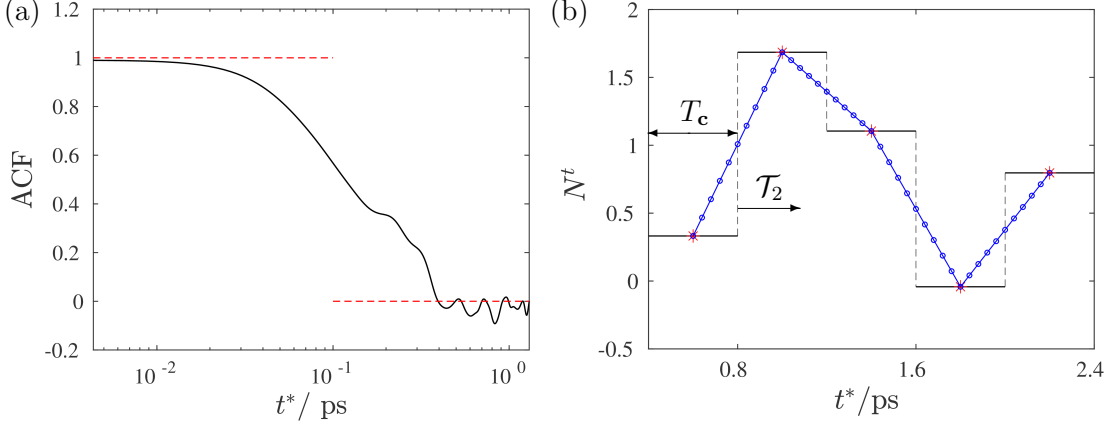
Figure 5.3: (a) The auto-correlation function (ACF) for shear stress, obtained from an MD simulation of a periodic cube of liquid; (b) an illustration of the linear interpolation used in evaluating the temporal stochastic term N^t.

In order to derive the explicit expression for variance, we separate spatial and temporal fluctuations and then focus solely on temporal fluctuations. The variance of

the temporal fluctuation is

$$\langle N(t)N(t')\rangle = A_{\mathrm{f}}^2 \delta(t - t')\,.$$

Here, A_{f} represents the noise amplitude. If we define the 'average noise' over a period of T_{N}

$$\overline{N} = \left[\int_0^{T_{\mathrm{N}}} N(t)dt\right] /T_{\mathrm{N}}\,,$$

the variance of $\overline{N}$ can be obtained with the process shown below

$$\left\langle \frac{\int_0^{T_{\mathrm{N}}} N(t)dt}{T_{\mathrm{N}}} \frac{\int_0^{T_{\mathrm{N}}} N(t')dt'}{T_{\mathrm{N}}} \right\rangle$$

$$= \frac{1}{T_{\mathrm{N}}^2} \int_0^{T_{\mathrm{N}}} \int_0^{T_{\mathrm{N}}} \langle N(t)N(t')\rangle \, dtdt'$$

$$= \frac{A_{\mathrm{f}}^2}{T_{\mathrm{N}}^2} \int_0^{T_{\mathrm{N}}} \int_0^{T_{\mathrm{N}}} \delta(t - t')dtdt'$$

$$= A_{\mathrm{f}}^2/T_{\mathrm{N}}\,. \tag{5.12}$$

The interpolated noise we proposed (in Figure 5.3 (b)) can be written as

$$N(t) = \sum_{i=1}^{\infty} \left[(1 - \mathcal{T}_i)X_i + \mathcal{T}_i X_{i+1}\right] \cdot \Pi(\mathcal{T}_i - 1/2)\,. \tag{5.13}$$

Here, X_i are normal distributed random numbers with mean zeros. Π is the hat function and $\mathcal{T}_i$ is defined as

$$\mathcal{T}_i = \frac{t - i \cdot T_{\mathrm{c}}}{T_{\mathrm{c}}} \in [0, 1]\,.$$

The $\overline{N}$ can be calculated as

$$
\begin{aligned}
\overline{N}|_0^{T_N} &= \frac{1}{T_N} \int_0^{T_N} N(t)dt \\
&= \frac{1}{T_N} \int_0^{T_N} \sum_{i=1}^{\infty} [(1 - \mathcal{T}_i)X_i + \mathcal{T}_i X_{i+1}] \cdot \Pi(\mathcal{T}_i - 1/2)dt \\
&= \frac{T_c}{T_N} \int_0^1 \left[\sum_{j=1}^{T_N/T_c} (1 - \mathcal{T}_i)X_j + \mathcal{T}_i X_{j+1} \right] d\mathcal{T}_i \\
&= \frac{T_c}{T_N} \sum_{j=1}^{T_N/T_c} \left[(\mathcal{T}_i - \frac{\mathcal{T}_i^2}{2})X_j + \frac{\mathcal{T}_i^2}{2} X_{j+1} \right] |_{\mathcal{T}_i=0}^{\mathcal{T}_i=1} \\
&= \frac{T_c}{2T_N} \sum_{j=1}^{T_N/T_c} (X_j + X_{j+1}) .
\end{aligned}
\tag{5.14}
$$

When $T_N \gg T_c$, this is approximately:

$$
\overline{N}|_0^{T_N} = \frac{T_c}{T_N} \sum_{j=1}^{T_N/T_c} X_j .
\tag{5.15}
$$

So the variance of $\overline{N}$ is then:

$$
\mathrm{Var}(\overline{N}) = \frac{T_c}{T_N} \mathrm{Var}(X_i) .
\tag{5.16}
$$

Because $\mathrm{Var}(\overline{N})$ should equal the theoretical result in Equation (5.12), we can obtain that:

$$
\mathrm{Var}(X_i) = A_f^2/T_c .
\tag{5.17}
$$

Similar processes can be applied to spatial noise. Therefore, the variance of this new numerical noise model is $1/(T_c \cdot L_c)$.

5.2.4 Time-step and grid-size convergence

In order to test the integrity of the SLE numerical approach introduced above, we consider the simulation of a short thread ($r_0 = 2.5$ nm, $L = 10$, Oh $= 1.07$, and Th $= 0.11$) with an increasingly fine time step and grid spacing. Note that for this case a model using uncorrelated noise would not converge.

We set dimensional $T_c^* = 0.01$ ps and $L_c^* = 0.5$ nm for all the simulations presented in this chapter (corresponding to dimensionless $T_c = 4.66 \times 10^{-5}$ and $L_c = 0.2$). These

were chosen to be similar to those seen in our MD data. Notably, since this is a stochastic system, it is the convergence of the ensemble-averaged quantities that we are concerned with; here the ensemble consists of 100 independent simulations.
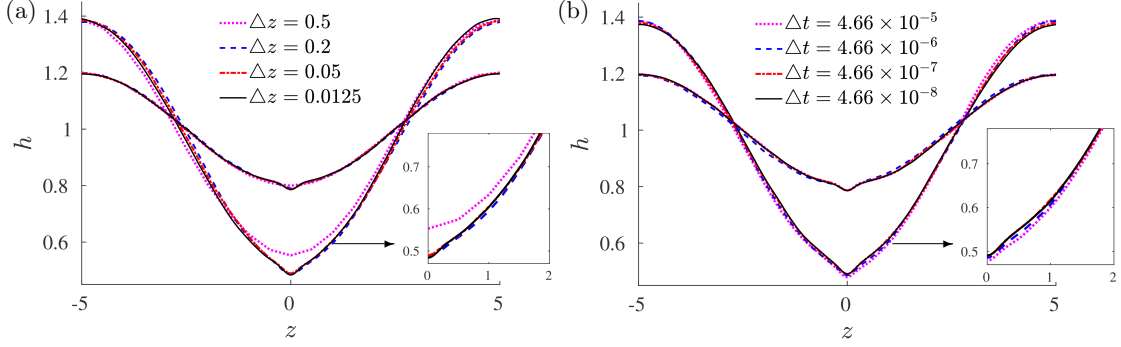
Figure 5.4: Ensemble-averaged interface profiles at two time instances ($t_1 = 4.66 \times 10^{-2}$ and $t_2 = 1.69$) for (a) decreasing grid-size with fixed time step ($\triangle t = 4.66 \times 10^{-7}$) and (b) decreasing time step with fixed grid size ($\triangle z = 0.05$).
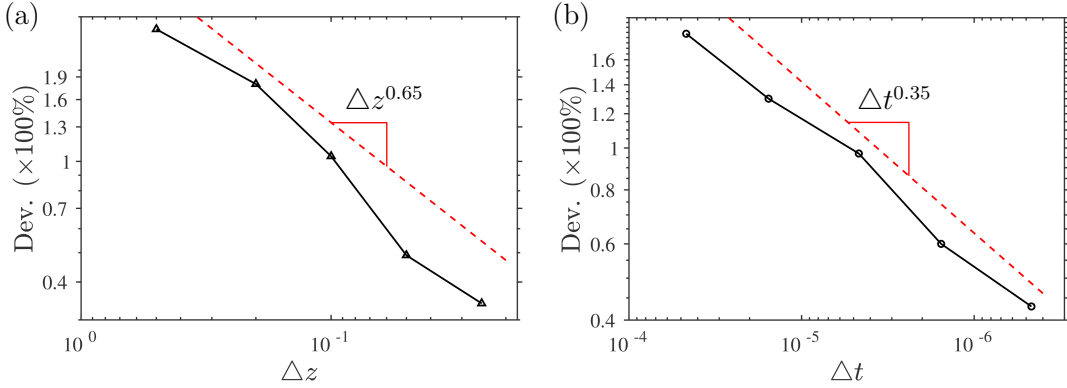
Figure 5.5: Convergence characteristics for decreasing (a) grid size and (b) time step. Average (over z) deviation of ensemble-averaged interface profiles to the finest resolution profile in Figure 5.4 (a) and (b), respectively.

The ensemble-averaged interface profiles at two time instances are plotted in Figure 5.4 for (a) varying grid size and (b) varying time step. Note that in this chapter we plot all interface and rupture profiles relative to the minimum point; i.e., we plot h against $z - z_{\min}$, where $z_{\min}(t)$ is the location of the minimum in thread radius at any instant in time. To better demonstrate the convergence of the method, we calculate the average deviation of each ensemble-averaged profile to that with the finest resolution

calculated; Figure 5.5 confirms that this deviation steadily decreases with increasing (a) spatial and (b) temporal resolution; i.e., it converges. However, the convergence rate is quite slow, probably because discontinuities exist between the correlated scales of the noise model. So continuous noise models (e.g. nonlinear interpolation) would be needed, which should be the subject of future investigation. Moreover, numerical schemes are also worth testing to check the influence of different orders of accuracy on the convergence.

5.2.5   Comparison with Grün's model
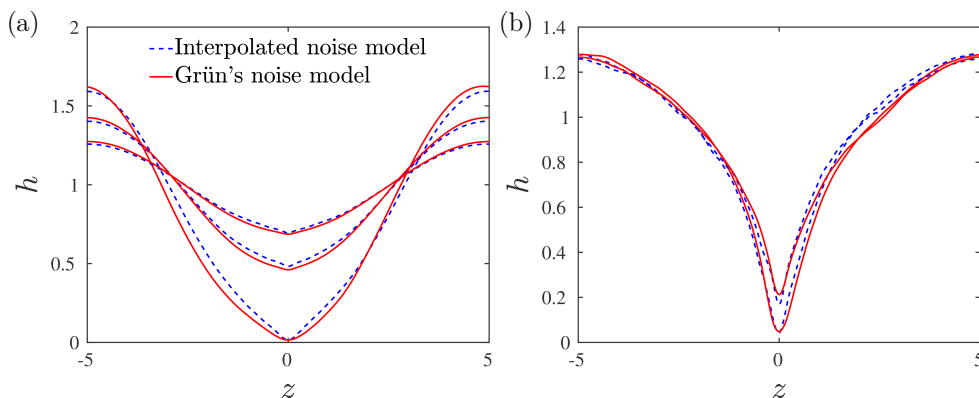
Figure 5.6: Ensemble-averaged interface profiles obtained from our noise model (dashed lines) and Grün's [78] (solid lines) at (a) three time instances ($t_1 = 0.175$, $t_2 = 1.42$ and $t_3 = 2.67$) with Oh = 1.00 and Th = 0.0951, and (b) two time instances ($t_1 = 0.200$ and $t_2 = 1.40$) with Oh = 5.51 and Th = 0.521.

Note that a spatially correlated but temporally uncorrelated noise model has been developed by Grün [78] for the stochastic thin-film equation (see Appendix E for more details). Here, we incorporate this model into our solver (for liquid threads) and compare it with the approach we presented above. Two test cases with different Oh and Th are solved numerically with $\triangle t = 1 \times 10^{-5}$ and $\triangle z = 0.05$. Figure 5.6 illustrates mean interface profiles (from 50 realisations) at different time instances, where good agreement is found between our noise model and Grün's. However, Grün's model is not available for the temporal convergence due to its temporally uncorrelated noise term, while our model has the advantage, not only of simplicity, but also of being able to produce spatio-temporally correlated noise.

5.3 Numerical verification and validation

Having demonstrated the convergence, the numerical solutions are verified and validated by the analytical models and MD simulations at both (i) the linear stage for instability in § 5.3.1 and (ii) the nonlinear stage for the rupture in § 5.3.2.

5.3.1 Linear instability and thermal capillary waves

In this section, SLE-RP in Chapter 4 has been employed as a benchmark for the numerical solutions of the SLE introduced above (Section 5.2). The SLE-RP can be written in a dimensionless form as follows:

$$|R|_{\mathrm{rms}} = \sqrt{\overline{|R_{\mathrm{LE}}|^2} + \overline{|R_{\mathrm{fluc}}|^2}}\,, \tag{5.18}$$

$$\begin{cases} \overline{|R_{\mathrm{LE}}|^2} = |R_{\mathrm{i}}|^2 e^{-at}\left[\cosh\left(ct/2\right) + \frac{a\sinh(ct/2)}{c}\right]^2, \\ \overline{|R_{\mathrm{fluc}}|^2} = \frac{3L}{\pi}(\mathrm{Th}\sqrt{\mathrm{Oh}}\,k^2)^2\, \frac{(a^2-c^2)-a^2\cosh(ct)-ac\sinh(ct)+c^2e^{at}}{ac^2(a^2-c^2)e^{at}}\,, \end{cases}$$

where

$$a = 3\,\mathrm{Oh}\,k^2 \quad \text{and} \quad c = \sqrt{(9\,\mathrm{Oh}^2-2)k^4 + 2k^2}\,.$$

We also perform MD simulations for comparison, where we adopt a coarse-grain water molecule model, mW [115], to limit the computational resources required for such long threads; in all cases, $L = 100$. The initial radius r_0 and the initial temperature T are selected to obtain specific Oh and Th (shown in Table 5.1): *Threads 1 & 2* have the same Th; *Threads 2 & 3* have the same Oh.

Table 5.1: Case setups of mW

Thread	r_0 (nm)	T (K)	γ (N m^{-1})	ρ (kg m^{-3})	μ (kg m^{-1} s^{-1})	Oh	Th	molecule number
(1)	2.410	275.6	6.53×10^{-2}	1.006×10^3	3.582×10^{-4}	0.90	0.10	147,828
(2)	2.891	354.8	5.85×10^{-2}	0.988×10^3	2.043×10^{-4}	0.50	0.10	250,484
(3)	5.170	304.4	6.29×10^{-2}	1.001×10^3	2.851×10^{-4}	0.50	0.05	1,451,568

For each case we extract statistics from an ensemble of independent simulations (or 'realisations'); 20 for MD and 50 for the SLE (true for the rest of the paper, unless otherwise stated). For each realisation, a discrete Fourier transform of the interface position (which in MD is extracted from axially-distributed annular bins based on a threshold density, similar to the approach in Chapter 4) is applied to get the power spectral density (PSD). The square root of the ensemble-averaged PSD at each time is plotted in Figure 5.7 and compared to the SLE-RP (Equation (5.18)). The agreement between the numerical results and the analytical ones is very good for each case and at
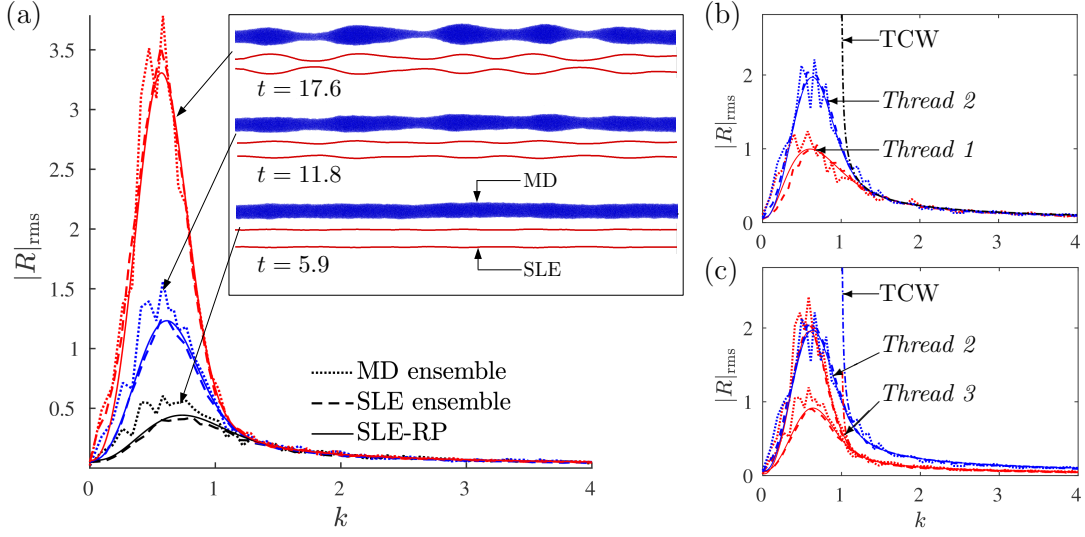
Figure 5.7: The r.m.s. of non-dimensional disturbance amplitude versus non-dimensional wavenumber; a comparison of ensemble-averaged MD simulations (dotted lines), ensemble-averaged SLE simulations (dashed lines), the SLE-RP analytical result (solid lines), and thermal capillary wave (TCW) theory (dashed-and-dotted lines). Comparisons are for (a) *Thread 3* at three (non-dimensional) time instants, t=5.9, 11.8, and 17.6 ; (b) *Threads 1* and *2* (equal Th) for t=9.3; and (c) *Threads 2* (t=9.3) and *3* (t=9.3, 14.7) with equal Oh. The inset in (a) shows selected MD and SLE realisations.

each time, giving us further confidence that the SLE implementation is both numerically sound and capable of capturing nanoscale flow physics (as demonstrated in Chapter 4, where we used a Lennard-Jones potential).

The results in Figure 5.7 (a) show a modal distribution (spectrum) that varies with time. For small wavenumbers ($k < 1$), the spectrum becomes sharper with time, while the spectrum at high wavenumbers ($k >\sim 2$) is static over these time scales; i.e., it quickly reaches its asymptotic limit. This limit can be obtained from Equation (5.18), for $k > 1$, by taking $t \to \infty$:

$$|R|_{\text{rms}} = \sqrt{\frac{L}{2\pi}} \text{Th} \sqrt{\frac{1}{k^2 - 1}} \,. \tag{5.19}$$

This is consistent with the theory for thermal capillary waves in thin-film flows [13, 81], which describes the time-invariant state of a liquid interface by a balance between capillary forces (surface tension) and thermal fluctuations. The crucial difference to thin-film

flows is seen at small wavenumber perturbations, which are unstable for the liquid thread because of the surface tension component acting around the thread's circumference — this is the RP instability. Interestingly, Equation (5.19) indicates that the asymptotic limit for $k > 1$ (i.e. the part of the spectrum composed of thermal capillary waves) only depends on Th, as confirmed in Figure 5.7 (b); *Threads 1* and *2* have the same spectrum at high wavenumbers as Th is fixed. Figure 5.7 (c) shows that the spectrum with the larger Th (*Thread 2*) is broader space (at the same non-dimensional instant); stronger thermal fluctuations lead to a wider distribution of wavenumbers. Since the droplet sizes are related to the dominant wavenumbers, we can expect a broader and enhanced distribution of the probability density function for droplet sizes with larger Th. This hypothesis is supported by results from a fluctuating Lattice Boltzmann model in [76].

5.3.2 Rupture dynamics

In this section, numerical solutions to the fully nonlinear SLE are compared to MD simulations for the rupture dynamics. For the MD in this section, the TIP4P/2005 water model [110] is adopted, with liquid properties as listed in Table 5.2. Here, $L = 12$.

Table 5.2: Case setups of TIP4P/2005

Thread	r_0 (nm)	T (K)	γ (N m^{-1})	ρ (kg m^{-3})	μ (kg m^{-1} s^{-1})	Oh	Th	molecule number
(4)	2.020	358.1	5.38×10^{-2}	0.964×10^3	3.230×10^{-4}	1.00	0.15	10,246
(5)	2.675	316.6	6.09×10^{-2}	0.987×10^3	5.827×10^{-4}	1.45	0.10	23,791
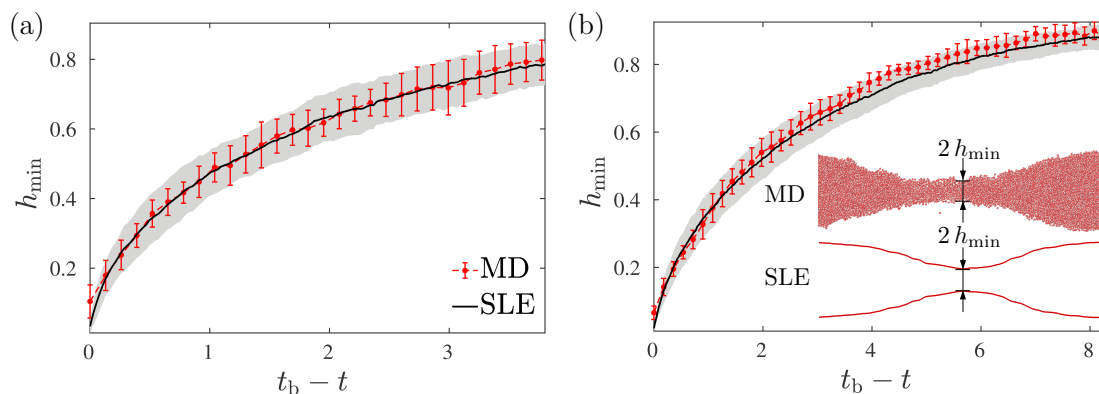
Figure 5.8: Minimum thread radius against time to rupture ($t_{\mathrm{b}} - t$). Comparison of MD and nonlinear SLE for (a) *Thread 4* and (b) *Thread 5*.
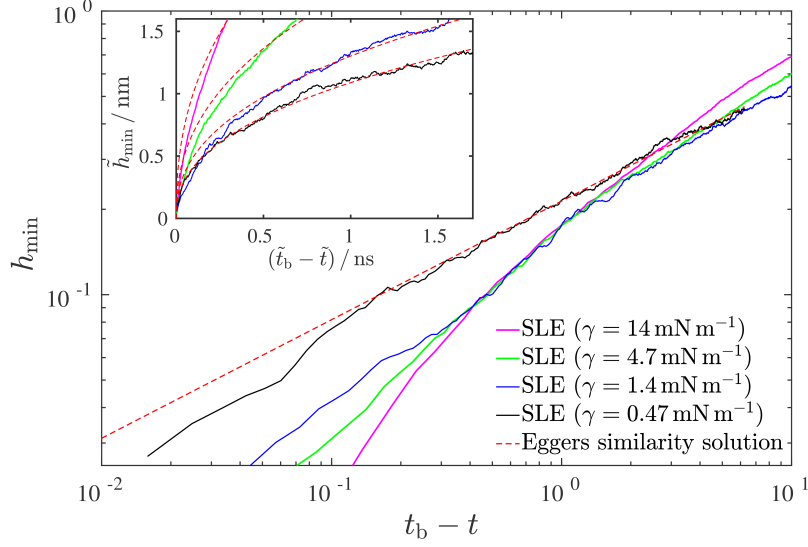
Figure 5.9: The temporal evolution of the minimum thread radius for different values of surface tension: comparison between similarity solutions [2] and an ensemble-average of nonlinear SLE calculations. Here, the maximum value of the surface tension ($\gamma = 14.0\,\text{mN} \cdot \text{m}^{-1}$) comes from liquid argon at $84.0\,\text{K}$.

Our first comparison, Figure 5.8, is for the time evolution of the minimum (over z) thread radius, $h_{\min}(t)$. Since our focus here is on the dynamics near rupture, $h_{\min}$ is plotted against time to rupture, $t_{\text{b}} - t$, where t_{b} is the time at rupture. The red error bars and shadows represent one standard deviation (either side of the mean) for the MD and the SLE, respectively. In the two cases (a) *Thread 4* and (b) *Thread 5*, good agreement is found at all times for the mean; but also, importantly, for the standard deviation.

Figure 5.8 suggests that a power law might govern the progression of the minimum thread thickness to rupture: $h_{\min} \propto (t_{\text{b}} - t)^{\alpha}$. However, despite exhibiting a power law, these results are not described well by the similarity solution proposed by Eggers [2] for which the exponent $\alpha = 0.418$. One possible reason for the discrepancy is that Eggers neglected the influence of surface tension. To explore this explanation, our SLE numerical frame is exploited, as MD is unable to perform such simulations due to inherent restrictions on the variation of liquid properties. We test different values for surface tension with all other parameters (i.e. ρ, μ and T) fixed. The average $h_{\min}(t)$ obtained from 50 realisations is plotted on a logarithmic scale in Figure 5.9. The results indicate that the numerical solutions (solid lines) do tend towards Eggers' similarity
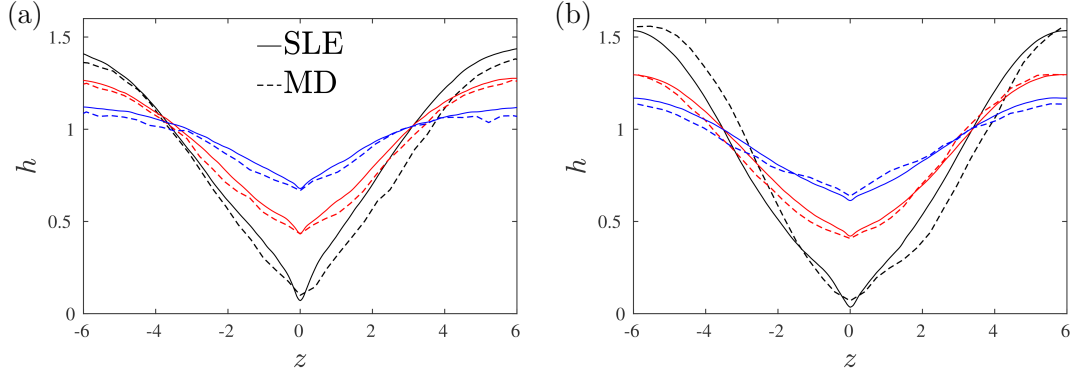
Figure 5.10: Ensemble-averaged interface profiles at three time instants leading to rupture: a comparison of the nonlinear SLE solver (solid lines) and MD data (dashed lines); (a) *Thread 4*: $t_b - t_1 = 0.13$ (black), $t_b - t_2 = 1.04$ (red), $t_b - t_3 = 2.73$ (blue); (b) *Thread 5*: $t_b - t_1 = 0.09$ (black), $t_b - t_2 = 1.44$ (red), $t_b - t_3 = 3.50$ (blue).

solution (red dashed lines) for lower values of surface tension. Note that we vary a dimensional quantity here, in order to connect most transparently with the assumption in Eggers' work. Notably, when surface tension is stronger, the breakup is faster than the analytical prediction, which suggests that the destabilising effect of surface tension can also contribute to the thread dynamics near to rupture. This limit of applicability might also explain the deviation between Eggers' similarity solution and MD results in previous studies [74, 131].

Although the agreement for h_{min} with Eggers' similarity solution is good for low γ, we were unable to make any reasonable comparison between either MD or SLE and the associated universal profiles. The reason is currently unclear and should be the subject of future investigation.

The ensemble-averaged profiles plotted in Figure 5.10 show good overall agreement between the MD and SLE for three time instants leading to rupture. The limitation of bin sizes in the MD data prevents a more detailed comparison of the profile shape. In particular, it is not clear whether the finer features seen in the SLE (namely, the V-notch or 'widow's peak' near to the minimum) are physical because these local features reach the molecular scale and cannot be reliably extracted from the MD.

5.4 Exploiting SLE: breakup beyond MD

Having established its predictive capability, in this section we use the nonlinear SLE solver to further explore the impact of fluctuations on rupture dynamics, over a broader

range of conditions than has been studied previously and for cases that are too computationally demanding to consider with MD. We start, in § 5.4.1, by exploring the shape of the thread at rupture, while in § 5.4.2, we focus on the time evolution of the point of the thread's minimum thickness.

5.4.1 Rupture profiles

Moseler & Landmann[1] were the first to demonstrate, using MD, that thermal fluctuations could lead to a symmetric double-cone rupture profile, and that SLE solutions were also able to capture this (whereas deterministic equations cannot). We reproduce this result for *Thread 5* (see Table 5.2 for parameters) in Figure 5.11. Note that the nonlinear SLE solution can reproduce the MD result, at a fraction of the computational cost, whereas the (deterministic) LE cannot. Here, each MD realisation of *Thread 5* needs about 4600 core hours, while one SLE solution (the finest resolution) only costs less than 1 core hour, i.e. the speed-up is about 10^3.

(a) MD   (b) SLE   (c) LE
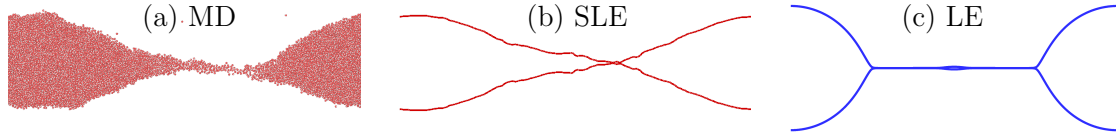
Figure 5.11: *Thread 5* rupture profiles from different models: (a) an MD simulation (b) a selected realisation from the SLE (c) a solution to the LE.

These computational advantages allow the SLE to be applied in a far broader range of conditions than is accessible to MD; as is illustrated in Figure 5.12. Figure 5.12 (a) shows a rupture profile from a macroscopic experiment [17] (with very small Th), which exhibits a satellite droplet between two main drops. This macroscale structure can be captured by the SLE solution (blue lines), since it reverts to the classical LE solution as Th → 0. The rupture profile in Figure 5.12 (b) is from an experiment at several microns, where a colloid-polymer mixture is used to make Th larger, not to generate a nanoscale thread. While the profile here is not a macroscopic one, it cannot be well described as a pure double-cone rupture either. However the SLE can faithfully reproduce such shapes, which are associated with intermediate Th (moderate fluctuations). Figure 5.12 (d) shows that the SLE solution can also capture a pure double-cone profile with a large Th at the nanoscale where only MD experiments are currently available for comparison.

Importantly, however, as done in [1], all the rupture profiles above are *selected* realisations. In other words they have been picked, from numerous independent SLE
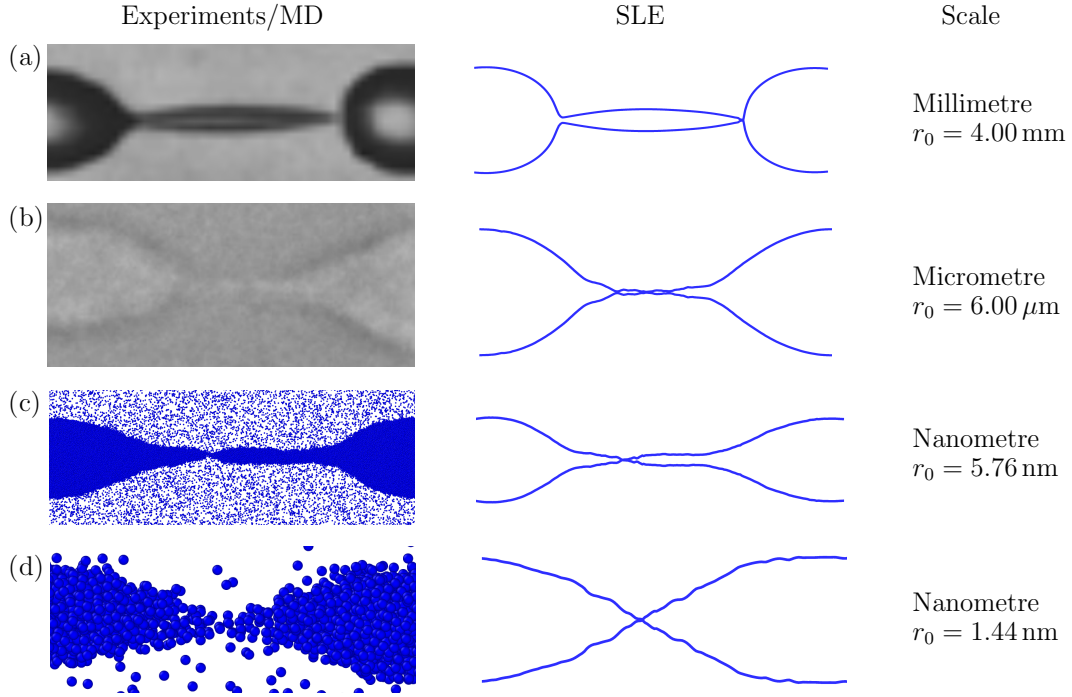
Figure 5.12: Comparison of rupture profiles in experiments (a,b) and MD (c,d) with numerical solutions to the SLE: (a) $\text{Oh} = 2.60 \times 10^{-3}, \text{Th} = 1.17 \times 10^{-7}$, experimental image reproduced from [17]; (b) $\text{Oh} = 1.00, \text{Th} = 4.50 \times 10^{-2}$, experimental image reproduced from [67]; (c) $\text{Oh} = 0.71, \text{Th} = 4.96 \times 10^{-2}$, *Cylinder 1* from Chapter 4; and (d) $\text{Oh} = 1.41, \text{Th} = 1.98 \times 10^{-1}$, *Cylinder 3* from Chapter 4.

results, based on their qualitative similarity to the experimental or MD result to which they are being compared. From these selections, then, it is not possible to ascertain whether the SLE has captured the full dynamics of the rupture, which are of course statistical in nature. To do this we must compare, at the least, the expected and/or most-probable profile, and some measure of the statistical fluctuation. Establishing such a framework is one of the main contributions of this paper.

Figure 5.13 shows a matrix of profiles for varying Th and Oh, obtained using the periodic boundary conditions. For comparison, the left-hand column ($\text{Th} = 0$) contains the rupture profiles as predicted by classical LE. Note that there are two rupture points at $\text{Oh} = 0.02$ and 1, due to the satellite drop. For consistency, we select the left one and move it to the center ($z = 0$). For the stochastic results ($\text{Th} > 0$), each realisation is centred on its rupture point (i.e. the rupture is located at $z = 0$). To preserve large anti-symmetrical features, that would otherwise be averaged out, each centred profile is flipped about $z = 0$ so that $\int_{-L/2}^{0} h \, dz > \int_{0}^{L/2} h \, dz$. In the figures, the solid blue lines are
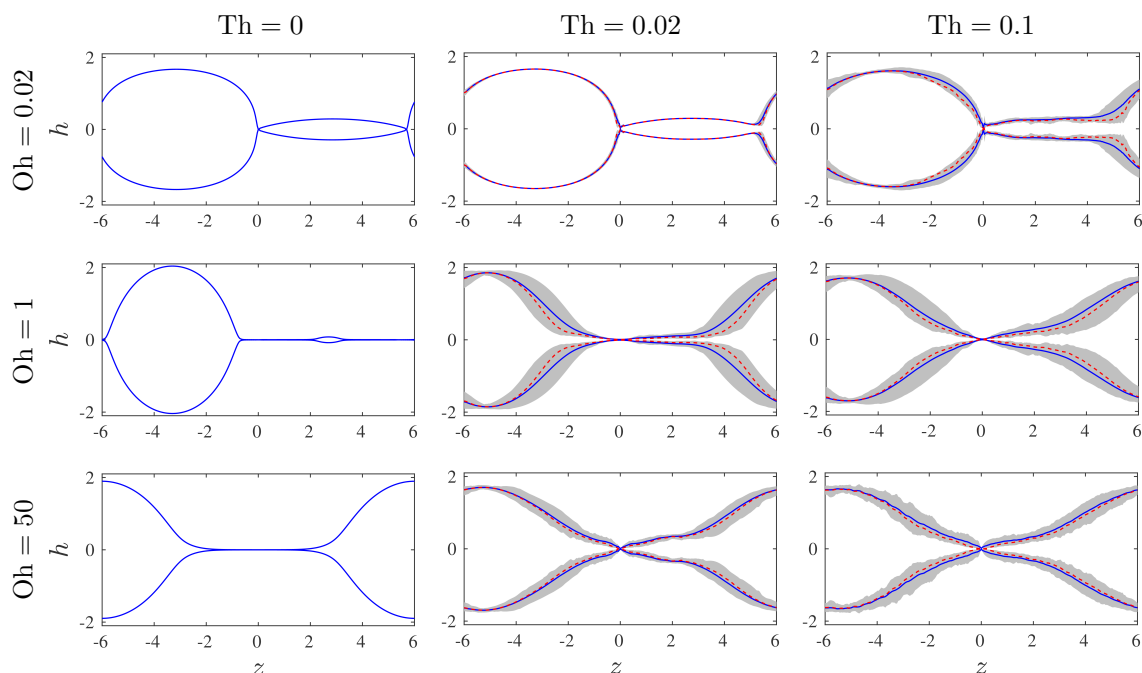
Figure 5.13: Rupture profiles for different combinations of Oh and Th. Solid lines represent the ensemble average (the expected profile), dashed lines an estimate of the most-probable profile, and the region bounded by the 10th and 90th percentile value of $h(z)$ is shaded gray.

the ensemble-averaged rupture profiles (averaged after the centering and transformation described above). Gray shading indicates the region between the 10th and 90th percentile value of h (determined at each z); i.e. for a given z we can be 80% confident that the profile exists within it. Note that as h is always greater than zero, the distribution of its value is not Gaussian, hence the mean/expected profile is not necessarily the same as the most probable. We can crudely approximate the positive distribution of h at any point in z with a Gamma distribution, and from that a most-probable profile (from the peak of the distribution at each z) can be estimated (the red dashed lines). Notably, it is the most-probable profile which Eggers [2] computes from the Fokker-Planck equation for the SLE. In the cases considered here there is little difference between the mean and the estimated most-probable profile.

The bottom right-hand corner profile in Figure 5.13 qualitatively reproduces the findings of Moseler & Landmann [1] and Eggers [2]; a largely symmetric double-cone profile is observed, although it appears this may be better described as an 'hourglass'. One might naively expect that the importance of fluctuations on thread dynamics would

be solely determined by the value of Th (the ratio of the thermal fluctuation scale to the thread radius). However, what is striking is that neither the relative magnitude of fluctuations (the shaded regions) nor the impact of noise on the mean profile is dictated by Th alone. For example, at Th=0.02, the influence of fluctuations on the dynamics can either be negligible or profound, depending on Oh. Nor is it easy to identify a combination of Oh and Th (e.g. $\text{Th}\sqrt{\text{Oh}}$ from Equation (5.2)) that might be useful in singularly describing when fluctuations become important or not; it is, seemingly, a non-trivial interplay of effects as we would expect when inertia, viscosity, surface tension and fluctuations all play a role.

The next most important observation is that, for low Oh, the impact of noise results in an *asymmetric* mean thread profile at rupture (see top right-hand corner image of Figure 5.13). The double-cone profile observed in Moseler & Landmann [1] is not observed here. Instead, we see a quite distinct rupture shape (a drop and funnel), on average, which looks more like typical rupture profiles seen macroscopically when a drop breaks off from a thread. This behaviour is not surprising, as the chance of two points pinching off at precisely the same instance becomes slim when we have fluctuations and indeed this kind of perfect pinch-off is also difficult to reproduce experimentally at the macroscopic level. We stress that these flow conditions are not accessible by our MD simulations at present; the SLE calculations are essential to provide this insight.

5.4.2 Evolution of minimum thread radius

In the classical picture there is the potential for multiple transitions between distinct 'dynamic regimes' (defined by Oh) leading to rupture [40, 37, 41]. The three main regimes, described in Section I, are the viscous regime (V-regime), the inertial regime (I-regime), and the universal regime (VI-regime). These regimes are characterised by a power-law (linear for the first and third) evolution of minimum thickness with time to rupture, at rates given by various analytical results [40, 37].

On top of this already complex situation, thermal fluctuations can introduce yet another regime (here referred to as the F-regime), which generates non-linear (power-law) evolution of minimum thread radius. For moderate Th ($>\sim 0.1$) and non-negligible Oh, fluctuations appear to dominate the entire thread evolution (see, e.g., the non-linear evolution in Figure 5.8 (a)). However, at lower Th, we can observe transitions from the classical behaviour to one that is fluctuation dominated as the rupture process progresses.

In Figure 5.14 we compare the SLE with the classical model (LE) and various

71
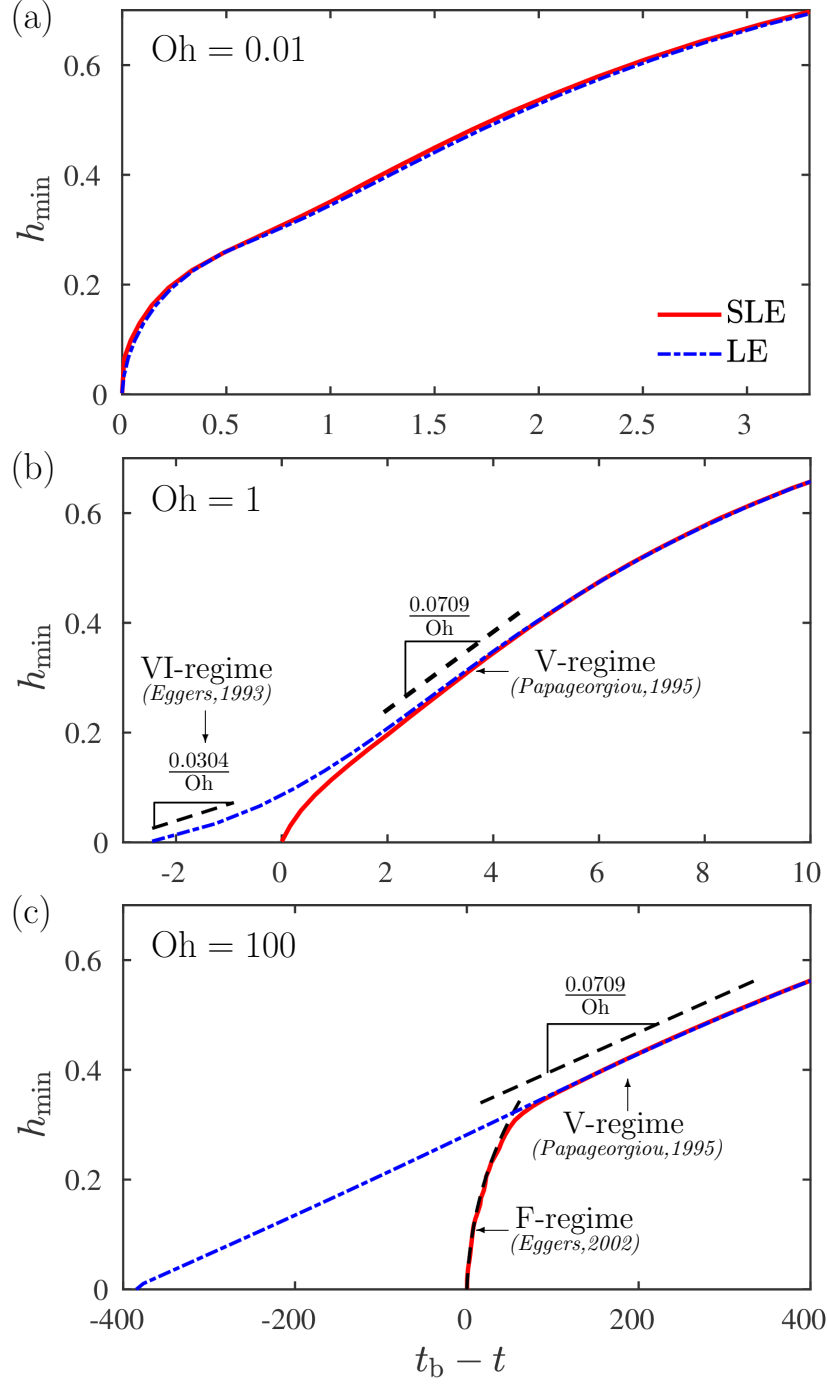
Figure 5.14: Time evolution of minimum thread radius, $h_{\min}$; a comparison between the LE (dashed and dotted lines) and SLE (solid lines) for Th=0.02 and Oh = (a) 0.01, (b)=1, and (c)=100. Note, t_{b} is the breakup time predicted by the SLE. Dashed lines represent similarity solutions in different dynamic regimes. Linear solutions in the VI-regime and V-regime come from Refs. [34] and [32], respectively. The power-law solution in the F-regime for (c) is obtained from Ref. [2].

analytical results for *fixed* Th = 0.02 at Oh = 0.01, 1 and 100. Experimentally, this corresponds to using fluids of a range of different viscosities (with fixed surface tensions) for the same breakup configuration. As was the case for the rupture profiles presented above, at low Oh (Figure 5.14 (a)) there is seemingly no impact of fluctuations on the time evolution of $h_{\min}$ (i.e. there is no discernible difference between the SLE and LE). For larger Oh (see Figure 5.14 (c)), however, a clear transition between macroscopic and a fluctuation-dominated regime can be observed. At early times the evolution is described by a linear time dependence, derived by Papageourgiou [32, 33] for the V-regime; at later times (in the F-regime) the evolution matches the power law proposed by Eggers [2] and greatly accelerates the breakup process. Of course, of the two numerical methods presented in the figure, only the SLE can capture both. When Oh = 1 (Figure 5.14 (b)), the dynamics become more complicated. The LE predicts a transition from the V-regime to the VI-regime in the final stages, which has been proved experimentally [40] and numerically [37] at macroscopic scales. However, this transition does not occur in the presence of thermal fluctuations, according to the SLE. Instead there exists a similar transition from the V-regime to a new regime as was the case for the large Oh case, but the power-law exponent does not match that found by Eggers (which, as explored in § 5.3.2, is possibly due to the assumption in his analytic treatment that surface tension is unimportant in the final stages leading to rupture).

Figure 5.15 shows more results of the transition from the V-regime to the 'fluctuation' regime, where the dashed lines are Papageorgiou's similarity solution for different Oh and solid lines represent the average solutions (from 50 realisations) for the SLE. These results indicate a bigger 'fluctuation' regime (larger crossover $h_{\min}$) with larger Oh, highlighting the important role of Oh on the fluctuation intensity. Furthermore, it would be interesting to explore whether there exists a scaling law between the height at which this transition occurs and Oh (or Th). However, we would need to get many decades of $h_{\min}$ to determine the precise crossover point, which is not available from our current simulations.

5.5   Summary

In this chapter, a numerical solver of the SLE has been developed with a new simple scheme proposed for the noise term. Based on validation from MD for both instability and the rupture of liquid nano-threads, this solver is demonstrated to be a powerful tool for studying the interface dynamics of nano-threads; and operating over a thousand times faster than MD. Furthermore, it allows us to operate in the regions of parameter space
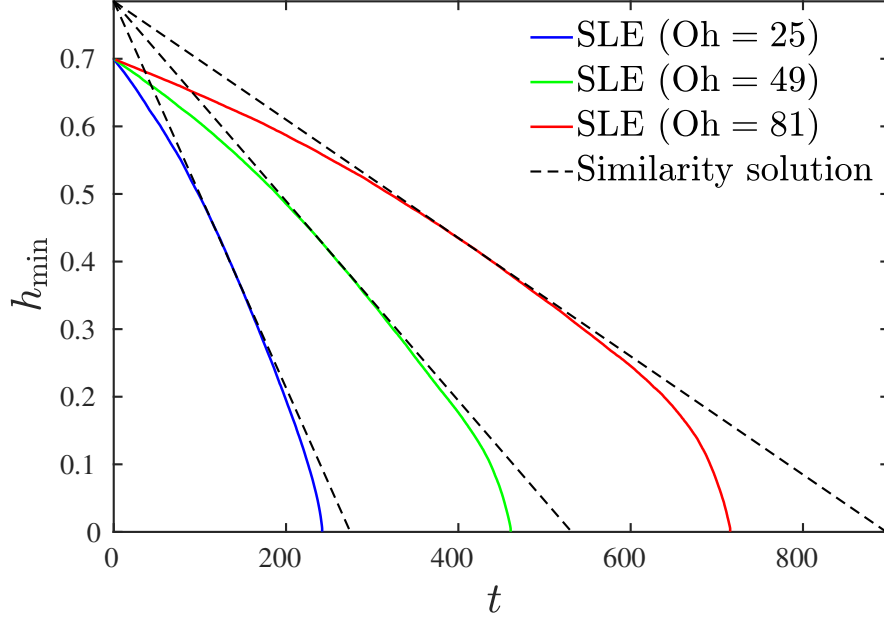
Figure 5.15: The temporal evolution of minimum thread radius for different Oh, with Th = 0.02. The similarity solution comes from the Ref. [33].

where analytic models are outside their limits of applicability and MD is impractical either due to (i) exorbitant computational cost or (ii) limits in the molecular properties available from known potentials.

While this chapter provides new understanding of interface dynamics, it opens up several new avenues of enquiry (i.e. the influence of the correlated lengths on dynamics, and new similarity solution containing both fluctuations and surface tension). Detailed future directions will be discussed in Chapter 7.

Chapter 6

Interface dynamics of bounded films at the nanoscale

As we have established and validated a reliable numerical framework for the SLE in Chapter 5, we can now expand this to other SPDEs to investigate different physics at the nanoscale. One scenario we consider is nano-film flows on substrates, which can be modelled by the STFE proposed in Chapter 3. In this Chapter, we will undertake detailed numerical studies for the STFE to explore different kinds of nano-film flows.

We organise the chapter in the following way. In Section 6.1, the Crank-Nicolson scheme is introduced as an implicit method for the STFE, where a simple iteration scheme is proposed in § 6.1.2 to achieve high efficiency. All the numerical solutions are validated against analytical results in Section 6.2. Then, this solver is used to explore two thin-film flows at the nanoscale:

(i) nano-droplet spreading, which we look at in Section 6.3,

(ii) nano-droplet coalescence, which we cover in in Section 6.4.

6.1 Numerics for the STFE

To construct the numerical framework, we start from the original STFE (with the substrate roughness $f = 0$ and the slip length $\beta = 0$). After rearranging Equation (3.52), the STFE can be written in the following format, with three terms on the right hand side (RHS), representing the surface tension, the disjoining pressure and the thermal

fluctuations, respectively,

$$\frac{\partial h}{\partial t} = -\frac{\gamma}{3\mu}\frac{\partial}{\partial x}\left(h^3\frac{\partial^3 h}{\partial x^3}\right) + \frac{1}{3\mu}\frac{\partial}{\partial x}\left(h^3\frac{\partial \Phi}{\partial x}\right) + \sqrt{\frac{2k_{\mathrm{B}}T}{3W\mu}}\frac{\partial}{\partial x}\left(h^{3/2}\mathcal{N}\right).\qquad(6.1)$$

When the calculation domain ($[0, L]$) is discretised with M uniform grid points, the solution can be defined by a vector, $\mathbf{H} = (h_1, h_2, ...h_M)^{\mathrm{T}}$. Using the well-known numerical technique of the method of lines [132], the discretised STFE can be presented as a system of coupled stochastic ODEs in time,

$$\frac{d\,\mathbf{H}}{dt} = \mathbf{T}(\mathbf{H}) + \mathbf{\Phi}(\mathbf{H}) + \mathbf{F}(\mathbf{H}),\qquad(6.2)$$

where $\mathbf{T}$, $\mathbf{\Phi}$ and $\mathbf{F}$ come from three terms on the RHS above (displayed in the same order). Note that Equation (6.2) is a stiff system due to the fourth-order derivatives in $\mathbf{T}$. Therefore, the explicit scheme that worked successfully in Chapter 5 would here be inefficient. Instead, pursuing reliable implicit methods is necessary for the STFE. In the following subsections, we will give the details of the algorithm.

6.1.1 Crank-Nicolson scheme

The Crank-Nicolson scheme was proposed in the mid 20th century [133], initially for numerically solving the heat equation and similar PDEs with second-order accuracy in time. Since this implicit method has been shown unconditionally stable for diffusion equations (or other similar PDEs) [133], it can be applied here to overcome the stiffness of the STFE. The first successful application was carried out by Diez & Kondic [134] for the deterministic thin-film equation (TFE) in 2002. Later, it was expanded to the STFE to explore the thin-film instability [83, 84] and droplet spreading [88] at small scales.

In this work, we employ this widely-used Crank-Nicolson scheme and rewrite it in a matrix expression, shown below,

$$\frac{\mathbf{H}^{n+1} - \mathbf{H}^n}{\triangle t^n} = \theta\,\mathbf{T}^{n+1} + (1-\theta)\,\mathbf{T}^n + \mathbf{\Phi}^n + \mathbf{F}^n.\qquad(6.3)$$

Here, the superscript n denotes the number of the time step. $\triangle t^n = t^{n+1} - t^n$. $\mathbf{T}^{n+1}$ represents the surface tension term at the next step, t^{n+1}, while $\mathbf{T}^n$ is at the current step, t^n. Notably, only $\mathbf{T}$ is treated implicitly because of its high (fourth) derivative order, while $\mathbf{\Phi}$ and $\mathbf{F}$ are dealt with explicitly. Despite this specific treatment, good predictions can be achieved based on this framework, and no precision loss of the solution has been

found in previous work [83, 84].

The symbol, θ in Equation (6.3) is a numerical parameter to determine the scheme options. Three typical values of θ and their corresponding schemes are listed in Table 6.1. In this work, we employ the Crank-Nicholson scheme as the implicit option, with $\theta = 1/2$.

Table 6.1: Numerical scheme options

θ	type	name
0	explicit	forward Euler scheme
1	implicit	backward Euler scheme
1/2	implicit	Crank-Nicholson scheme

The explicit scheme ($\theta = 0$) is also tested in §6.2.1 to provide results for the efficiency comparison between different schemes.

The surface tension term can expressed as a product of a diffusion matrix and the solution, namely, $\mathbf{T} = \mathbf{A} \cdot \mathbf{H}$, proposed by Diez & Kondic [134]. Therefore, Equation (6.3) becomes

$$\frac{\mathbf{H}^{n+1} - \mathbf{H}^n}{\triangle t^n} = \theta \, \mathbf{A}^{n+1} \cdot \mathbf{H}^{n+1} + (1 - \theta) \, \mathbf{A}^n \cdot \mathbf{H}^n + \mathbf{\Phi}^n + \mathbf{F}^n \,. \tag{6.4}$$

The explicit expression for $\mathbf{A}$ is given in Appendix F, which comes from [134] with the positivity-preserving property enforced. Because $\mathbf{A}$ is the nonlinear matrix depending on the solution at the next time step (h_i^{n+1}), our problem now is working out how to integrate Equation (6.4). To solve this problem, an iteration method is required.

6.1.2 Iteration scheme

The best known iteration scheme is the Newton-Kantorovich method [135], with a function, G, defined first:

$$\mathbf{G} = \left(\mathbf{I} - \theta \triangle t \mathbf{A}^{n+1}\right) \cdot \mathbf{H}^{n+1} - [\mathbf{I} + (1 - \theta)\triangle t \mathbf{A}^n] \cdot \mathbf{H}^n - (\mathbf{\Phi}^n + \mathbf{F}^n) \triangle t \,, \tag{6.5}$$

where $\mathbf{G}(h_i^{n+1})$ is equal to zero when h_i^{n+1} is the exact solution at t^{n+1} for Equation (6.4). However, the final solution is unknown. Therefore, we guess an initial value of the solution, h_i^g, then evaluate how far it is from the actual solution. A correction, q_i is introduced here to give $\mathbf{G}(h_i^g + q_i) = 0$, which can be approximated by a linear expansion, expressed as

$$\mathbf{G}(h_i^g + q_i) \approx \mathbf{G}(h_i^g) + \frac{\partial \mathbf{G}}{\partial h_i^g} q_i = 0 \,. \tag{6.6}$$

Since all the variables at time step, $n + 1$ (i.e., $\mathbf{H}^n$, $\mathbf{A}^n$, $\boldsymbol{\Phi}^n$ and $\mathbf{F}^n$) are independent of h_i^g, the derivative of $\mathbf{G}(h_i^g)$ is

$$
\begin{aligned}
\frac{\partial \mathbf{G}}{\partial h_i^g} &= \frac{\partial \left(\mathbf{H} - \theta \triangle t \mathbf{T} \right)}{\partial h_i^g} \\
&= \mathbf{I} - \theta \triangle t \frac{\partial \mathbf{T}}{\partial h_i^g} \\
&= \mathbf{I} - \theta \triangle t \mathbf{J} \,,
\end{aligned}
\tag{6.7}
$$

where the $\mathbf{J}$ is the Jacobian matrix, whose detailed expressions are presented in Appendix F. Combining Equation (6.6) and (6.7) yields an algebraic coupled system of equations where q_i are the only unknown variables:

$$
[\mathbf{I} - \theta \triangle t \mathbf{J}(h_i^g)] \cdot \mathbf{q} = -\mathbf{G}(h_i^g) \,.
\tag{6.8}
$$

When Equation (6.8) is solved to give a 'new' q_i, we expect to move closer to the real solution. Then, we update our guess as $h_i^g = h_i^g + q_i$ and repeat the process. If the iteration converges, G will decrease, eventually to zero.

However, convergence cannot always be guaranteed with the Newton-Kantorovich method, especially when h_i^g causes the iteration to go in an incorrect direction. Even if h_i^g is simply 'not good enough', the process can be fairly inefficient, with more than hundreds of iteration steps to reach the converged h_i^{n+1}. Therefore, we propose another simple new iteration method to improve the numerical performance, whose basic framework is expressed as:

$$
\left(\mathbf{I} - \theta \triangle t \mathbf{A}^{n+1} \right) \cdot \mathbf{H}^{n+1} = [\mathbf{I} + (1 - \theta) \triangle t \mathbf{A}^n] \cdot \mathbf{H}^n - (\boldsymbol{\Phi}^n + \mathbf{F}^n) \triangle t \,.
\tag{6.9}
$$

Since the diffusion matrix, $\mathbf{A}^{n+1}$ depends on the unknown solution, h_i^{n+1}, the guess value, h_i^g is substituted into $\mathbf{A}$ directly. So the solution can be obtained via

$$
\mathbf{H}^{n+1} = [\mathbf{I} - \theta \triangle t \mathbf{A}(h_i^g)]^{-1} \cdot \{ [\mathbf{I} + (1 - \theta) \triangle t \mathbf{A}^n] \cdot \mathbf{H}^n - (\boldsymbol{\Phi}^n + \mathbf{F}^n) \triangle t \} \,.
\tag{6.10}
$$

This process is then repeated with h_i^g updated by the solutions at each iteration step until the deviation, $q_i = |h_i^{n+1} - h_i^g|$ is close to zero. Although there is no strict mathematical demonstration for the convergence improvement, we have achieved better performance in our numerical tests with this new scheme, and have shown it to be much more efficient than the Newton-Kantorovich method. In the tests, the initial guess value is set as the solution at the previous time step, i.e., $h_i^g = h_i^n$. Having established the basic iteration

frame, a robust tool to solve Equation (6.10) is now needed. Since $(\mathbf{I} - \theta\triangle t\mathbf{A})$ is a pentadiagonal matrix, an optimized Gauss method is used here to obtain the solution, h_i, at every corresponding time step efficiently.

One problem we have left is the numerical errors in temporal discretisation when $\triangle t$ is too large. According to the linear approximation, the error can be decided by the second-order derivative in the Taylor expansion [136]:

$$e_i = \frac{(\triangle t^n)^2}{h_i^n} \frac{d^2 h_i^n}{dt^2} , \qquad (6.11)$$

whose discretised expression is

$$e_i = \frac{(\triangle t^n)^2}{h_i^{n-1}} \frac{\triangle t^{n-1} h_i^{n+1} + \triangle t^n h_i^{n-1} + (\triangle t^{n-1} + \triangle t^n) h_i^n}{(\triangle t^{n-1} + \triangle t^n) h_i^n} . \qquad (6.12)$$

Usually, the errors at different nodes have different values. So, we check the maximum value of the errors $(max(|e_i|))$ and set small values (e.g., 10^{-2} or 10^{-3}) as the upper limit for $max(|e_i|)$ to achieve good precision.

In summary, the iterative process requires the following checks:

- The new solution is not negative at any point, i.e., $h_i > 0$.
- The time derivative error e_i has to be smaller than the upper limit, i.e., $max(|e_i|) < 10^{-3}$.
- The iteration process converges, i.e. $|q_i|$ decreases monotonically to $|10^{-4} h_i|$.
- The number of iteration steps is smaller than 100.

If any condition is not satisfied, we go back to the initial value $(h_i^g = h_i^n)$ and restart the iteration process with a smaller time step that is half of the previous one, $\triangle t^n = \triangle t^n/2$. Notably, since new random variables are introduced at each time step for the STFE, the error in the temporal derivative is expected to be much larger than that of the (deterministic) TFE, which would significantly increase the computational costs with a smaller time step.

6.2   Numerical verifications

Here, we will verify the numerical frame with the analytical models for

(i) deterministic cases (modelled by the TFE) in § 6.2.1,

(ii) stochastic cases (modelled by the STFE) in § 6.2.2.

6.2.1 Deterministic cases

In this section, we test two deterministic cases in the TFE framework. The first is the perturbation dissipation of the thin-film flows due to surface tension, which can be modeled by Equation (6.2) with only the surface tension term ($\mathbf{\Phi} = 0$ and $\mathbf{F} = 0$) on the RHS. The solutions are plotted in the Figure 6.1(a), where a sinusoidal perturbation is
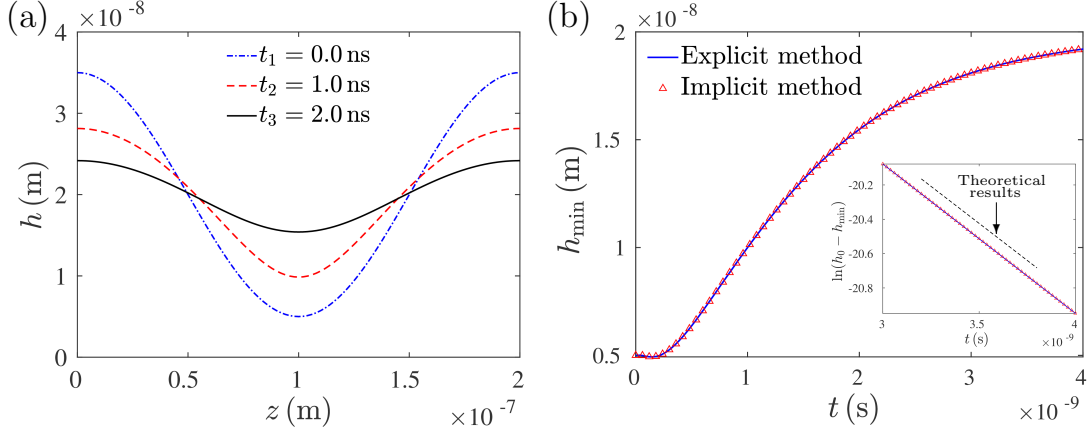
Figure 6.1: Perturbation dissipation of thin-film flows. (a) Interface profiles at different time instants. (b) Minimum film height against time, where the blue solid lines and triangle dots are the results of the explicit method ($\theta = 0$) and implicit method ($\theta = 1/2$), respectively. The black dashed line comes from Equation (6.14).

set to a thin-film with $h_0 = 20 \, \text{nm}$ and $L = 10 h_0$ (see the blue dash-dotted line). We can see a clear perturbation dissipation as time goes by with the increase of $h_{\min}$ against time, as shown in Figure 6.1(b).

To verify the numerical results further, we carry out linear instability analyses (similar to the approach in §4.1.2 for the jet flows) with $h(x,t) = h_0(1 + \varepsilon e^{\omega t + ikx})$. Substituting this into the TFE gives

$$h_0 \varepsilon \omega e^{\omega t + ikx} = -\frac{\gamma}{3\mu} h_0^4 \varepsilon (ik)^4 e^{\omega t + ikx} \,. \tag{6.13}$$

Therefore, we can obtain the expression for the growth rate of the perturbation:

$$\omega = -\frac{\gamma h_0^3 k^4}{3\mu} \,. \tag{6.14}$$

Here, $\mu = 1.64 \times 10^{-4}$ and $\gamma = 5.46 \times 10^{-2}$. In this case, since there is only one wave, the wavenumber can be calculated directly from the film length, i.e., $k = 2\pi/L$. Notably, $\omega <$

0 means that surface tension always dissipates perturbations in the instability. This is the main difference from the RP instability in Section 4.1, where surface tension plays roles as both driving and dissipating forces with two curvatures. Equation (6.14) is plotted as the benchmark (see the black dashed line) in the subset of Figure 6.1(b), in which our numerical solutions match this analytical model very well, providing further verification. In addition, we apply both the explicit method (forward Euler scheme) and the implicit method (Crank-Nicholson scheme) for the solutions. Very close agreement between these two methods can be seen in Figure 6.1(b). In the next case, more comparisons between the methods will be shown.
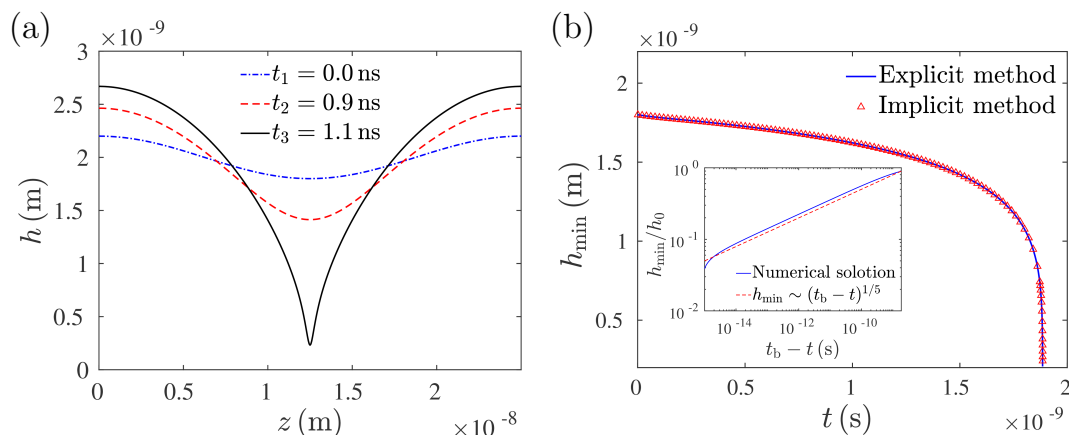
Figure 6.2: Thin-film rupture dynamics. (a) Interface profiles at different time instants. (b) Minimum film height against time, where the blue solid lines and triangle dots are the results of the explicit method ($\theta = 0$) and implicit method ($\theta = 1/2$), respectively. The red dashed line comes from the similarity solutions in [52].

Despite the stabilising influence of the surface tension, the bounded film could rupture (become unstable) because of the van der Waals forces, as found in the experiments with the polymer-liquid [58]. This phenomenon has been successfully described by the TFE [58, 80] with a similarity solution derived (i.e., $h_{min}(t) \sim (t_b - t)^{1/5}$) [52], which is used as the benchmark in our second test. The van der Waals forces are modelled by the disjoining pressure in Equation (6.1), expressed as $\phi = H_a/(2\pi h^3)$, where H_a represents the Hamaker constant [137], reflecting the strength of the various intermolecular attractions. In the simulation, $H_a = 2 \times 10^{-19}$ J. The liquid property (μ and γ) is the same as those of the first case.

The interface profiles of the film are illustrated in Figure 6.2(a) with a sinusoidal initial perturbation (the blue dash-dotted line). Due to the influence of the disjoining pressure, the perturbation increases with time, with a 'spike' profile at the final stage

(see the black solid line). Figure 6.2(b) shows the time evolution of the minimum film height, $h_{\min}(t)$, where the numerical solution matches the similarity solution proposed by Zhang & Lister [52] fairly well in the subset, providing further verification.
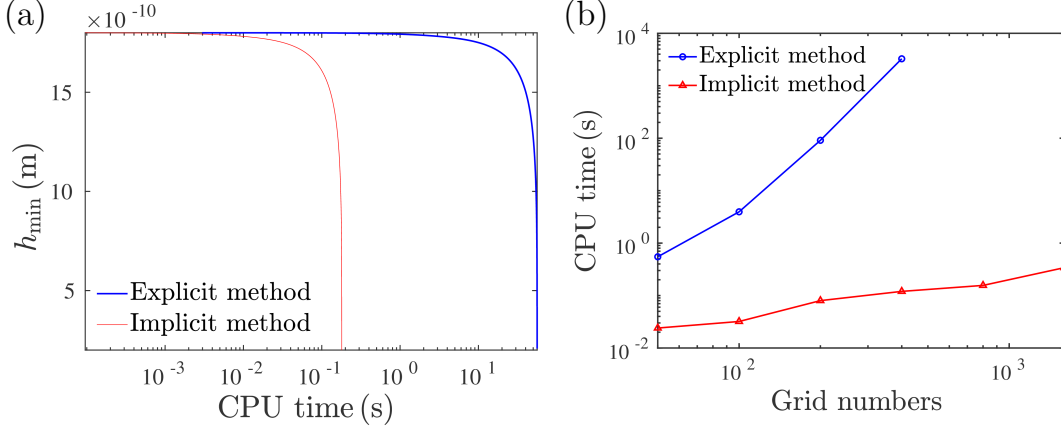
Figure 6.3: Efficiency comparison between two numerical methods. (a) Minimum film height against the CPU time (core-second). Here, the same grid number (200) is used by both the methods. (b) Simulation CPU time at different grid numbers. The whole time is evaluated from the beginning (the initial profile) to the rupture time $(h_{\min} < 10^{-2}h_0)$, obtained with the adaptive time-step method started from a large initial $\triangle t$.

Note that both explicit and implicit methods are employed in this case, where good agreement is obtained in $h_{\min}(t)$. To compare their efficiencies, the adaptive time-step method, introduced in § 6.1.2, is used here to achieve the fastest simulation speed with different grid numbers for each method. The CPU time evolution of $h_{\min}$ with 200 grid nodes is presented in Figure 6.3(a), where the implicit method is found to be around three orders of magnitude faster than the explicit one. Figure 6.3(b) shows the statistics of the time of the entire dynamics process (from the initial profile to the rupture) with different grid numbers. Here, we can see obvious advantages to the implicit method, and efficiency can be improved by five more orders of magnitude with dense grids (where node number is larger than 1000).

6.2.2 Stochastic case

Similar to the verifications in § 5.3.1, the TCW theory is employed here to validate the numerical solutions for the STFE. One realisation is illustrated in Figure 6.4, where perturbations, driven by thermal fluctuations, grow against time despite the dissipation effect due to the surface tension. As a consequence, significant capillary waves are

generated due to the fluctuations in the final solutions (see the dotted black lines), which should coincide with the TCW theories.
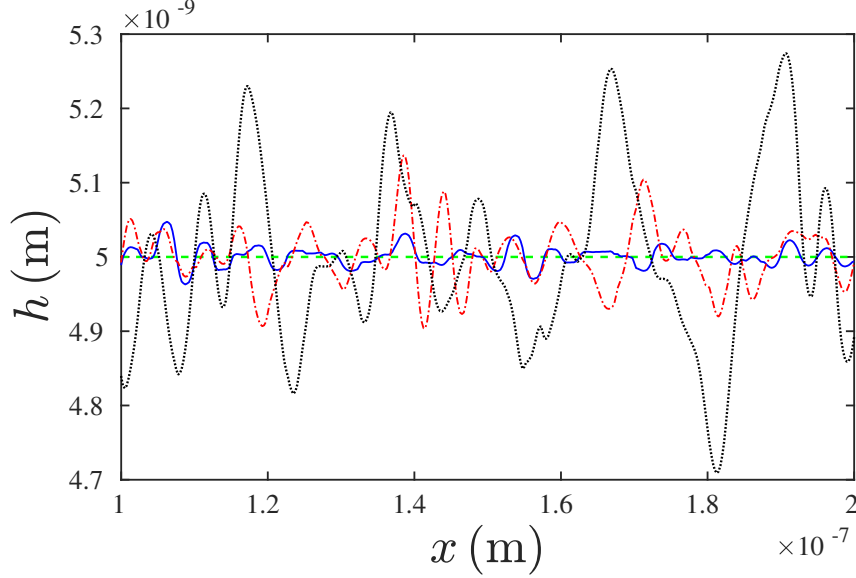
Figure 6.4: Interface profiles of a bounded film with $h_0 = 5\,\text{nm}$ and $W = 2\,\text{nm}$ at 4 time instants, i.e., $t_1 = 0.0\,\text{fs}$ (green line), $t_2 = 10.0\,\text{fs}$ (blue line), $t_3 = 0.190\,\text{ps}$ (red line), $t_4 = 3.99\,\text{ps}$ (black line).

The lastest theoretical framework for the TCW is presented by Zhang et al [82] including the TCW dynamics at different time instants, expressed as

$$|H|_{\text{rms}} = \sqrt{\overline{|H_{\text{det}}|^2} + \overline{|H_{\text{fluc}}|^2}}, \tag{6.15}$$

$$\begin{cases} \overline{|H_{\text{det}}|^2} = |H_{\text{i}}|^2 e^{2\omega t}, \\ \overline{|H_{\text{fluc}}|^2} = \frac{k_{\text{B}} T h_0^3 k^2}{3\mu\omega} \frac{L}{W} \left(e^{2\omega t} - 1 \right), \end{cases}$$

where H_{rms} is the mean square roots of the film interface, representing the wave spectrum and H_{i} is the initial model disturbance. The growth rate, ω was found to depend on the wavenumber, k, i.e.,

$$\omega(k) = -\frac{\gamma h_0^3 k^4}{3\mu} + \frac{\text{H}_{\text{a}} k^2}{2\pi\mu h_0}. \tag{6.16}$$

To simplify the problem, we neglect the disjoining pressure term ($\text{H}_{\text{a}} = 0$) and set a perfectly smooth initial condition without any perturbations ($H_{\text{i}} = 0$). So Equation (6.15) becomes

$$|H|_{\text{rms}} = \sqrt{\frac{k_{\text{B}} T h_0^3 k^2}{3\mu\omega} \frac{L}{W} \left[e^{-(2\gamma h_0^3 k^4 t)/(3\mu)} - 1 \right]}, \tag{6.17}$$

83
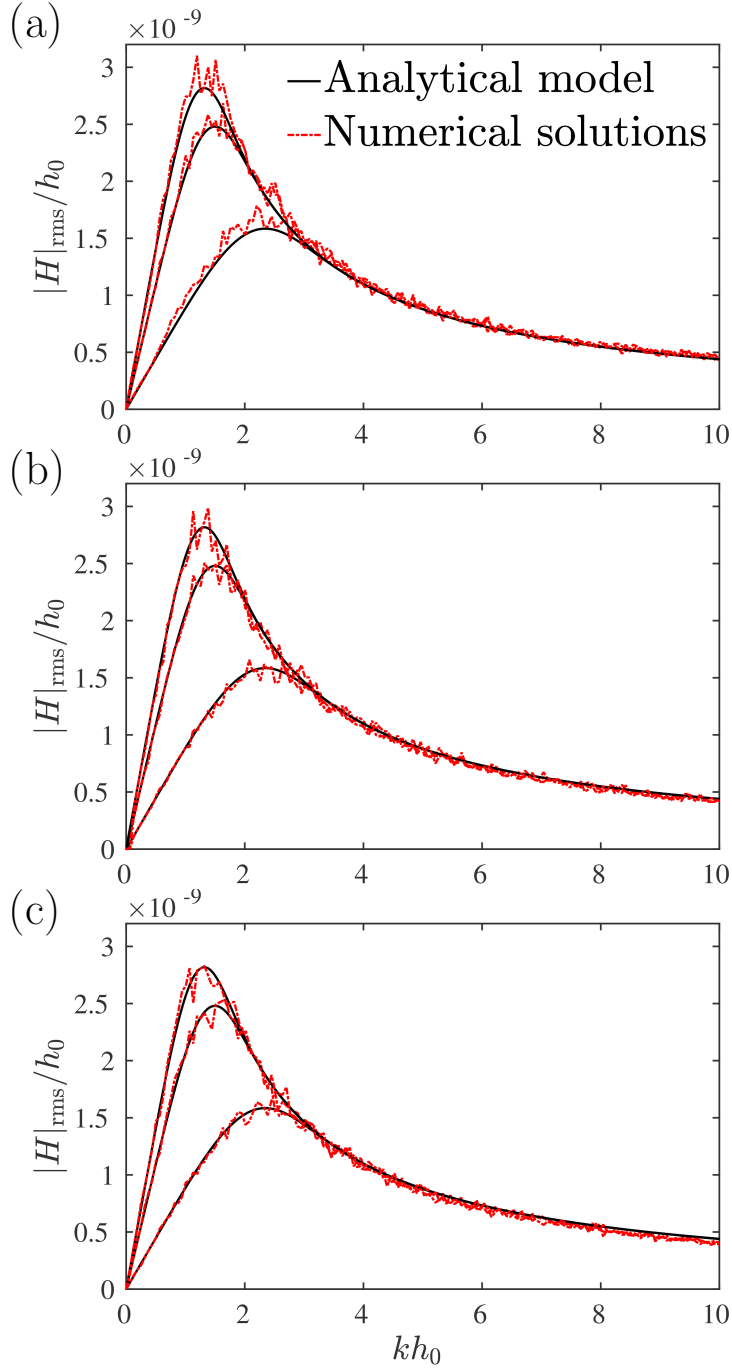
Figure 6.5: The r.m.s. of disturbance amplitude versus wavenumber three time instants, i.e., $t_1 = 5.00\,\text{ps}$, $t_2 = 30.0\,\text{ps}$ and $t_3 = 50.0\,\text{ps}$; a comparison of ensemble-averaged SLE simulations (dashed lines) and analytical result (solid lines). (a) white noise with $\triangle z = 0.5\,\text{nm}$; (b) interpolated noise with $\triangle z = 0.1\,\text{nm}$; (c) Grun's noise model with $\triangle z = 0.1\,\text{nm}$. For the correlated noise model, $L_c = 0.5\,\text{nm}$.

which is used as the benchmark for the numerical solutions here.

To match the analytical model in Equation (6.17), 50 independent simulations (or realisations) are performed with an initial film height of $h_0 = 5\,\text{nm}$ and a film length of $L = 500\,\text{nm}$. The properties of the liquid argon in [82] are employed here with $\mu = 2.44 \times 10^{-4}\,\text{kg}\,\text{m}^{-1}\,\text{s}^{-1}$ and $\gamma = 1.52 \times 10^{-2}\,\text{N}\,\text{m}^{-1}$. For the fluctuation term, temperature T is set as $84.01\,\text{K}$ and the film width (z-coordinate), $W = 2\,\text{nm}$. Similar to the approach in §5.3.1, a discrete Fourier transform of the interface position is applied for each realisation to get the PSD, and then an ensemble average at each time instant allow us to produce the results (red dashed lines) in Figure (6.5), whereas the black solid lines come from Equation (6.17).

Since SLE studies in Chapter 5 denote that uncorrelated (white) noise leads to the grid-size/time-step unconvergence, the two correlated noise models introduced in Chapter 5 are used here with finer grids to give the results in Fig 6.5(b) and (c). We can see good agreement between the numerical results and the analytical model at each time instant no matter which noise model is chosen, giving us confidence that our STFE solver is sufficiently reliable to be applied to explore the physics of the thin-film flows at the nanoscale.

6.3 Droplet spreading

In this section, we carry out numerical studies of droplet spreading on different substrates with the STFE solver developed in this chapter. Usually, the macroscopic spreading is considered to be driven by surface tension, while extra effects (e.g. van der Waals forces or thermal fluctuations) need to be taken into account at the nanoscale. When the substrate is completely wettable (zero contact angle), the influence of disjoining pressure can be neglected due to the balance between the attractive and repulsive contributions of the van der Waals forces [90]. Note that the zero disjoining pressure is just an assumption to simplify the problem, while on fully wettable substrates in the real physical world, there may exist other complicated intermolecular forces, leading to a negative disjoining pressure term. With this assumption, the remaining microscopic factor, the thermal fluctuations, becomes the main concern in this section.

6.3.1 Scaling derivation

In order to model the spreading at the nanoscale, first we non-dimensionalise the STFE ($\phi = 0$) with the rescaling variables shown below:

$$\tilde{h} = h/h_0, \qquad \tilde{t} = t/(3\mu h_0/\gamma).$$

So the non-dimensional version of the STFE is:

$$\frac{\partial \tilde{h}}{\partial \tilde{t}} = -\frac{\partial}{\partial \tilde{x}} \left(\tilde{h}^3 \frac{\partial^3 \tilde{h}}{\partial \tilde{x}^3} \right) + \sqrt{2\varphi} \frac{\partial}{\partial \tilde{x}} \left(\tilde{h}^{3/2} \tilde{\mathcal{N}} \right), \tag{6.18}$$

where $\varphi = k_{\mathrm{B}} T / (\gamma W h_0)$, represents the noise intensity.

It is well known that the spreading characteristics can be predicted by a power-law scaling of a characteristic lateral scale, i.e., $\tilde{\ell} \sim \tilde{t}^n$ [89]. Here, we use the average second moment of $\tilde{h}$ to estimate $\tilde{\ell}$, first used by Davidovitch et al. [88],

$$\tilde{\ell}(t) = \left\langle \left[\frac{1}{\tilde{V}} \int (\tilde{x} - \tilde{X})^2 \tilde{h}(x, t) d\tilde{x} \right] \right\rangle, \tag{6.19}$$

where $\tilde{V} = \int \tilde{h} d\tilde{x}$ is the constant volume of the droplet, $\tilde{X} = \left(\int \tilde{x} \tilde{h} d\tilde{x} \right) / \tilde{V}$ is the instantaneous position of the droplet center, and $\langle \ldots \rangle$ represents the ensemble average of all the realisations.

In order to decide the power law (n), a similarity transform is made with the change of variables, proposed by Nesic [136]:

$$\tilde{x} = b\breve{x}, \qquad \tilde{h} = b^\alpha \breve{h}, \qquad \tilde{t} = b^\eta \breve{t}, \tag{6.20}$$

where b is an arbitrary factor, and α and η are constants that remain to be fixed. The symbol '$\breve{}$' means 'transformed' variables. According to the scaling relation above ($\breve{x} \sim \breve{h} \sim \breve{t} \sim O(1)$), we can easily obtain $\tilde{\ell} \sim \tilde{x} \sim \tilde{t}^{1/\eta}$, namely, the power law is equal to $1/\eta$. For the value of η, we substitute the transform relations above into the non-dimensional STFE (Equation (6.18)) and obtain

$$\frac{\partial \breve{h}}{\partial \breve{t}} = - \left(b^{3\alpha + \eta - 4} \right) \partial_{\breve{x}} \left(\breve{h}^3 \partial_{\breve{x}}^3 \breve{h} \right) + \left[b^{(\alpha + \eta - 3)/2} \right] \sqrt{2\varphi} \partial_{\breve{x}} \left[\breve{h}^{3/2} \breve{\mathcal{N}}(\breve{x}, \breve{t}) \right]. \tag{6.21}$$

Note that, on the RHS, there are two independent force terms:

(i) the deterministic term due to the surface tension,

(ii) the stochastic term due to the thermal fluctuations,

as well as the arbitrary scaling factor b, where the scaling powers should always be zero to hold the 'similarity' of the transform, namely,

$$
\begin{cases}
3\alpha + \eta - 4 = 0\,, & \text{for the deterministic term,} \\
\alpha + \eta - 3 = 0\,, & \text{for the stochastic term.}
\end{cases}
\tag{6.22}
$$

In addition, no matter which force drives the spreading, the droplet volume,

$$
\tilde{V} = \int \tilde{h}\,d\tilde{x} = b^{\alpha+1} \int \breve{h}\,d\breve{x}\,.
$$

should always be conserved, requiring $\alpha = -1$. So, we can obtain the value of the left coefficient η from Equation (6.26), i.e., $\eta = 7$ in the surface tension term; and $\eta = 4$ in the stochastic term, implying two power-law spreading regimes:

$$
\begin{cases}
\tilde{\ell} \sim \tilde{t}^{\,1/7}, & \text{Tanner's law,} \\
\tilde{\ell} \sim \tilde{t}^{\,1/4}, & \text{Stochastic spreading.}
\end{cases}
\tag{6.23}
$$

These have been proposed by Tanner [89] and Davidovitch et al. [88], respectively. In addition, the larger power law (1/4) in the stochastic regime denotes that the spreading at the nanoscale is enhanced by the thermal fluctuations.

However, the conclusions above are only valid for the spreading on the fully wettable substrate with the no-slip boundary condition, which is not always the case at the nanoscale. Here, we use the STFE with the slip boundary condition (derived in the §3.2.3) to explore how the slip affects the spreading behaviours. With similar rescaling variables, the STFE with slip (see Equation (3.59) is written in the non-dimensional version

$$
\frac{\partial \tilde{h}}{\partial \tilde{t}} = -\frac{\partial}{\partial \tilde{x}}\left[\left(\tilde{h}^3 + 3\tilde{\beta}\tilde{h}^2\right)\frac{\partial^3 \tilde{h}}{\partial \tilde{x}^3}\right] + \sqrt{2\varphi}\frac{\partial}{\partial \tilde{x}}\left[\left(\tilde{h}^3 + 3\tilde{\beta}\tilde{h}^2\right)^{1/2}\tilde{\mathcal{N}}\right]\,,
\tag{6.24}
$$

where $\tilde{\beta}$ is the non-dimensional slip length. If $\tilde{\beta} \gg \tilde{h}$, the transformed Equation (6.24) (with scaling variables in Equation (6.20)) is

$$
\frac{\partial \breve{h}}{\partial \breve{t}} = -\left(b^{2\alpha+\eta-4}\right)\partial_{\breve{x}}\left(3\tilde{\beta}\breve{h}^2\partial_{\breve{x}}^3\breve{h}\right) + b^{(\eta-3)/2}\sqrt{2\varphi}\,\partial_{\breve{x}}\left[\sqrt{3\tilde{\beta}\breve{h}^2}\breve{\mathcal{N}}(\breve{x},\breve{t})\right]\,.
\tag{6.25}
$$

By the same approach, we get

$$
\begin{cases}
2\alpha + \eta - 4 = 0, & \text{for the deterministic term,} \\
\eta - 3 = 0, & \text{for the stochastic term,}
\end{cases}
\tag{6.26}
$$

where α is still equal to -1. Therefore, we can obtain a 'slip-modified' power law for the spreading:

$$
\begin{cases}
\tilde{\ell} \sim \tilde{t}^{1/6}, & \text{Slip} - \text{modified Tanner's law,} \\
\tilde{\ell} \sim \tilde{t}^{1/3}, & \text{Slip} - \text{modified stochastic spreading.}
\end{cases}
\tag{6.27}
$$

Note that the power law with the slip effect is larger than those obtained with the no-slip boundary condition, resulting in a faster spreading on substrates with slip. Further numerical validation will be shown in the following subsection.

6.3.2 Numerical results of the spreading
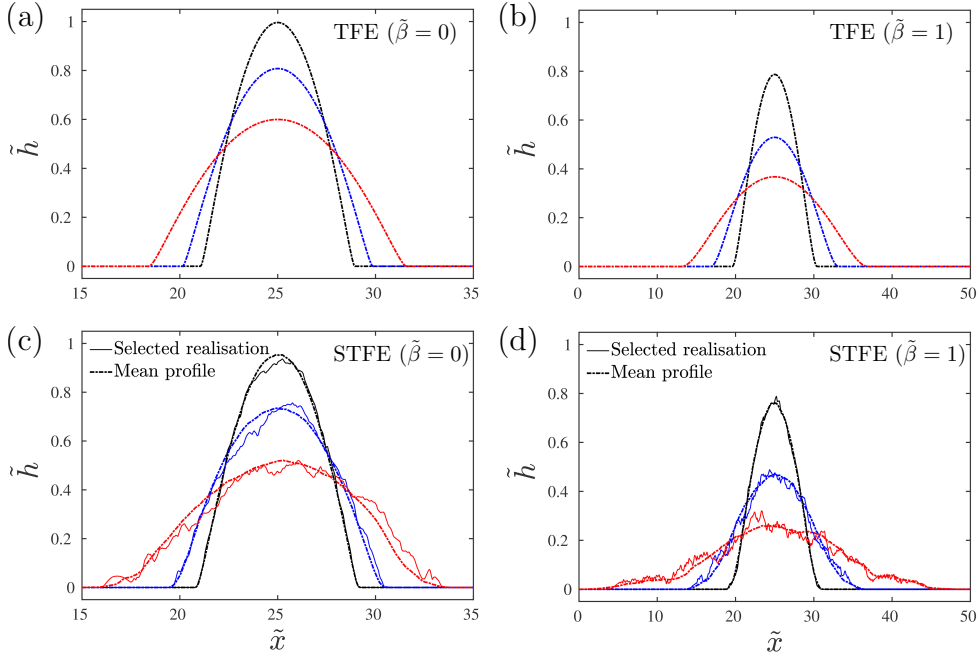
Figure 6.6: Spreading profiles at three time instants, i.e., $\tilde{t}_1 = 10$ (black lines), $\tilde{t}_2 = 10^2$ (blue lines) and $\tilde{t}_3 = 10^3$ (red lines) with the no-slip boundary (a)(c) and the slip boundary (b)(d). The deterministic cases are shown in (a) and (b), while the stochastic cases are shown in (c) and (d) with $\varphi = 10^{-3}$, where the solid lines represents one selected realisation. The dash-dotted lines are the average from 50 realisations.

To demonstrate the scaling law in the previous section, both deterministic and stochastic cases are solved numerically here with $\triangle z = 0.01$ and $L_c = 0.05$. As long-time realisations are required, the initial time step is set to be quite large, $\triangle t = 10^{-3}$, with the adaptive implicit method. In addition to the initial droplet profiles (modelled by a sinusoidal function), a precursor film is set over the whole domain. This approach is widely used in solving STFE numerically for different kinds of thin-film flows [78, 84, 85, 88] and designed not only for the numerical convenience but also to circumvent the contact line dynamics, where complicated boundary conditions are needed. As the film height is extremely small ($h^* = 10^{-2}h_0$), the fluctuations on it are set as zero, i.e. $\varphi_i = 0$. When the droplet spreads to a precursor-film node and 'pulls up' it, namely, $h_i > h^*$, the fluctuations on this node are activated.
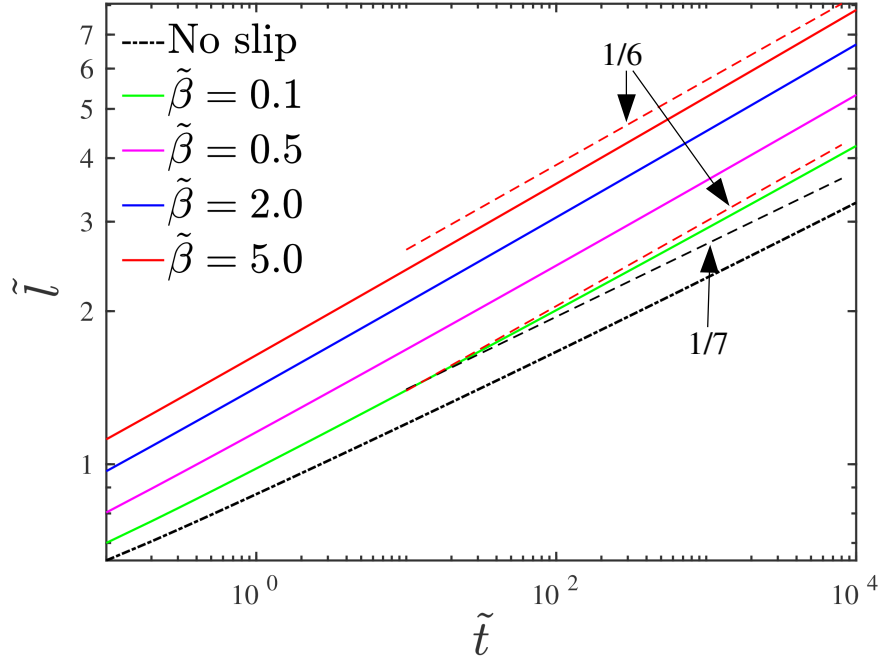
Figure 6.7: Deterministic characteristic lateral scales with different slip lengths, the dashed-dotted line is the numerical solution for the TFE with $\tilde{\beta} = 0$. Other solid lines (in different colours) are the numerical solutions for the TFE with different slip lengths. The dashed lines are the similarity solutions from Tanner's Law (Equation (6.23)) and the slip-modified law (Equation (6.27)).

Figure 6.6 shows the droplet profiles at different time steps, where the stochastic profiles are the average of the 50 independent realisations with $\varphi = 10^{-3}$. Note that the

initial spreading is much 'faster' than that at the later stage ($\tilde{t}_3 - \tilde{t}_2$ is much larger than $\tilde{t}_2 - \tilde{t}_1$) due to the initial stronger capillary forces (from the larger curvatures), while at the later stage the thermal fluctuations play a significant role and accelerate the process (see the comparison between upper and lower figures). In addition, the spreading is enhanced by the slip effects at any stage by comparing the figures on left and right. These findings coincide with the similarity solutions in §6.3.1 qualitatively.

To get a further quantitative comparison, $\tilde{\ell}$ is extracted based on Equation (6.19). Figure 6.7 illustrates the deterministic droplet widths with different slip lengths, where $\tilde{\ell}$ is found to increase significantly faster against $\tilde{t}$ with a larger $\tilde{\beta}$, showing an enhanced spreading with the slip effects. Moreover, spreading with the no-slip boundary (black dash-dotted line) and the large slip boundary (red solid line) obey the (slip-modified) Tanner's law presented in the previous section very well. In the crossover with a 'weak' slip effect ($\tilde{\beta} = 0.1$), we can see a transfer from the Tanner's law ($\tilde{\ell} \sim \tilde{t}^{1/7}$) to the the slip-modified law ($\tilde{\ell} \sim \tilde{t}^{1/6}$), denoting that even a 'tiny' slip effect would become more significant at the later stages of spreading due to the smaller $\tilde{h}$.
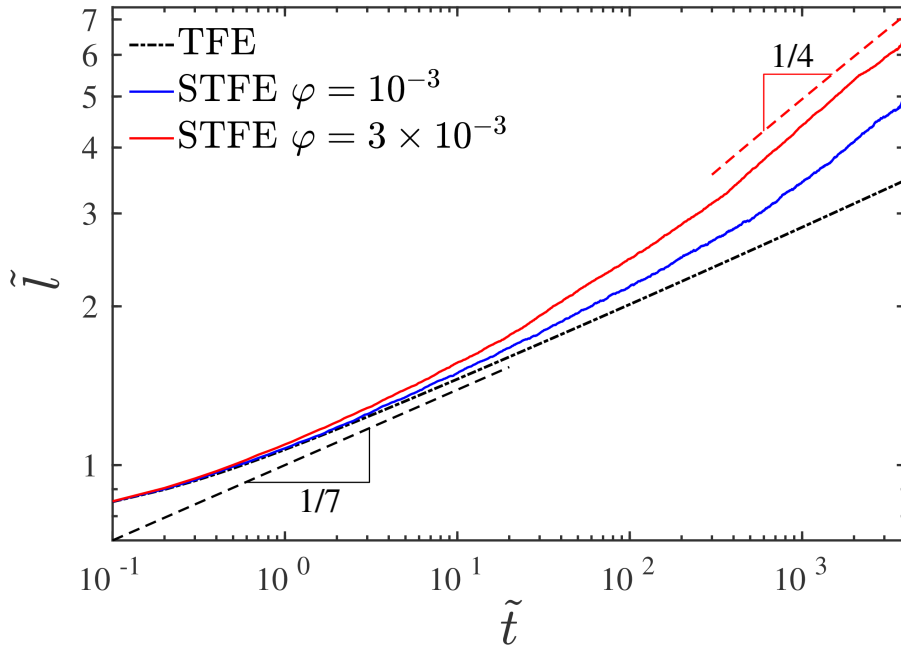
Figure 6.8: characteristic lateral scales with no-slip boundary conditions. Dash-dotted line is the result of the deterministic droplet. Solid lines are the average $\tilde{l}$ from 50 realisations with different fluctuation intensities, i.e., $\varphi = 10^{-3}$ in blue and $\varphi = 10^{-3}$ in red. Dashed lines represent the similarity solutions in Equation (6.23).

90

A similar behaviour also exists in the influence of thermal fluctuations. Usually, the stochastic power laws can be found after several decades (see Figure 6.8). This explains why long-time simulations are required here with millions of time steps. So, it is computationally expensive to solve the STFE for the spreading cases, even though it is just a simple one-dimensional SPDE, where 50 realisations of each stochastic case in this subsection ($\triangle z = 10^{-2}$ and $\triangle t = 10^{-3}$) needs about 20 core hours. It also means that MD is currently not available here due to the several decades of running time. Figure 6.8 shows faster spreading, which agrees with the stochastic power law, $\tilde{\ell} \sim \tilde{t}^{1/4}$ (see the dashed line) due to the thermal fluctuations. This result was first confirmed numerically in [88] with the STFE. Note that there exists a transfer from Tanner's law to the stochastic law, showing that the noise dominates over the deterministic relaxation at the later stages of the spreading ($t \gg 1$). In addition, though stronger noise (with a larger φ) does not change the power law, it will lead to an earlier transfer (see the deviations between red and blue lines in Figure 6.8).
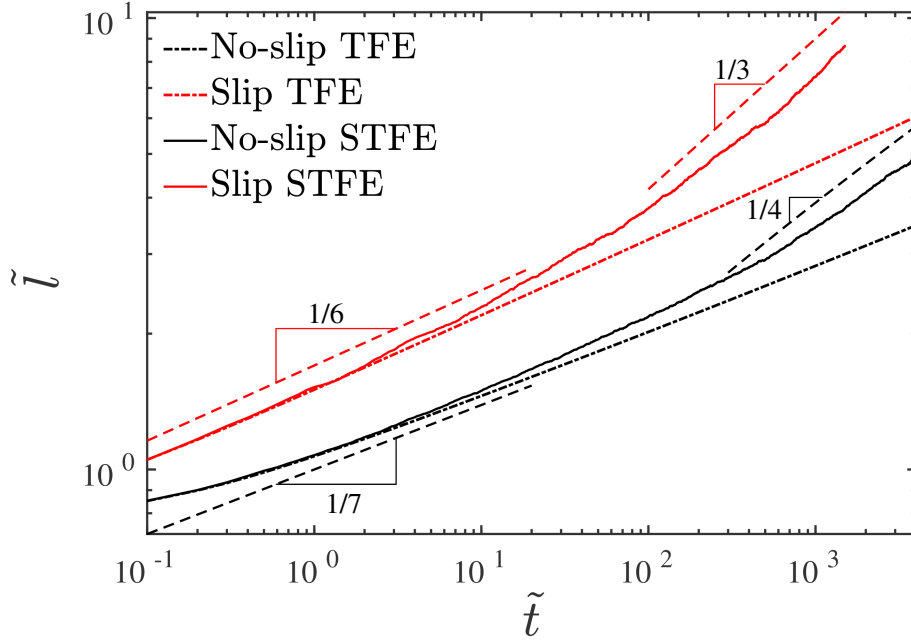
Figure 6.9: Influence of the slip on the characteristic lateral scales. The dash-dotted lines are the solutions of the deterministic cases. The solid lines are the solutions of the stochastic cases with $\varphi = 10^{-3}$. Dashed lines represent similarity solutions in Equation (6.23) and (6.27). Here, $\tilde{\beta} = 1.0$

The characteristic lateral scales with different boundary conditions are plotted in

Figure 6.9, in which the numerical solutions match not only previous similarity solutions (no-slip) [88], but also the new power law with the slip boundary (see Equation (6.27)) very well. Despite faster spreading in the case with the slip boundary (red lines), it has been shown to have a similar transfer from the 'deterministic regime' to the 'stochastic regime' compared with the no-slip case.

6.4 Droplet coalescence

A further interesting application of the lubrication thin-film equation is droplet coalescence on a substrate. However, most of the previous studies on this topic are carried out at the macroscale with the (deterministic) TFE [92, 138, 139]. The STFE has never been employed to model nano-droplet coalescence on a substrate. As Perumanath et al [63] have shown that the thermal fluctuations are crucial to the dynamics of coalescence of two 'free' nano-droplets in a vacuum with MD, a similar influence of noise can be expected in the coalescence of two 'bounded' nano-droplets, which will be explored by both the MD and STFE solver in this section. Note that we focus on 2D cases here.

(a) Symmetric coalescence   (b) Asymmetric coalescence

$t = t_0 - 1.5\,(\text{ns})$ $t = t_0 - 1.1\,(\text{ns})$

$t = t_0 - 1.0\,(\text{ns})$ $t = t_0 - 0.55\,(\text{ns})$

$t = t_0\,(\text{ns})$ $t = t_0\,(\text{ns})$

$t = t_0 + 3.0\,(\text{ns})$ $t = t_0 + 2.2\,(\text{ns})$

$t = t_0 + 4.25\,(\text{ns})$ $t = t_0 + 4.4\,(\text{ns})$

Figure 6.10: MD results for the coalescence. (a) Symmetric coalescence with the same droplet radius, $R = 10\,\text{nm}$ (b) Asymmetric coalescence with different droplet radii, i.e., $R_1 = 15\,\text{nm}$ and $R_2 = 10\,\text{nm}$.

In MD, the mW model is employed to simulate liquid water (for smaller computational costs compared to the TIP4P/2005) on a smooth platinum substrate at $T = 400\,\text{K}$. The platinum substrate is assumed to be rigid with an atomic mass of $3.24 \times 10^{-25}\,\text{kg}$ [140]. The liquid-solid interaction is modelled by the 12-6 LJ potential (introduced in §3.1.2) with $\epsilon_{\text{ls}}/k_{\text{B}} = 444\,\text{K}$ and $\sigma_{\text{ls}} = 0.28\,\text{nm}$ to create a fully wettable substrate (zero contact angle). With the similar approach used in Chapter 4 and 5, the initial configurations of droplets are cut from a liquid bulk, created from equilibrium NVT simulations with a Nos-Hoover thermostat at the specific temperature. The same ensemble and thermostat is used for the main simulations with the time step, 2.5 femtoseconds.

The results of two coalescence cases are presented in Figure 6.10 with two separate droplets on the substrate set as the initial conditions. The initial distance between the two droplets is 50 nm. Because of the fully wettable substrate, both the droplets spread first until their contact lines touch each other. This moment is defined as t_0 i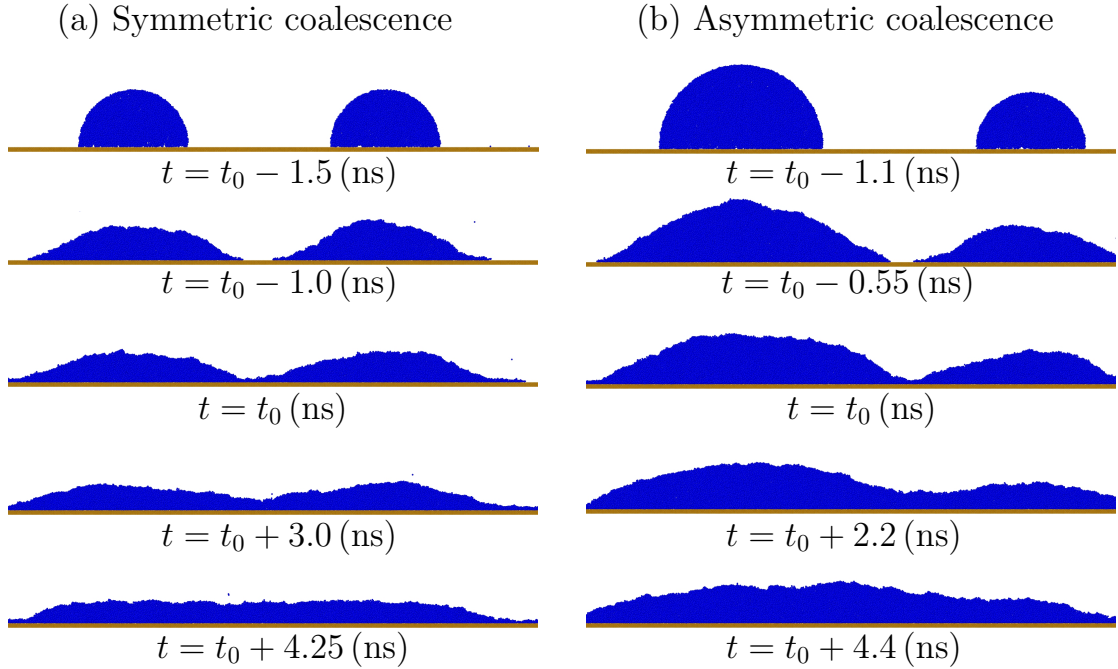n Figure 6.10, when the two droplets are connected by a 'molecular bridge'. After that, the coalescence happens with the growth of the liquid bridge, resulting in one merged droplet. From a theoretical aspect, the minimum interface height, h_{min} at t_0 is expected to be zero. However, because of the thickness of the initial 'molecular bridge', $h_{\text{min}}(t_0)$ is approximately equal to the molecular scale(σ) rather than zero. A similar phenomenon also exists in nano-thread breakup, introduced in Chapter 5, where the minimum thickness of nano-threads is not zero at the breakup time ($h_{\text{min}}(t_{\text{b}}) \neq 0$).

To compare MD results with the predictions of the STFE, the liquid transport properties are calculated with the approaches in §3.1.3. Here, $\mu = 1.64 \times 10^{-4}\,\text{kg}\,\text{m}^{-1}\,\text{s}^{-1}$ and $\gamma = 5.45 \times 10^{-2}\,\text{N}\,\text{m}^{-1}$. The domain width along the z-coordinate, $W = 2\,\text{nm}$. Since the contact angle is zero, the disjoining pressure can be neglected due to the balance between attractive and repulsive van der Waals forces (similar to the condition of the spreading case in Section 6.3). To obtain the initial h for the STFE, the interface profile at t_0 is extracted from each MD realisation with the same approach introduced in Appendix D. Then we shift all the coalescence points to the same position($x = 100\,\text{nm}$) and calculate the averaged interface profiles, $h(t_0)$, which is used as the initial configuration for the STFE.

Our first comparison, Figure 6.11, is for the time evolution of the the minimum bridge height, $h_{\text{min}}(t)$. As we are focussing on the coalescence, t_0 is set as zero. In both cases ((a,c) symmetric coalescence and (b,d) asymmetric coalescence) good agreement is found at all time instants for the mean values of the MD and STFE, whereas the deterministic model (TFE) is not able to capture the physics, highlighting the significant role of thermal fluctuations. Moreover, the stochastic $h_{\text{min}}(t)$ always appears smaller

than that predicted by the (deterministic) TFE at the same time, demonstrating that noise decelerates the coalescence. This finding is contrary to all previous findings in this thesis, that thermal fluctuations accelerate the dynamics (in the instability, thread rupture and spreading). Therefore, we can conclude that the thermal noise does not always works as a driving force in the interface dynamics at the nanoscale, and its role is determined by fluid configurations. In addition, Hernández-Sánchez et al proposed a power law from the TFE to describe the coalescence dynamics and demonstrated their model with experiments in [92]. However, this power law is not found in Figure 6.11(c) and (d), even in the TFE solutions (black dashed lines). At present, the reason is unclear and should be the subject of future investigation.
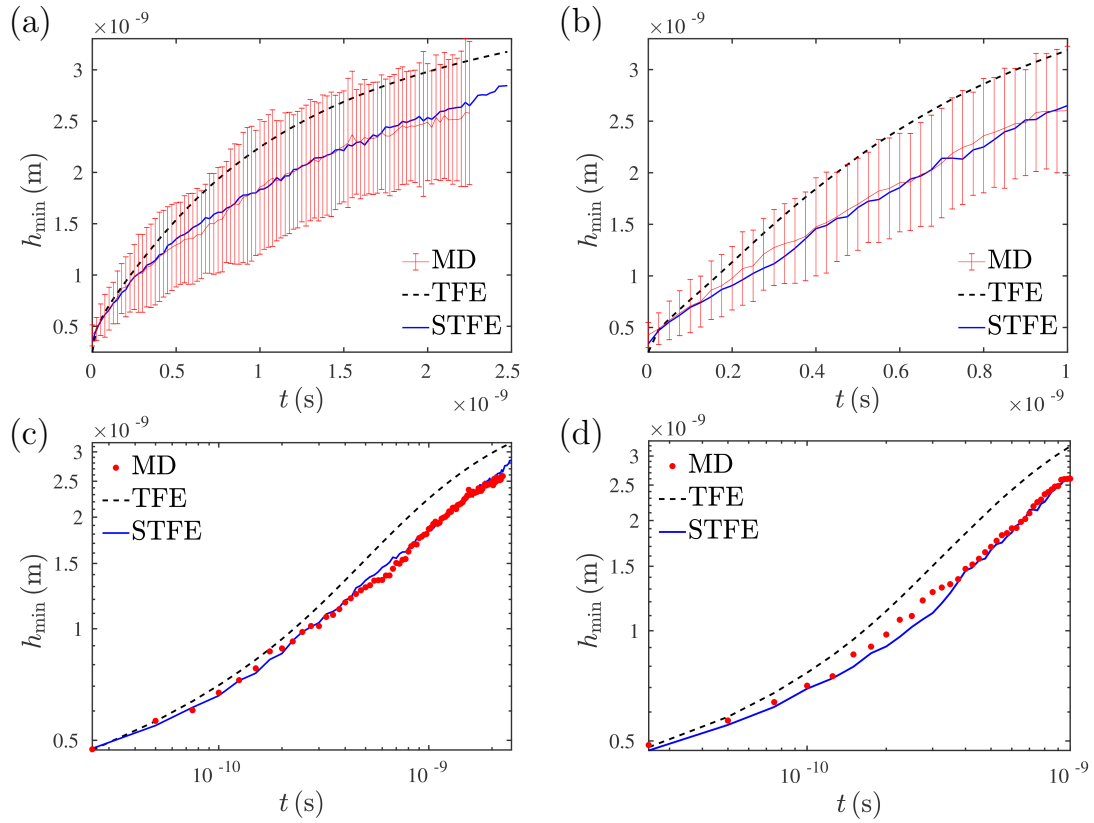
Figure 6.11: Time evolution of the minimum height of the coalescence: comparison between MD and the numerical solutions for the TFE/STFE. for both symmetric coalescence in (a, c) and asymmetric coalescence in (b, d). (a) and (b) are plotted in the uniform-coordinate, while (c) and (d) are illustrated in the log-coordinate. Both the MD and STFE results are the average from 50 realisations. The error bars in (a) and (b) represent the standard deviations of the MD.

94
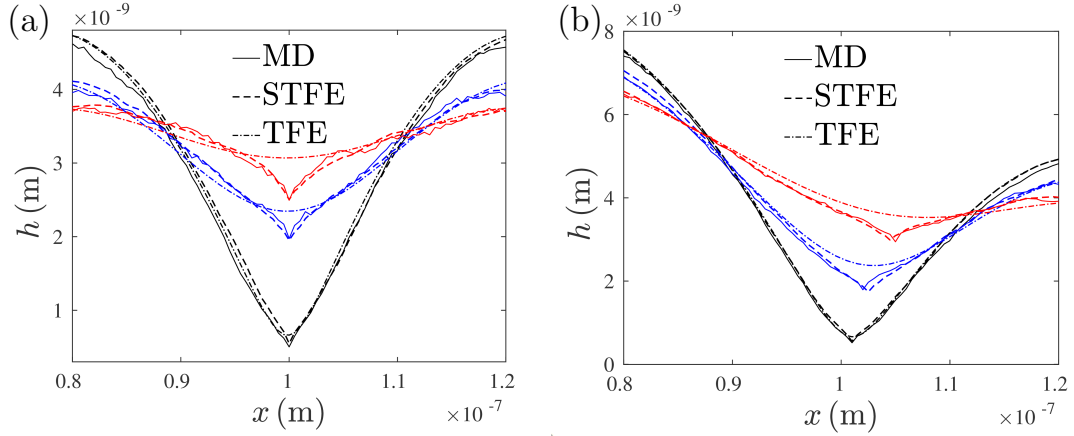
Figure 6.12: Comparisons between the STFE/TFE and the MD at three time instants, t_1 (black lines), t_2 (blue lines) and t_3 (red lines). (a) symmetric coalescence: $t_1 = t_0 + 0.075\,(\mathrm{ns})$, $t_2 = t_0 + 1.13\,(\mathrm{ns})$ and $t_3 = t_0 + 2.0\,(\mathrm{ns})$. (b) Asymmetric coalescence: $t_1 = t_0 + 0.075\,(\mathrm{ns})$, $t_2 = t_0 + 0.575\,(\mathrm{ns})$ and $t_3 = t_0 + 1.25\,(\mathrm{ns})$.

The ensemble-averaged profiles plotted in Figure 6.12 show good overall agreement between the MD results (solid lines) and the STFE solutions (dashed lines) for three time instants in the coalescence. For the asymmetric case, the averaged bottom point ($h_{\min}$) moves to smaller droplet as time goes by, which seems to be driven by gradients of the capillary forces due to the different local curvatures, i.e. the capillary force around the smaller droplet is larger (because of the larger curvature), generating a 'pulling' force towards to the smaller droplet. As noted above, the deterministic predictions (dash-dotted lines) cannot match the MD results. Therefore, we conclude that the nano-droplet coalescence on the fully wettable substrate depends on both surface tension and thermal fluctuations.

6.5   Summary

In this chapter, we developed an efficient numerical solver for the STFE in the Crank-Nicolson framework with a new iteration methods proposed. Based on the validations from analytical models in both deterministic and stochastic cases, the solver has been shown not only to capture the physics at the nanoscale accurately but also to be several orders of magnitude faster than the one with explicit methods (similar to the approach used in Chapter 5).

This solver is then applied to explore two bounded film flows:

(i) nano-droplet spreading in Section 6.3;

95

(ii) nano-droplet coalescence in Section 6.4.

In the spreading case, we have derived similarity solutions with new power laws taking the slip effect into account for both deterministic and stochastic cases in § 6.3.1, validated by the numerical solutions for the TFE/STFE in § 6.3.2. It is found that the slip-modified power laws are larger than previous ones with the no-slip boundary condition, denoting faster spreading. For the coalescence at the nanoscale, both the MD and our solver is employed because no reliable analytical models have been found. The simulations show that thermal fluctuations are non-negligible in the coalescence at the nanoscale, in accordance with the previous findings in other nano-interface dynamics, but decelerate the coalescence, which is opposite to the effect of acceleration found in previous cases. Therefore, it can be concluded that whether thermal fluctuations at the nanoscale are a driving or a dissipative influence depends on the particular fluid configuration.

Chapter 7

Conclusions and future work

In this final chapter, the main achievements and conclusions of the thesis will be summarised (Section 7.1) followed by a discussion on potential future research directions (Section 7.2).

7.1 Conclusion

The influence of thermal fluctuations on nanoscale interfacial flows has been explored both numerically and theoretically. Two main models have been applied: (i) MD used as 'numerical experiments' and (ii) LLNS for analytical solutions and efficient numerical results. The findings from the two models are summarised in this section.

The main results obtained from MD (using LAMMPS[103]) are as follows:

- Different molecular models (including LJ, TIP4P/2005, and mW) were tested and validated in Chapter 3.

- The instability of long cylinders was simulated with liquid argon (LJ) in Chapter 4 and water (mW) in Chapter 5.

- The rupture of nano-threads was explored with water (TIP4P/2005) in Chapter 5.

- Nano-droplet coalescence on a substrate was studied with water (mW) in Chapter 6.

For the SPDE models from the LLNS, the novel achievements are listed here:

- Advanced STFEs were derived in Chapter 3 with the influence of substrate roughness and slip taken into account.

- A theoretical framework, SLE-RP, was proposed in Chapter 4 to predict the RP instability at the nanoscale with thermal fluctuations taken into account.

- An SLE solver was developed with a simple correlated noise model, proposed in Chapter 5. The grid/time-step convergence of the SLE solutions was first shown with the solver. After validation with MD results, the solver was applied to explore the rupture dynamics of cases with a wide range of fluid properties, for which neither experiment nor MD is available.

- An efficient STFE solver was developed in the Crank-Nicolson framework with a new iteration method, proposed in Chapter 6. After validation with the analytical models, the solver was used to study the droplet spreading and coalescence on substrates at the nanoscale.

The above achievements led to the following conclusions on the physics of different nanoscale interfacial dynamics:

- In the RP instability at the nanoscale, thermal fluctuations not only violate the Plateau stable boundary ($\lambda_{\mathrm{crit}} = 2\pi r_0$), but also modify the dominant modes of the perturbations.

- The applicability of the well-known similarity solution [2] has been challenged by our numerical solutions for the SLE, indicating that surface tension still plays a significant role in the rupture dynamics of nano-threads and thus cannot be neglected.

- The nanoscale rupture dynamics (e.g. rupture profiles and transition between different regimes) are complicated, depending on the combined influence of the two dimensionless quantities, Oh and Th.

- Droplet spreading is enhanced by the slip boundary condition in both the 'surface-tension-dominated' regime and 'fluctuation-dominated' regime at the nanoscale.

- Thermal fluctuations decelerate nanoscale droplet coalescence on fully wettable substrates.

7.2 Future directions

Although the work done in this thesis helps to improve understanding of the fluctuating hydrodynamics of nanoscale interfacial flows, it also opens up new avenues of enquiry, which we discuss here.

Correlation Scales

In Chapters 5 and 6, the use of a correlation scale is motivated from two angles. First, the computational SLE/STFE scheme is seen to be unable to converge unless such a scale is introduced, with huge spikes on the free surface observed that appear to prematurely rupture the thread and/or destroy the numerical accuracy. Second, MD suggests that correlation scales exist (in §5.2.3), and as one may expect these are typically on the molecular scale. These issues motivate a number of different questions.

From a modelling viewpoint, the incorporation of molecular correlation scales within a continuum model should be treated with caution, and thus one may interpret a continuum limit as when the correlation length goes to zero. However, in some cases, the correlations seem to have a profound effect on thin-film dynamics simulations and experiments [84], so these issues are far from trivial.

In terms of numerical analysis, there are interesting questions regarding convergence, both as one considers the grid/time-step going to zero and as the correlation scale becomes small. For example, what should we expect if we consider a fixed number of cells within each correlation scale and then take the correlation scale to zero (as one may expect for the continuum limit)? Such questions are related to the development of robust and efficient numerical schemes for SPDE problems. Here, we focus on simplicity, with the linear interpolation of noise. More complex schemes exist, where the noise is represented in terms of appropriate basis functions [78, 85]; however, although these are more mathematically rigorous approaches, we found them to give the same dynamic behaviours at increased computational cost (see Figure 5.6). Clearly, there is scope for more work in this direction, particularly as one considers the possibility of developing 2D schemes, as even though the SLE is much cheaper than MD, it is still more computationally burdensome than deterministic methods (as a minimum, due to the requirement for ensembles).

Similarity Solutions

By considering a liquid with sufficiently small surface tension, we were able to recover the power law predicted by Eggers' similarity solution [2] for the nano-thread rupture in Chapter 5, as previously also identified in experiments with colloid-polymer mixtures [67]. However, no agreement was obtained between the SLE and the similarity solution for the universal profiles predicted in [2] and surface tension was seen to influence the power law even at physical values, as seen in Figures 5.9 and 5.14. Therefore, it remains an open problem to derive similarity solutions for the breakup that can incorporate surface tension, building on the new framework and considering the most probable breakup in a stochastic process.

In addition, Hernández-Sánchez et al proposed a similarity solution to predict the coalescence of two sessile drops [92], where the power law of the similarity solution was confirmed by experiments in [92], but cannot be recovered in the numerical tests in Section 6.4; the reason for this is unknown. Moreover, it is interesting to explore whether a similarity solution exists for the coalescence that takes the influence of the thermal fluctuations into account. Despite the decelerating effect of the noise found numerically, it would be more convincing to compare the power law of different regimes (i.e. the surface tension and thermal fluctuations) directly.

Transition prediction

In Section 5.4, liquid thread rupture is a multiscale phenomenon with complicated transitions between different regimes. Numerical solutions in Figure 5.14 and 5.15 show a transition from the V-regime to F-regimes. However, it remains unclear whether a scaling law exists between the crossover (transition) point and Oh. To answer this question, we need to develop more accurate and efficient schemes (e.g. higher-order schemes and implicit time marching methods) to capture many decades of dynamics, which could be the subject of future work.

In addition, we found a transition from the 'surface-tension-dominated' regime to the 'fluctuation-dominated' regime in the nano-droplet spreading in Section 6.3. It would be interesting to investigate the relationship between the transition point and the fluctuation intensity φ with different boundary conditions.

Experimental analysis

For the nano-thread/cylinder dynamics, one not only has small spatial scales, but also small temporal ones for the problems of interest. This is in contrast to thin-film dynam-

ics, where typical time scales are macroscopic when highly viscous films are considered [58, 80] and therefore experimental analysis that temporally resolves features becomes possible. For the problems considered in Chapters 4 and 5, it seems most likely that experimental verification would come first from the ultra-low surface tension liquids developed in [67, 68], which make Th moderate even at the microscale where one can perform imaging. There are many potential directions for experimental analysis to take, but a starting point would be to more carefully consider the rupture profiles and scaling of $h_{\min}$ to see how these compare to the predictions in Chapter 5.

Other physical factors

Most of the physics modelled in this thesis are ideal, where some factors are assumed negligible, but this is not always the case in the real physical world. There are therefore numerous potential extensions of the present work considering other physical factors. For example, it would be an interesting idea to consider ambient fluids at nanoscale, which have been known to affect the macroscale RP instability [22, 141] and the rupture of nano-threads [70]. Another interesting factor is the substrate (boundary) roughness in thin-film flows, which has been modelled by the new STFE (Equation (3.51)) proposed in §3.2.3. It would not be difficult to supplement this factor into the STFE solver developed in Chapter 6, in order to explore how the substrate roughness affects the linear TCW and nonlinear dynamics such as rupture, spreading and coalescence.

Appendix A

Governing equations

A.1 Axisymmetric NS equations for jet flows

In this section, the axisymmetric NS equations for jet flows are presented, used to derive the SLE in § 3.2.2.

A.1.1 Fluid equations

After eliminating all the terms with respect to ϕ in the cylinder coordinates (z, r, ϕ), the axisymmetric incompressible equation can be written as,

$$\frac{\partial u}{\partial z} + \frac{\partial v}{\partial r} + \frac{v}{r} = 0 \,, \tag{A.1}$$

$$\rho \frac{\partial u}{\partial t} + \rho \left(u \frac{\partial u}{\partial z} + v \frac{\partial u}{\partial r} \right) = -\frac{\partial p}{\partial z} + \frac{\partial \tau_{zz}}{\partial z} + \frac{\partial \tau_{zr}}{\partial r} + \frac{1}{r}\tau_{zr} \,, \tag{A.2}$$

$$\rho \frac{\partial v}{\partial t} + \rho \left(u \frac{\partial v}{\partial z} + v \frac{\partial v}{\partial r} \right) = -\frac{\partial p}{\partial r} + \frac{\partial \tau_{rz}}{\partial z} + \frac{\partial \tau_{rr}}{\partial r} + \frac{1}{r}\tau_{rr} - \frac{2\mu}{r^2}v \,, \tag{A.3}$$

where u and v are the axis and radial velocity respectively. Substituting the constitutive equation of all the τ into the two momentum equation (Equation (A.2) and (A.3)) gives

$$\frac{\partial u}{\partial t} + \left(u \frac{\partial u}{\partial z} + v \frac{\partial u}{\partial r} \right) = -\frac{1}{\rho} \frac{\partial p}{\partial z} + \nu \left(\frac{\partial^2 u}{\partial z^2} + \frac{\partial^2 u}{\partial r^2} + \frac{1}{r} \frac{\partial u}{\partial r} \right) \,, \tag{A.4}$$

$$\frac{\partial v}{\partial t} + \left(u \frac{\partial v}{\partial z} + v \frac{\partial v}{\partial r} \right) = -\frac{1}{\rho} \frac{\partial p}{\partial r} + \nu \left(\frac{\partial^2 v}{\partial z^2} + \frac{\partial^2 v}{\partial r^2} + \frac{1}{r} \frac{\partial v}{\partial r} - \frac{v}{r^2} \right) \,. \tag{A.5}$$

A.1.2 Interface equations

The interface equations are introduced in this subsection with h representing the interface position. As $\nabla h = (\partial_z h, -1)$, the kinematic boundary condition,

$$\frac{\partial h}{\partial t} + u\frac{\partial h}{\partial z} - v = 0 \,. \tag{A.6}$$

Here, with $\boldsymbol{n} = (-\partial_z h, 1)/\sqrt{1 + (\partial_z h)^2}$, the balance of normal force (Equation (3.18)) is written as

$$p + \frac{1}{1 + (\partial_z h)^2}\left[\tau_{rr} - 2\partial_z h\tau_{zr} + (\partial_z h)^2\,\tau_{zz}\right] = \gamma\left(\frac{1}{R_1} + \frac{1}{R_2}\right) \,. \tag{A.7a}$$

Explicitly, this gives:

$$p + \frac{2\mu}{1 + (\partial_z h)^2}\left[\frac{\partial v}{\partial r} + \frac{\partial h}{\partial z}\left(\frac{\partial u}{\partial r} + \frac{\partial v}{\partial z}\right) + \left(\frac{\partial h}{\partial z}\right)^2\frac{\partial u}{\partial z}\right]$$
$$= \gamma\left[\frac{1}{h\sqrt{1 + (\partial_z h)^2}} - \frac{\frac{\partial^2 h}{\partial z^2}}{\left(1 + (\partial_z h)^2\right)^{\frac{3}{2}}}\right] \,. \tag{A.7b}$$

Additionally, $\boldsymbol{t} = (1, \partial_z h)/\sqrt{1 + (\partial_z h)^2}$ yields the expression of the tangential force balance from Equation (3.19),

$$\partial_z h\left(\tau_{rr} - \tau_{zz}\right) + \left[1 - (\partial_z h)^2\right]\tau_{rz} = 0 \,. \tag{A.8a}$$

Explicitly, this gives

$$2\partial_z h\left(\frac{\partial v}{\partial r} - \frac{\partial u}{\partial z}\right) + \left[1 - (\partial_z h)^2\right]\left(\frac{\partial u}{\partial r} + \frac{\partial v}{\partial z}\right) = 0 \,. \tag{A.8b}$$

A.2 Two dimensional LLNS equations for thin-film flows

In this appendix, we present the two-dimensional LLNS, used to derive the STFE in § 3.2.3.

A.2.1 Flow equations

The 2D LLNS is written as below with the terms about z eliminated,

$$\frac{\partial u}{\partial x} + \frac{\partial v}{\partial y} = 0 \,, \tag{A.9}$$

$$\rho \frac{\mathrm{D}u}{\mathrm{D}t} = -\frac{\partial(p + \Pi)}{\partial x} + \frac{\partial(\tau_{xx} + S_{xx})}{\partial x} + \frac{\partial(\tau_{xy} + S_{xy})}{\partial y} \,, \tag{A.10}$$

$$\rho \frac{\mathrm{D}v}{\mathrm{D}t} = -\frac{\partial(p + \Pi)}{\partial y} + \frac{\partial(\tau_{xy} + S_{xy})}{\partial x} + \frac{\partial(\tau_{yy} + S_{yy})}{\partial y} \,. \tag{A.11}$$

A.2.2 Interface Equations

The kinematic boundary condition can be obtained with $\nabla h = (\partial_x h, -1)$:

$$\frac{\partial h}{\partial t} + u \frac{\partial h}{\partial x} - v = 0 \,. \tag{A.12}$$

Since $\boldsymbol{n} = (-\partial_x h, 1)/\sqrt{1 + (\partial_x h)^2}$ and $\boldsymbol{t} = (1, \partial_x h)/\sqrt{1 + (\partial_x h)^2}$, the balance of normal force gives

$$p + \frac{1}{1 + (\partial_x h)^2} \left[(\partial_x h)^2 (\tau_{xx} + S_{xx}) - 2\partial_x h(\tau_{xy} + S_{xy}) + (\tau_{yy} + S_{yy}) \right] = -\gamma \frac{\partial_x^2 h}{[1 + (\partial_x h)^2]^{3/2}} \,. \tag{A.13}$$

The tangential force balance can be expressed as,

$$\partial_x h \left(\tau_{xx} + S_{xx} - \tau_{yy} - S_{yy} \right) + \left[(\partial_x h)^2 - 1 \right] (\tau_{xy} + S_{xy}) = 0 \,. \tag{A.14}$$

Appendix B

Stochastic shear stress on the slip boundary

In §3.1.3, the Green-Kubo function is used to calculate bulk viscosity, written as,

$$\mu = \frac{V_{\text{bulk}}}{k_{\text{B}}T} \int_0^\infty \langle P(t)\,P(0) \rangle\, dt \quad (i \neq j), \tag{B.1}$$

Since P represents the pressure tensors from the Green-Kubo scheme, the covariance of stochastic shear stress, S, is proportional to $k_{\text{B}}T\mu/V_{\text{bulk}}$, namely,

$$\langle S(t)S(0) \rangle \sim \langle P(t)P(0) \rangle \sim \frac{k_{\text{B}}T\mu}{V_{\text{bulk}}}\,, \tag{B.2}$$

This finding is consistent with Equation (3.16) in §3.2.1 because

$$
\begin{aligned}
\left\langle S(\mathbf{r},t)S(\acute{\mathbf{r}},\acute{t}) \right\rangle &= 2\,k_{\text{B}}\,\mu\,T\,\delta(x-\acute{x})\,\delta(y-\acute{y})\,\delta(z-\acute{z})\,\delta(t-\acute{t}) \\
&\sim \frac{2\,k_{\text{B}}\,\mu\,T\,\delta(t-\acute{t})}{dx\,dy\,dz} \\
&\sim \frac{2\,k_{\text{B}}\,\mu\,T\,\delta(t-\acute{t})}{dV_{\text{bulk}}}\,,
\end{aligned} \tag{B.3}
$$

Similarly, the viscosity on the slip boundary can be modelled by the BB model [126], as presented below,

$$\mu = \frac{\beta}{A_{\text{s}}k_{\text{B}}T} \int_0^\infty \langle F(t)\,F(0) \rangle_{\text{eq}}\, dt \quad (i \neq j), \tag{B.4}$$

where F is the friction force on the liquid-solid interface and A_{s} represents the interface area. The subscript 'eq' means that this particular formula is only valid at the equilib-

rium state. Since the stochastic shear stress on the liquid-solid interface, $S_{\mathrm{s}} \sim F/A_{\mathrm{s}}$. Hence,

$$\langle S_{\mathrm{s}}(t)S_{\mathrm{s}}(0)\rangle \sim \frac{k_{\mathrm{B}}T\mu}{\beta A_{\mathrm{s}}}\,. \tag{B.5}$$

Combining Equation (B.5) with

$$\frac{1}{dA_{\mathrm{s}}} = \frac{1}{dx\,dz} \sim \delta(x-\acute{x})\,\delta(z-\acute{z})\,,$$

we can derive the covariance of S_{s} (the reverse process can be seen in Equation (B.3)),

$$\langle S_{\mathrm{s}}(\mathbf{r},t)S_{\mathrm{s}}(\acute{\mathbf{r}},\acute{t})\rangle = 2\,k_{\mathrm{B}}\,\mu\,T\,\delta(x-\acute{x})\,\delta(z-\acute{z})\,\delta(t-\acute{t})/\beta\,. \tag{B.6}$$

Therefore, the covariance in § 3.2.2 is

$$\langle S_{\mathrm{s}}(x,t)S_{\mathrm{s}}(\acute{x},\acute{t})\rangle = \frac{2k_{\mathrm{B}}\mu T}{\beta W}\delta(x-\acute{x})\,\delta(t-\acute{t})\,. \tag{B.7}$$

Appendix C

Derivation for R_fluc

In this appendix, we will show how to deal with the integral, $\overline{\left|\int_0^t N(k, t - \mathcal{T})H(k, \mathcal{T})d\mathcal{T}\right|^2}$, in Equation (4.35), namely, demonstrating Equation (C.1).

$$\overline{\left|\int_0^t N(k, t - \mathcal{T})H(k, \mathcal{T})d\mathcal{T}\right|^2} = L\int_0^t H^2 d\mathcal{T}. \tag{C.1}$$

First, we write the integral in a discrete expression,

$$\overline{\left|\int_0^t N(k, t - \mathcal{T})H(k, \mathcal{T})d\mathcal{T}\right|^2} = \left\{\sum_{\mathcal{T}_i=0}^{\mathcal{T}_i=t} [N(k, t - \mathcal{T}_i)\, H(k, \mathcal{T}_i)\, \triangle\mathcal{T}]\right\}^2. \tag{C.2}$$

Since N represents Gaussian random numbers (with zero mean value), we can have

$$\left\{\sum_{\mathcal{T}_i=0}^{\mathcal{T}_i=t} [N(k, t - \mathcal{T}_i)\, H(k, \mathcal{T}_i)\, \triangle\mathcal{T}]\right\}^2$$

$$= \text{E}^2\left\{\sum_{\mathcal{T}_i=0}^{\mathcal{T}_i=t} [N(k, t - \mathcal{T}_i)\, H(k, \mathcal{T}_i)\, \triangle\mathcal{T}]\right\} + \text{Var}\left\{\sum_{\mathcal{T}_i=0}^{\mathcal{T}_i=t} [N(k, t - \mathcal{T}_i)\, H(k, \mathcal{T}_i)\, \triangle\mathcal{T}]\right\}$$

$$= \text{Var}\left\{\sum_{\mathcal{T}_i=0}^{\mathcal{T}_i=t} [N(k, t - \mathcal{T}_i)\, H(k, \mathcal{T}_i)\, \triangle\mathcal{T}]\right\}, \tag{C.3}$$

where 'E' and 'Var' represents the expectation and variance of N, respectively. Because the variance of a sum of Gaussian random variables is equal to the sum of their individual

variances, Equation (C.3) becomes

$$\text{Var}\left\{\sum_{\mathcal{T}_i=0}^{\mathcal{T}_i=t}[N(k,t-\mathcal{T}_i)\,H(k,\mathcal{T}_i)\,\triangle\mathcal{T}]\right\}$$

$$=\sum_{\mathcal{T}_i=0}^{\mathcal{T}_i=t}\text{Var}\left[N(k,t-\mathcal{T}_i)\,H(k,\mathcal{T}_i)\,\triangle\mathcal{T}\right]$$

$$=\sum_{\mathcal{T}_i=0}^{\mathcal{T}_i=t}\left\{\text{Var}\left[N(k,t-\mathcal{T}_i)\right]\,H(k,\mathcal{T}_i)^2\,\triangle\mathcal{T}^2\right\}\,. \tag{C.4}$$

According to Equation (4.34), the variance of $N(k,t)$ is equal to $\delta(t)L$. Substituting this into Equation (C.4) yields

$$\sum_{\mathcal{T}_i=0}^{\mathcal{T}_i=t}\left\{\text{Var}\left[N(k,t-\mathcal{T}_i)\right]\,H(k,\mathcal{T}_i)^2\,\triangle\mathcal{T}^2\right\}$$

$$=\sum_{\mathcal{T}_i=0}^{\mathcal{T}_i=t}\left[\frac{L}{\triangle\mathcal{T}}\,H(k,\mathcal{T}_i)^2\,\triangle\mathcal{T}^2\right]$$

$$=L\sum_{\mathcal{T}_i=0}^{\mathcal{T}_i=t}H(k,\mathcal{T}_i)^2\,\triangle\mathcal{T}\,. \tag{C.5}$$

Combining Equation (C.2) and Equation (C.5), we get

$$\left\{\sum_{\mathcal{T}_i=0}^{\mathcal{T}_i=t}[N(k,t-\mathcal{T}_i)\,H(k,\mathcal{T}_i)\,\triangle\mathcal{T}]\right\}^2=L\sum_{\mathcal{T}_i=0}^{\mathcal{T}_i=t}H(k,\mathcal{T}_i)^2\,\triangle\mathcal{T}\,, \tag{C.6}$$

which is the discrete format of Equation (C.1).

Appendix D

Interface shape extraction in MD
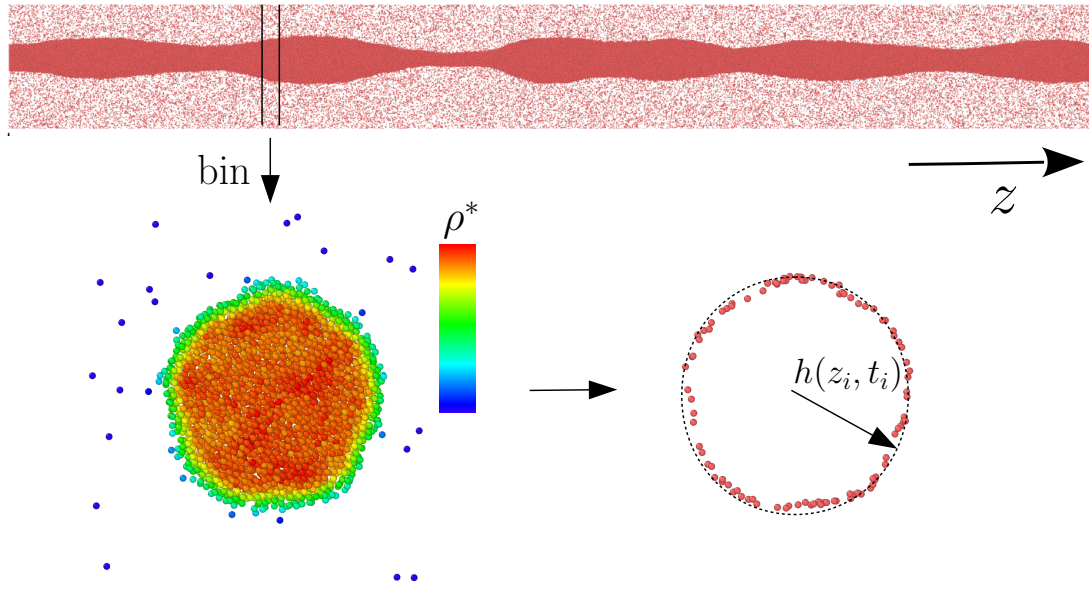
Figure D.1: Molecule density distribution and interface shape of a bin

Based on the axisymmetry assumption, averages of $h(z_i, t_i)$ are taken over molecule positions within a control region (bin). Here the liquid threads are cut into hundreds of bins along the z direction (see the top panel in Figure D.1). Each bin contains 2 to 3 layers of molecules, constructed by a liquid molecule disc in the centre of a bin with some vapour molecules around (see the left panel of Figure D.1). Here, ρ^* represents molecule density (LJ units), which is used to identify the liquid-vapour interface (the right panel of Figure D.1). The average radius (black dash line in Figure D.1) is calculated from the interface obtained above to get the local interface height, $h(z_i, t_i)$ for each bin. With
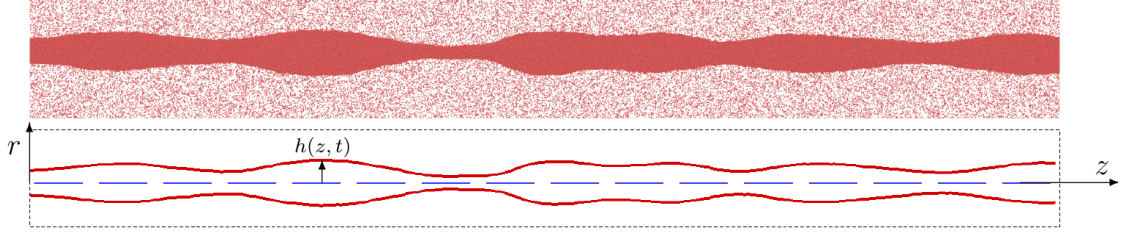
Figure D.2: Interface perturbation extracted from MD

h for all bins, we get the entire interface shape, illustrated in Figure D.2, where a good agreement between original MD data and the profile extracted can be found.
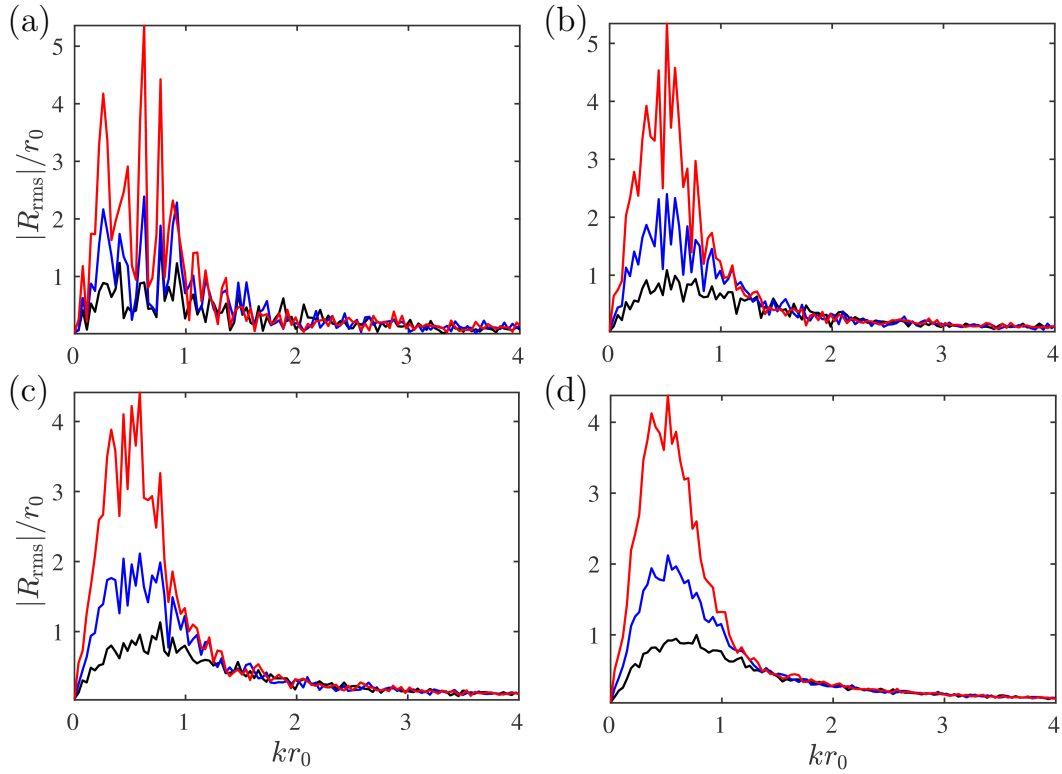
Figure D.3: The r.m.s of dimensionless modal amplitude versus dimensionless wavenumber; ensemble-averaged MD data (*Cylinder 2* in Chapter 4) at various time instants: 0.35 (black), 0.64 (blue), 0.93 (red) /ns; These mean values are from different numbers of realisatons: (a) 1, (b) 5, (c) 10, (d)45.

The discrete Fourier transform (DFT) is then applied for h from one MD realisation to generate a spectrum at various time instants, shown in Figure D.3(a). Since

the spectrum from one realisation looks chaotic, the DFT is repeated for many MD realisations with different initial configurations to pursue a 'smooth' averaged spectrum (see Figure D.3(d)).

Appendix E

Grün's correlated noise model

In this appendix, we introduce the spatially correlated noise model, proposed by Grün in [78], where an exponential correlation function is employed

$$
F_{\mathrm{cor}}(z, L_{\mathrm{c}}) = \begin{cases} Z^{-1}\exp\left[-\frac{1}{2}\left(\frac{L}{L_{\mathrm{c}}}\sin\left(\pi z/L\right)\right)^2\right], & \text{for } L_{\mathrm{c}} > 0\,, \\ \delta(z), & \text{for } L_{\mathrm{c}} = 0\,. \end{cases} \tag{E.1}
$$

Here, L_{c} is the spatial correlation length, L is the domain length, Z is such that $\int_0^L F_{\mathrm{cor}}(z, L_{\mathrm{c}})du = 1$. Note that all the variables in this appendix are non-dimensional, according to the nomenclature in Chapter 5.

The stochastic term, $\mathcal{N}(z, t)$ is expanded as per separation of variables in the Q-Wiener process,

$$
\mathcal{N}(z, t) = \frac{\partial W(z, t)}{\partial t} = \sum_{q\to-\infty}^{q\to+\infty} \chi_q\, \dot{c}_q(t)\, g_q(z)\,. \tag{E.2}
$$

Here, the coefficient $\dot{c}_q$ represents temporal white-noise processes, and the constant χ_q are the eigenvalues of F_{cor},

$$
\chi_q = \int_{-L/2}^{L/2} F_{\mathrm{cor}}(z)e^{-i\,2\pi qz/L}dz \tag{E.3}
$$

where q represents an integer sequence and the wavenumber, $k = 2\pi q/L$. Diez et al.[84] calculated the integral and found that χ_q could be expressed by the Bessel function,

$$
\chi_k = I_k(\alpha)/I_0(\alpha)\,, \tag{E.4}
$$

where

$$\alpha = \left(\frac{L}{2L_\mathrm{c}}\right)^2 .$$

Figure E.1 shows the eigenvalue spectrum for several values of L_c. Note that for $L_\mathrm{c} \to 0$ (i.e., $\alpha \to \infty$), we have $\chi_q \to 1$ for all q, leading to the limiting case of the white (uncorrelated) noise.
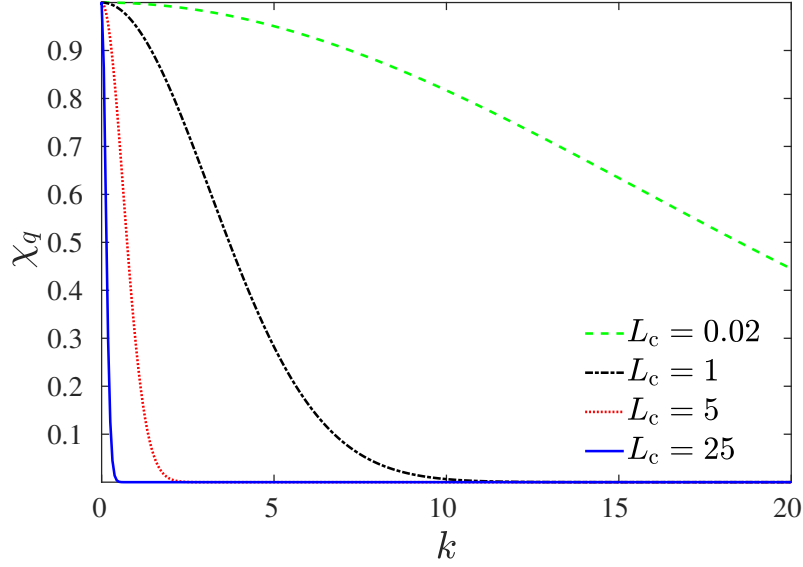
Figure E.1: Linear spectrum of eigenvalues for several values of L_c from Equation (E.4).

The term g_q corresponds to the set of orthonormal eigenfunctions according to

$$g_q(z) = \begin{cases} \sqrt{\frac{2}{L}}\cos(\frac{2\pi q z}{L}), & \text{for } q > 0 \\ \sqrt{\frac{1}{L}}, & \text{for } q = 0 \\ \sqrt{\frac{1}{L}}\sin(\frac{2\pi q z}{L}), & \text{for } q < 0 \end{cases} \tag{E.5}$$

Therefore, the discretized expression of the noise term is

$$N_i^t = \sum_{q=-\frac{M+1}{2}}^{q=\frac{M+1}{2}} \chi_q \, N_q^t \, g_q(z) , \tag{E.6}$$

where M is the nodes number. Samples of N_i^t with $L = 100$ are illustrated in Figure E.2 with different correlation lengths. Note that a larger L_c leads to 'weak' and 'smooth'

noise.
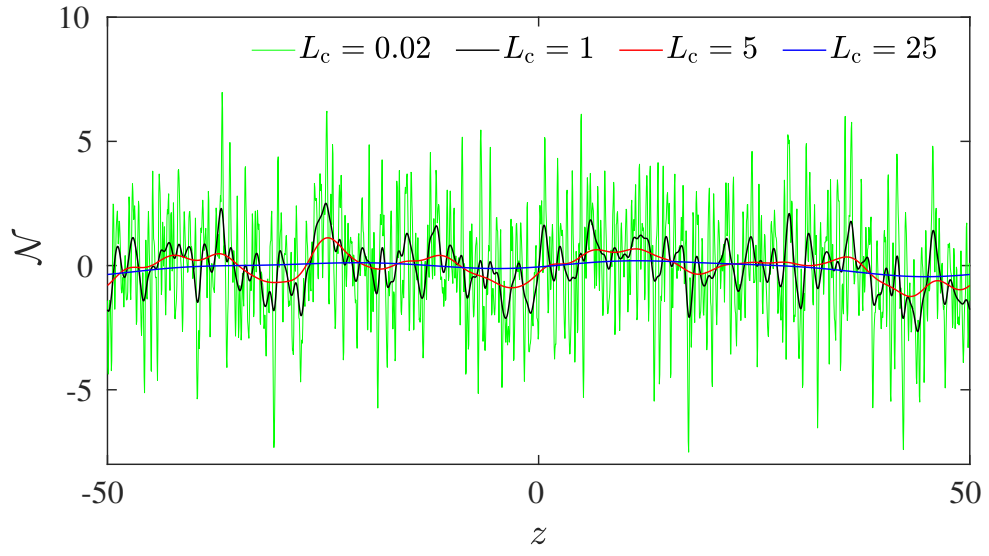
Figure E.2: Spatially correlated noise with different L_c.

Appendix F

Numerics for the STFE

F.1 Diffusion matrix

Based on the positive preserving scheme [134], the surface tension term, T_i $(i = 1, 2...M)$ depends on the five neighbouring grid points,

$$\text{T}_i = \sum_{j=-2}^{2} a_{i,i+j}\, h_{i+j}\,,\tag{F.1}$$

where $a_{i,i+j}$ is the diffusion coefficient. Its expression reads,

$$\begin{bmatrix} a_{i,i-2} \\ a_{i,i-1} \\ a_{i,i} \\ a_{i,i+1} \\ a_{i,i+2} \end{bmatrix} = \left(\frac{\gamma}{6\mu \bigtriangleup x^4} \right) \begin{bmatrix} -h_{i-1}^3 - h_i^3 \\ 3h_{i-1}^3 + 4h_i^3 + h_{i+1}^3 \\ -3h_{i-1}^3 - 6h_i^3 - 3h_{i+1}^3 \\ h_{i-1}^3 + 4h_i^3 + 3h_{i+1}^3 \\ -h_i^3 - h_{i+1}^3 \end{bmatrix}\,.\tag{F.2}$$

Note that, the boundary condition needs to be implemented for the nodes with the number, $i > M - 2$ or $i < 3$. Here, we employ the zero-flux boundary condition (mostly for simplicity), where the first- and third-order derivatives at node 1 and M are 0, i.e.,

$$\partial_x h(0, t) = 0\,, \quad \partial_{xxx}^3 h(0, t) = 0\,,$$
$$\partial_x h(L, t) = 0\,, \quad \partial_{xxx}^3 h(L, t) = 0\,.$$

The schematic of this boundary condition is illustrated in Figure F.1. Here, the black dot represents the grid nodes, while the crosses are the ghost nodes, whose values come

from the corresponding grid nodes.
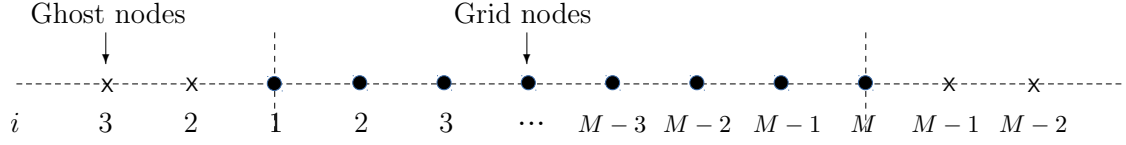
Figure F.1: Schematic of zero-flux boundary condition

Combining Equation (F.2) and the boundary condition above yields the diffusion matrix, $\mathbf{A}$, shown below,

$$
\mathbf{A} = \begin{bmatrix}
a_{11} & 2a_{12} & 2a_{13} & 0 & \cdots & \cdots & \cdots & \cdots & 0 \\
a_{21} & a_{22}+a_{23} & a_{23} & a_{24} & \ddots & \cdots & \cdots & \cdots & \vdots \\
a_{31} & a_{32} & a_{33} & a_{34} & a_{35} & \ddots & \cdots & \cdots & \vdots \\
\vdots & \ddots & \ddots & \ddots & \ddots & \ddots & \ddots & \cdots & \vdots \\
0 & \ddots & a_{i,i-2} & a_{i,i-1} & a_{i,i} & a_{i,i+1} & a_{i,i+2} & \ddots & \vdots \\
\vdots & \ddots & \ddots & \ddots & \ddots & \ddots & \ddots & \ddots & 0 \\
\vdots & \ddots & \ddots & \ddots & a_{M-2,M-4} & a_{M-2,M-3} & a_{M-2,M-2} & a_{M-2,M-1} & a_{M-2,M} \\
\vdots & \ddots & \ddots & \ddots & \ddots & a_{M-1,M-3} & a_{M-1,M-2} & a_{M-1,M-1}+a_{M-1,M-2} & a_{M-1,M} \\
0 & \ddots & \ddots & \ddots & \ddots & \ddots & 2a_{M,M-2} & 2a_{M,M-1} & a_{M,M}
\end{bmatrix} .
$$

Note that $\mathbf{A}$ is the five-diagonal matrix with the zero-flux boundary condition, which is implemented into the coefficients a_{11}, a_{12}, $a_{M,M-1}$ and $a_{M,M}$, including the ghost nodes (see equations below),

$$
a_{11} = -\frac{\gamma}{\mu \bigtriangleup x^4}\left(h_1^3 + h_2^3\right) ,
$$
$$
a_{12} = \frac{2\,\gamma}{3\,\mu \bigtriangleup x^4}\left(h_1^3 + h_2^3\right) ,
$$
$$
a_{M,M-1} = \frac{2\,\gamma}{3\,\mu \bigtriangleup x^4}\left(h_{M-1}^3 + h_M^3\right) ,
$$
$$
a_{MM} = -\frac{\gamma}{\mu \bigtriangleup x^4}\left(h_{M-1}^3 + h_M^3\right) .
$$

116

F.2 Jacobian matrix

Here, the Jacobian matrix, $\mathbf{J} = \frac{\partial \mathbf{T}}{\partial h_i^g}$ used in § 6.1.2 is

$$J_{i,i-2} = \frac{\partial T_i}{\partial h_{i-2}} = a_{i,i-2} \,, \tag{F.3}$$

$$J_{i,i-1} = \frac{\partial T_i}{\partial h_{i-1}} = a_{i,i-1} - \frac{\gamma h_{i-1}^2}{2\mu \triangle x^4} \left(h_{i+1} - 3h_i + 3h_{i-1} - h_{i-2} \right) \,, \tag{F.4}$$

$$J_{i,i} = \frac{\partial T_i}{\partial h_i} = a_{i,i} + \frac{\gamma h_i^2}{2\mu \triangle x^4} \left(h_{i+2} - 4h_{i+1} + 6h_i - 4h_{i-1} + h_{i-2} \right) \,, \tag{F.5}$$

$$J_{i,i+1} = \frac{\partial T_i}{\partial h_{i+1}} = a_{i,i+1} + \frac{\gamma h_{i+1}^2}{2\mu \triangle x^4} \left(h_{i+2} - 3h_{i+1} + 3h_{i-1} - h_{i-1} \right) \,, \tag{F.6}$$

$$J_{i,i+2} = \frac{\partial T_i}{\partial h_{i+2}} = a_{i,i+2} \,. \tag{F.7}$$

Bibliography

[1] M. Moseler and U. Landman. Formation, stability, and breakup of nanojets. *Sci.*, 289:1165–1169, 2000.

[2] J. Eggers. Dynamics of liquid nanojets. *Phys. Rev. Lett.*, 89:084502, 2002.

[3] O. A. Basaran, H. Gao, and P. P. Bhat. Nonstandard inkjets. *Annu. Rev. Fluid Mech.*, 45:85–113, 2013.

[4] S. Shabahang, J. J. Kaufman, D. S. Deng, and A. F. Abouraddy. Observation of the plateau-rayleigh capillary instability in multi-material optical fibers. *Appl. Phys. Lett.*, 99(16):161909, 2011.

[5] S. Mitragotri. Current status and future prospects of needle-free liquid jet injectors. *Nat. Rev. Drug Discovery*, 5(7):543–548, 2006.

[6] A. L. Bertozzi, M. P. Brenner, T. F. Dupont, and L. P. Kadanoff. Singularities and similarities in interface flows. In *Trends and perspectives in applied mathematics*, pages 155–208. Springer, 1994.

[7] Y. D. Shikhmurzaev. *Capillary flows with forming interfaces.* Chapman and Hall/CRC, 2007.

[8] J. J. Kaufman, G. Tao, S. Shabahang, E. Banaei, D. S. Deng, X. Liang, S. G. Johnson, Y. Fink, and A. F. Abouraddy. Structured spheres generated by an in-fibre fluid instability. *Nat.*, 487(7408):463–467, 2012.

[9] R. W. Day, M. N. Mankin, and C. M. Lieber. Plateau–rayleigh crystal growth of nanowire heterostructures: strain-modified surface chemistry and morphological control in one, two, and three dimensions. *Nano Lett.*, 16(4):2830–2836, 2016.

[10] H. A. Stone, A. D. Stroock, and A. Ajdari. Engineering flows in small devices: microfluidics toward a lab-on-a-chip. *Annu. Rev. Fluid Mech.*, 36:381–411, 2004.

[11] J. Stampfl, R. Liska, and A. Ovsianikov. *Multiphoton lithography: Techniques, materials, and applications.* John Wiley & Sons, 2016.

[12] R. W. Day, M. N. Mankin, R. Gao, Y. No, S. Kim, D. C. Bell, H. Park, and C. M. Lieber. Plateau–rayleigh crystal growth of periodic shells on one-dimensional substrates. *Nat. Nanotechnol.*, 10(4):345, 2015.

[13] D. G. Aarts, M. Schmidt, and H. N. Lekkerkerker. Direct visual observation of thermal capillary waves. *Sci.*, 304(5672):847–850, 2004.

[14] J. M. O. De Zarate and J. V. Sengers. *Hydrodynamic fluctuations in fluids and fluid mixtures.* Elsevier, 2006.

[15] L. D. Landau, E. M. Lifshits, and L. P. Pitaevskii. volume 9 of *Course of theoretical physics*, chapter 9, pages 86–91. Pergamon Press, 2 edition, 1980.

[16] J. Eggers and E. Villermaux. Physics of liquid jets. *Rep. Prog. Phys.*, 71:1–79, 2008.

[17] D. F. Rutland and G. J. Jameson. A non-linear effect in the capillary instability of liquid jets. *J. Fluid Mech.*, 46(2):267–271, 1971.

[18] J. A. F. Plateau. *Statique expérimentale et théorique des liquides soumis aux seules forces moléculaires*, volume 2. Gauthier-Villars, 1873.

[19] L. Rayleigh. On the instability of jets. *Proc. London Math. Soc.*, 1:4–13, 1878.

[20] L. Rayleigh. Xvi. on the instability of a cylinder of viscous liquid under capillary force. *London, Edinburgh, Dublin Philos. Mag. J. Sci.*, 34:145–154, 1892.

[21] C. Weber. Zum zerfall eines flüssigkeitsstrahles. *ZAMM-J. Appl. Math. Mech.*, 11:136–154, 1931.

[22] S. Tomotika. On the instability of a cylindrical thread of a viscous liquid surrounded by another viscous fluid. *Proc. R. Soc. London, Ser. A*, 150:322–337, 1935.

[23] J. B. Keller, S. I. Rubinow, and Y. O. Tu. Spatial instability of a jet. *Phys. Fluids*, 16(12):2052–2055, 1973.

[24] E. F. Goedde and M. C. Yuen. Experiments on liquid jet instability. *J. Fluid Mech.*, 40(3):495–511, 1970.

[25] J. Delteil, S. Vincent, A. Erriguible, and P. Subra-Paternault. Numerical investigations in rayleigh breakup of round liquid jets with vof methods. *Comp. Fluids*, 50(1):10–23, 2011.

[26] H. C. Lee. Drop formation in a liquid jet. *IBM J. Res. Dev.*, 18(4):364–369, 1974.

[27] D. B. Bogy. Drop formation in a circular liquid jet. *Annu. Rev. Fluid Mech.*, 11(1):207–228, 1979.

[28] J. Eggers and T. F. Dupont. Drop formation in a one-dimensional approximation of the navier–stokes equation. *J. Fluid Mech.*, 262:205–221, 1994.

[29] M. P. Brenner, J. Eggers, K. Joseph, S. R. Nagel, and X. Shi. Breakdown of scaling in droplet fission at high reynolds number. *Phys. Fluids*, 9(6):1573–1590, 1997.

[30] W. van Hoeve, S. Gekle, J. H. Snoeijer, M. Versluis, M. P. Brenner, and D. Lohse. Breakup of diminutive rayleigh jets. *Phys. Fluids*, 22(12):122003, 2010.

[31] J. B. Keller and M. J. Miksis. Surface tension driven flows. *SIAM J. Appl. Math.*, 43(2):268–277, 1983.

[32] D. T. Papageorgiou. Analytical description of the breakup of liquid jets. *J. Fluid Mech.*, 301:109–132, 1995.

[33] D. T. Papageorgiou. On the breakup of viscous liquid threads. *Phys. fluids*, 7(7):1529–1544, 1995.

[34] J. Eggers. Universal pinching of 3d axisymmetric free-surface flow. *Phys. Rev. Lett.*, 71(21):3458, 1993.

[35] J. R. Castrejón-Pita, A. A. Castrejón-Pita, E. J. Hinch, J. R. Lister, and I. M. Hutchings. Self-similar breakup of near-inviscid liquids. *Phys. Rev. E*, 86(1):015301, 2012.

[36] G. H. McKinley and A. Tripathi. How to extract the newtonian viscosity from capillary breakup measurements in a filament rheometer. *J. Rheology*, 44(3):653–670, 2000.

[37] Y. Li and J. E. Sprittles. Capillary breakup of a liquid bridge: identifying regimes and transitions. *J. Fluid Mech.*, 797:29–59, 2016.

[38] P. K. Notz, A. U. Chen, and O. A. Basaran. Satellite drops: Unexpected dynamics and change of scaling during pinch-off. *Phys. Fluids*, 13(3):549–552, 2001.

[39] A. Rothert, R. Richter, and I. Rehberg. Formation of a drop: viscosity dependence of three flow regimes. *New J. Phys.*, 5(1):59, 2003.

[40] J. R. Castrejón-Pita, A. A. Castrejón-Pita, S. S. Thete, K. Sambath, I. M. Hutchings, J. Hinch, J. R. Lister, and O. A. Basaran. Plethora of transitions during breakup of liquid filaments. *Proc. Natl. Acad. Sci.*, 112(15):4582–4587, 2015.

[41] A. Lagarde, C. Josserand, and S. Protière. Oscillating path between self-similarities in liquid pinch-off. *Proc. Natl. Acad. Sci.*, 115(49):12371–12376, 2018.

[42] S. V. Alekseenko, V. Nakoriakov, B. G. Pokusaev, and T. Fukano. *Wave flow of liquid films*. Begell House New York, 1994.

[43] O. Bäumchen, L. Marquant, R. Blossey, A. Münch, B. Wagner, and K. Jacobs. Influence of slip on the rayleigh-plateau rim instability in dewetting viscous films. *Phys. Rev. Lett.*, 113(1):014501, 2014.

[44] M. Schneemilch and A. M. Cazabat. Shock separation in wetting films driven by thermal gradients. *Langmuir*, 16(25):9850–9856, 2000.

[45] G. Reiter. Dewetting of thin polymer films. *Phys. Rev. Lett.*, 68(1):75, 1992.

[46] G. Reiter. Unstable thin polymer films: rupture and dewetting processes. *Langmuir*, 9(5):1344–1351, 1993.

[47] A. Vrij. Possible mechanism for the spontaneous rupture of thin, free liquid films. *Discuss. Faraday Soc.*, 42:23–33, 1966.

[48] A. Sheludko. Thin liquid films. *Adv. Colloid Interface Sci.*, 1(4):391–464, 1967.

[49] E. Ruckenstein and R. K. Jain. Spontaneous rupture of thin liquid films. *J. Chem. Soc., Faraday Trans. 2: Mol. Chem. Phys.*, 70:132–147, 1974.

[50] M. B. Williams and S. H. Davis. Nonlinear theory of film rupture. *J. Colloid Interface Sci.*, 90(1):220–228, 1982.

[51] A. Oron, S. H. Davis, and S. G. Bankoff. Long-scale evolution of thin liquid films. *Rev. Mod. Phys.*, 69(3):931, 1997.

[52] W. W. Zhang and J. R. Lister. Similarity solutions for van der waals rupture of a thin film on a solid substrate. *Phys. Fluids*, 11(9):2454–2462, 1999.

[53] R. V. Craster and O. K. Matar. Dynamics and stability of thin liquid films. *Rev. Mod. Phys.*, 81(3):1131, 2009.

[54] K. Jacobs, S. Herminghaus, and K. R. Mecke. Thin liquid polymer films rupture via defects. *Langmuir*, 14(4):965–969, 1998.

[55] J. Bischof, D. Scherer, S. Herminghaus, and P. Leiderer. Dewetting modes of thin metallic films: nucleation of holes and spinodal dewetting. *Phys. Rev. Lett.*, 77(8):1536, 1996.

[56] R. Seemann, S. Herminghaus, and K. Jacobs. Dewetting patterns and molecular forces: A reconciliation. *Phys. Rev. Lett.*, 86(24):5534, 2001.

[57] R. Mukherjee and A. Sharma. Instability, self-organization and pattern formation in thin soft films. *Soft Matter*, 11(45):8717–8740, 2015.

[58] J. Becker, G. Grün, R. Seemann, H. Mantz, K. Jacobs, K. R. Mecke, and R. Blossey. Complex dewetting scenarios captured by thin-film models. *Nat. Mater.*, 2(1):59, 2003.

[59] K. Kadau, C. Rosenblatt, J. L. Barber, T. C. Germann, Z. Huang, P. Carlès, and B. J. Alder. The importance of fluctuations in fluid mixing. *Proc. Natl. Acad. Sci.*, 104(19):7741–7745, 2007.

[60] H. Perrin, R. Lhermerout, K. Davitt, E. Rolley, and B. Andreotti. Defects at the nanoscale impact contact line motion at all scales. *Phys. Rev. Lett.*, 116(18):184502, 2016.

[61] D. Belardinelli, M. Sbragaglia, M. Gross, and B. Andreotti. Thermal fluctuations of an interface near a contact line. *Phys. Rev. E*, 94(5):052803, 2016.

[62] J. C. Fernández-Toledano, T. D. Blake, and J. De Coninck. Contact-line fluctuations and dynamic wetting. *J. Colloid Interface Sci.*, 540:322–329, 2019.

[63] S. Perumanath, M. K. Borg, M. V. Chubynsky, J. E. Sprittles, and J. M. Reese. Droplet coalescence is initiated by thermal motion. *Phys. Rev. Lett.*, 122(10):104501, 2019.

[64] E. Secchi, A. Niguès, L. Jubin, A. Siria, and L. Bocquet. Scaling behavior for ionic transport and its fluctuations in individual carbon nanotubes. *Phys. Rev. Lett.*, 116(15):154501, 2016.

[65] J. Koplik and J. R. Banavar. Molecular dynamics of interface rupture. *Phys. Fluids*, 5(3):521–536, 1993.

[66] S. Kawano. Molecular dynamics of rupture phenomena in a liquid thread. *Phys. Rev. E*, 58(4):4468, 1998.

[67] Y. Hennequin, D. Aarts, J. H. van der Wiel, G. Wegdam, J. Eggers, H. N. W. Lekkerkerker, and D. Bonn. Drop formation by thermal fluctuations at an ultralow surface tension. *Phys. Rev. Lett.*, 97:244502, 2006.

[68] J. Petit, D. Rivière, H. Kellay, and J. Delville. Break-up dynamics of fluctuating liquid threads. *Proc. Natl. Acad. Sci.*, 109(45):18327–18331, 2012.

[69] Y. S. Choi, S. J. Kim, and M. U. Kim. Molecular dynamics of unstable motions and capillary instability in liquid nanojets. *Phys. Rev. E*, 73:016309, 2006.

[70] W. Kang and U. Landman. Universality crossover of the pinch-off shape profiles of collapsing liquid nanobridges in vacuum and gaseous environments. *Phys. Rev. Lett.*, 98:064504, 2007.

[71] A. Tiwari, H. Reddy, S. Mukhopadhyay, and J. Abraham. Simulations of liquid nanocylinder breakup with dissipative particle dynamics. *Phys. Rev. E*, 78(1):016305, 2008.

[72] J. R. Royer, D. J. Evans, L. Oyarte, Q. Guo, E. Kapit, M. E. Möbius, S. R. Waitukaitis, and H. M. Jaeger. High-speed tracking of rupture and clustering in freely falling granular streams. *Nat.*, 459(7250):1110–1113, 2009.

[73] D. Min and H. Wong. Rayleighs instability of lennard-jones liquid nanothreads simulated by molecular dynamics. *Phys. Fluids*, 18:024103, 2006.

[74] N. Gopan and S. P. Sathian. Rayleigh instability at small length scales. *Phys. Rev. E*, 90(3):033001, 2014.

[75] C. Mo, L. Qin, F. Zhao, and L. Yang. Application of the dissipative particle dynamics method to the instability problem of a liquid thread. *Phys. Rev. E*, 94(6):063113, 2016.

[76] X. Xue, M. Sbragaglia, L. Biferale, and F. Toschi. Effects of thermal fluctuations in the fragmentation of a nanoligament. *Phys. Rev. E*, 98(1):012802, 2018.

[77] C. Mo, L. Qin, and L. Yang. Crossover behavior study of a thinning liquid bridge using the dissipative particle dynamics method. *Comp. Fluids*, 157:232–239, 2017.

[78] G. Grün, K. Mecke, and M. Rauscher. Thin-film flow influenced by thermal noise. *J. Stat. Phys.*, 122(6):1261–1291, 2006.

[79] K. Mecke and M. Rauscher. On thermal fluctuations in thin film flow. *J. Phys.: Condens Matter*, 17(45):S3515, 2005.

[80] R. Fetzer, M. Rauscher, R. Seemann, K. Jacobs, and K. Mecke. Thermal noise influences fluid flow in thin films during spinodal dewetting. *Phys. Rev. Lett.*, 99(11):114503, 2007.

[81] A. M. Willis and J. B. Freund. Thermal capillary waves relaxing on atomically thin liquid films. *Phys. Fluids*, 22(2):022002, 2010.

[82] Y. Zhang, J. E. Sprittles, and D. A. Lockerby. Molecular simulation of thin liquid films: Thermal fluctuations and instability. *Phys. Rev. E*, 100(2):023108, 2019.

[83] S. Nesic, R. Cuerno, E. Moro, and L. Kondic. Fully nonlinear dynamics of stochastic thin-film dewetting. *Phys. Rev. E*, 92(6):061002, 2015.

[84] J. A. Diez, A. G. González, and R. Fernández. Metallic-thin-film instability with spatially correlated thermal noise. *Phys. Rev. E*, 93(1):013120, 2016.

[85] M. A. Durán-Olivencia, R. S. Gvalani, S. Kalliadasis, and G. A. Pavliotis. Instability, rupture and fluctuations in thin liquid films: Theory and computations. *J. Stat. Phys.*, 174(3):579–604, 2019.

[86] A. A. Pahlavan, L. Cueto-Felgueroso, A. E. Hosoi, G. H. McKinley, and R. Juanes. Thin films in partial wetting: Stability, dewetting and coarsening. *J. Fluid Mech.*, 845:642–681, 2018.

[87] M. S. Shah, V. van Steijn, C. R. Kleijn, and M. T. Kreutzer. Thermal fluctuations in capillary thinning of thin liquid films. *J. Fluid Mech.*, 876:1090–1107, 2019.

[88] B. Davidovitch, E. Moro, and H. A. Stone. Spreading of viscous fluid drops on a solid substrate assisted by thermal fluctuations. *Phys. Rev. Lett.*, 95(24):244505, 2005.

[89] L. H. Tanner. The spreading of silicone oil drops on horizontal surfaces. *J. Phys. D: Appl. Phys.*, 12(9):1473, 1979.

[90] S. Nesic, R. Cuerno, E. Moro, and L. Kondic. Dynamics of thin fluid films controlled by thermal fluctuations. *Eur. Phys. J. Special Top.*, 224(2):379–387, 2015.

[91] A. M. Willis and J. B. Freund. Enhanced droplet spreading due to thermal fluctuations. *J. Phys.: Condens Matter*, 21(46):464128, 2009.

[92] J. F. Hernández-Sánchez, L. A. Lubbers, A. Eddi, and J. H. Snoeijer. Symmetric and asymmetric coalescence of drops on a substrate. *Phys. Rev. Lett.*, 109(18):184502, 2012.

[93] J. D. McGraw, T. Salez, O. Bäumchen, E. Raphaël, and K. Dalnoki-Veress. Self-similarity and energy dissipation in stepped polymer films. *Phys. Rev. Lett.*, 109(12):128303, 2012.

[94] T. Salez, J. D. McGraw, O. Bäumchen, K. Dalnoki-Veress, and E. Raphaël. Capillary-driven flow induced by a stepped perturbation atop a viscous film. *Phys. Fluids*, 24(10):102111, 2012.

[95] K. Kargupta and A. Sharma. Creation of ordered patterns by dewetting of thin films on homogeneous and heterogeneous substrates. *J. Colloid Interface Sci.*, 245(1):99–115, 2002.

[96] J. M. Haile. *Molecular dynamics simulation: elementary methods*, volume 1. Wiley New York, 1992.

[97] M. Karplus and J. A. McCammon. Molecular dynamics simulations of biomolecules. *Nat. Struct. Mol. Biol.*, 9(9):646, 2002.

[98] C. L. Rountree, R. K. Kalia, E. Lidorikis, A. Nakano, L. Van Brutzel, and P. Vashishta. Atomistic aspects of crack propagation in brittle materials: Multimillion atom molecular dynamics simulations. *Annu. Rev. Mater. Res.*, 32(1):377–400, 2002.

[99] C. E. Simien, Y. C. Chen, P. Gupta, S. Laha, Y. N. Martinez, P. G. Mickelson, S. B. Nagel, and T. C. Killian. Using absorption imaging to study ion dynamics in an ultracold neutral plasma. *Phys. Rev. Lett.*, 92(14):143001, 2004.

[100] B. J. Alder and T. E. Wainwright. Phase transition for a hard sphere system. *J. Chem. Phys.*, 27(5):1208–1209, 1957.

[101] J. A. Thomas and A. J. McGaughey. Water flow in carbon nanotubes: transition to subcontinuum transport. *Physical Review Letters*, 102(18):184502, 2009.

[102] J. Rafiee, X. Mi, H. Gullapalli, A. V. Thomas, F. Yavari, Y. Shi, P. M. Ajayan, and N. A. Koratkar. Wetting transparency of graphene. *Nat. Mater.*, 11(3):217, 2012.

[103] S. Plimpton. Fast parallel algorithms for short-range molecular dynamics. *J. Comput. Phys.*, 117:1–19, 1995.

[104] W. C. Swope, H. C. Andersen, P. H. Berens, and K. R. Wilson. A computer simulation method for the calculation of equilibrium constants for the formation of physical clusters of molecules: Application to small water clusters. *J. Chem. Phys.*, 76(1):637–649, 1982.

[105] H. J. C. Berendsen, D. van der Spoel, and R. van Drunen. Gromacs: a message-passing parallel molecular dynamics implementation. *Comp. Phys. Commun.*, 91(1-3):43–56, 1995.

[106] J. C. Phillips, R. Braun, W. Wang, J. Gumbart, E. Tajkhorshid, E. Villa, C. Chipot, R. D. Skeel, L. Kale, and K. Schulten. Scalable molecular dynamics with namd. *J. Comp. Chem.*, 26(16):1781–1802, 2005.

[107] J. E. Lennard. On the determination of molecular fields. *Proc. R. Soc. London*, 106:441–477, 1924.

[108] G. A. Fernandez, J. Vrabec, and H. Hasse. A molecular simulation study of shear and bulk viscosity and thermal conductivity of simple real fluids. *Fluid Phase Equilib.*, 221:157–163, 2004.

[109] S. Toxvaerd and J. C. Dyre. Communication: Shifted forces in molecular dynamics. *J. Chem. Phys.*, 134(8):081102, 2011.

[110] J. L. Abascal and C. Vega. A general purpose model for the condensed phases of water: Tip4p/2005. *J. Chem. Phys*, 123(23):234505, 2005.

[111] H. J. C. Berendsen, J. R. Grigera, and T. P. Straatsma. The missing term in effective pair potentials. *J. Phys. Chem.*, 91(24):6269–6271, 1987.

[112] W. L. Jorgensen, J. Chandrasekhar, J. D. Madura, R. W. Impey, and M. L. Klein. Comparison of simple potential functions for simulating liquid water. *J. Chem. Phys.*, 79(2):926–935, 1983.

[113] F. H. Stillinger and A. Rahman. Improved simulation of liquid water by molecular dynamics. *J. Chem. Phys.*, 60(4):1545–1557, 1974.

[114] M. W. Mahoney and W. L. Jorgensen. A five-site model for liquid water and the reproduction of the density anomaly by rigid, nonpolarizable potential functions. *J. Chem. Phys.*, 112(20):8910–8922, 2000.

[115] V. Molinero and E. B. Moore. Water modeled as an intermediate element between carbon and silicon. *J. Chem. Phys*, 113(13):4008–4016, 2008.

[116] R. L. Rowley and M. M. Painter. Diffusion and viscosity equations of state for a lennard-jones fluid obtained from molecular dynamics simulations. *Int. J. Thermophys.*, 18(5):1109–1121, 1997.

[117] M. S. Green. Markoff random processes and the statistical mechanics of time-dependent phenomena. ii. irreversible processes in fluids. *J. Chem. Phys*, 22:398–413, 1954.

[118] R. Kubo. Statistical-mechanical theory of irreversible processes. i. general theory and simple applications to magnetic and conduction problems. *J. Phys. Soc. Japan*, 12:570–586, 1957.

[119] J. H. Irving and J. G. Kirkwood. The statistical mechanical theory of transport processes. iv. the equations of hydrodynamics. *J. Chem. Phys.*, 18(6):817–829, 1950.

[120] J. G. Kirkwood and F. P. Buff. The statistical mechanical theory of surface tension. *J. Chem. Phys*, 17:338–343, 1949.

[121] A. Trokhymchuk and J. Alejandre. Computer simulations of liquid/vapor interface in lennard-jones fluids: Some questions and answers. *J. Chem. Phys*, 111:8510–8523, 1999.

[122] A. Donev, E. Vanden-Eijnden, A. Garcia, and J. Bell. On the accuracy of finite-volume schemes for fluctuating hydrodynamics. *Commun. Appl. Math. Comput. Sci.*, 5(2):149–197, 2010.

[123] C. Kim, A. Nonaka, J. B. Bell, A. L. Garcia, and A. Donev. Fluctuating hydrodynamics of reactive liquid mixtures. *J. Chem. Phys.*, 149(8):084113, 2018.

[124] R. Kubo. The fluctuation-dissipation theorem. *Rep. Prog. Phys.*, 29(1):255, 1966.

[125] C. Zhao, J. E. Sprittles, and D. A. Lockerby. Revisiting the rayleigh–plateau instability for the nanoscale. *J. Fluid Mech.*, 861, 2019.

[126] L. Bocquet and J. L. Barrat. Hydrodynamic boundary conditions, correlation functions, and kubo relations for confined fluids. *Phys. Rev. E*, 49(4):3079, 1994.

[127] M. Goldin, J. Yerushalmi, R. Pfeffer, and R. Shinnar. Breakup of a laminar capillary jet of a viscoelastic fluid. *J. Fluid Mech.*, 38:689–711, 1969.

[128] R. T. Cygan and J. D. Kubicki. *Molecular modeling theory: Applications in the geosciences*, volume 42. Walter de Gruyter GmbH & Co KG, 2018.

[129] R. MacCormack. The effect of viscosity in hypervelocity impact cratering. *J. Spacecraft Rockets*, 40:757–763, 2003.

[130] J. B. Bell, A. L. Garcia, and S. A. Williams. Numerical methods for the stochastic landau-lifshitz navier-stokes equations. *Phys. Rev. E*, 76(1):016708, 2007.

[131] D. K. Bhuptani and S. P. Sathian. Effect of axial electric field on the rayleigh instability at small length scales. *Phys. Rev. E*, 95(5):053115, 2017.

[132] W. E. Schiesser. *The numerical method of lines: integration of partial differential equations*. Elsevier, 2012.

[133] J. Crank and P. Nicolson. A practical method for numerical evaluation of solutions of partial differential equations of the heat-conduction type. In *Math. Proc. Cambridge Philos. Soc.*, volume 43, pages 50–67. Cambridge University Press, 1947.

[134] J. A. Diez and L. Kondic. Computing three-dimensional thin film flows including contact lines. *J. Comput. Phys.*, 183(1):274–306, 2002.

[135] B. T. Polyak. Newton-kantorovich method and its global convergence. *J Math. Sci.*, 133(4):1513–1523, 2006.

[136] S. Nesic. Stochastic dynamics of substrate-confined systems: Fisher fronts and thin liquid films (doctoral dissertation). 2015.

[137] J. N. Israelachvili. *Intermolecular and surface forces*. Academic press, 2015.

[138] W. D. Ristenpart, P. M. McCalla, R. V. Roy, and H. A. Stone. Coalescence of spreading droplets on a wettable substrate. *Phys. Rev. Lett.*, 97(6):064501, 2006.

[139] S. Karpitschka and H. Riegler. Sharp transition between coalescence and non-coalescence of sessile drops. *J. Fluid Mech.*, 743, 2014.

[140] B. Shi and V. K. Dhir. Molecular dynamics simulation of the contact angle of liquids on solid surfaces. *J. Chem. Phys.*, 130(3):034705, 2009.

[141] S. Mowlavi, I. Shukla, P. T. Brun, and F. Gallaire. Particle size selection in capillary instability of locally heated coaxial fiber. *Phys. Rev. Fluids*, 4(6):064003, 2019.